Characterisation of Hybrid Photon Detectors for the LHCb and an analysis of the rare decay $B_s^o \to \phi\phi$

Judith McCarron

Thesis submitted for the degree of Doctor of Philosophy

School of Physics

The University of Edinburgh

2008

Abstract

The LHCb experiment at CERN is nearing completion and is expected to begin operation in 2008. It will make precision measurements of Charge-Parity in the B meson system. Two Ring Imaging Cherenkov detectors provide excellent charged particle recognition, particularly in their separation of kaons and pions. This thesis outlines the production and testing of Hybrid Photon Detectors, used to measure Cherenkov light in the Ring Imaging Cherenkov detectors. We also report an analysis of the rare decay $B_s^o \to \phi(K^+K^-)\phi(K^+K^-)$ using data produced in a Monte Carlo simulation. The ability to distinguish kaons and pions is vital to reduce the combinatorial background. In this decay a $b \to s$ transition occurs which is heavily suppressed in the Standard Model, and thus provides an excellent opportunity to search for New Physics. We find an expected yield of 1834±1136 $B_s^o \to \phi\phi$ events in a 2fb^{-1} data sample. A background to signal ratio of 0.25±0.18 was obtained.

Declaration

This work represents the effort of many members of the LHCb collaboration at CERN, in Switzerland. I have been part of a team of people who have been worked on the Hybrid Photon Detector project for the LHCb Ring Imaging Cherenkov detectors. The writing of this thesis is entirely my own work.

Acknowledgements

Firstly I would like to thank my mum and my grandfather. Thank you both for all the support over the past four years, I really don't think I could have finished this otherwise. Also Chris for making my time in Edinburgh extremely happy and for keeping me more or less sane, especially during the last six months!

Particular thanks to my supervisor Franz, not only for guiding my through the academic side of things but for always being happy to answer my stupider questions. Thanks also to Stephan, my second supervisor, for the excellent introduction to HPDs and all the guidance in the lab. Thanks to Yuehong for all the advice on my analysis - it was much-needed at times. Also thanks to all the of the PPE group in Manchester for sparking my enthusiasm for particle physics in the first place.

I would also like to thank my friends, who had to put up with a lot at times! Catherine, for all of the de-stressing at the Ashburn, and the long relaxing lunches. Charlotte and Berni, who were with me for my first degree and who I haven't seen for far too long. Thanks to everyone in the Edinburgh office, particularly for making me feel so welcome when I first started. Thanks to James, Alasdair, Reinhardt - mainly for showing me how to play pool. Also thanks to James for more practical help, and teaching me that computers are my friend (most of the time). Thanks and best of luck to all the younger students, particularly Alan, Andrew, Nick and Rob. Finally, I would like to thank the staff and all the other UK students at CERN who made my time in Geneva so enjoyable.

Contents

List of Figures

List of Tables

Chapter 1

Motivation and Theory

1.1 Introduction

It is difficult to say exactly when the field of particle physics began, as people have been speculating on the origin of matter since Greek times. A major milestone was Thompson's discovery of the electron in 1897, when studying electrical discharge in gases. This was the first of the elementary particles to be discovered. Fourteen years later, in 1911, Rutherford showed that even ordinary matter is formed from smaller particles with the discovery of the atom. This came about when particle scattering off a gold foil showed that a small dense structure was responsible for most of the mass in matter. Although the proton had been known about since 1918, it was 1930s before the other constituent of the atom, the neutron, was discovered. In the years following, experiments using cloud and bubble chambers observed many more particles.

By the 1960s matter was being described in terms of four fundamental forces. In an attempt to unite these forces and give structure to the emerging "zoo" of particles the Standard Model of particle physics was developed. This was extremely successful not only in providing a united picture of particles and forces but also in its predictive abilities. Not only the existence but the properties of new particles such as the W and Z bosons and the top and charm quark were predicted. The only predicted particle which remains unobserved at the present time is the Higgs boson, responsible for giving other particles their mass.

Many of the milestone discoveries in particle physics were achieved at the CERN, the particle physics laboratory established near Geneva in 1954. At the present time the Large Hadron Collider (LHC) is currently under construction at CERN and will begin operation in 2008. Operating at a 14 TeV centre-of-mass energy the LHC will be the most powerful accelerator in the world, and will usher in a new era of particle physics.

This thesis outlines the testing of Hybrid Photon Detectors for the LHCb experiment at CERN, and the analysis of the rare particle decay $B_s^o \rightarrow \phi\phi$. Chapter 1 gives a brief introduction to the Standard Model, and prospects for New Physics beyond it. Chapter 2 provides background on the LHCb experiment at CERN. Chapter 3 describes the operation and testing of Hybrid Photon Detectors, an integral part of the RICH counters at the LHCb. The RICH detectors will enable charged particle identification, reducing $b - \overline{b}$-inclusive backgrounds to the point where rare decays are measurable. In Chapter 4 an analysis of the rare decay $B_s^o \rightarrow \phi\phi$ using Monte Carlo data is discussed. This decay enables the measurement of the weak mixing phase ϕ_s and is an excellent channel in which to search for New Physics beyond the Standard Model. Chapter 5 is a summary of the results obtained.

1.2 The Standard Model

The Standard Model of particle physics consists of twelve types of fundamental particle and four force carriers. All of these can be categorised as fermions, which have half-integer spin, or bosons, which have integer spin in units of $\hbar$. The Standard Model fermions are further separated into leptons and quarks. These have a size of $<10^{-17}$ m and are believed to be point-like particles with no internal structure.

Leptons are fundamental fermions occurring in three flavours: electron (e), muon (μ) and tau (τ). The leptons interact via the weak force, and charged leptons also experience electromagnetic forces.

$$\begin{pmatrix} e \\ \nu_e \end{pmatrix} \begin{pmatrix} \mu \\ \nu_\mu \end{pmatrix} \begin{pmatrix} \tau \\ \nu_\tau \end{pmatrix}$$

The leptons form weak doublets, shown above, which are arranged in three generations of increasing mass. The leptons e^-, μ^- and τ^- have charge of $-e$, while the neutrinos ν_e, ν_μ and ν_τ are uncharged. "Normal" matter consists of particles from the first (lightest) generation, while the other, heavier generations decay into first generation particles. Current experimental values for their masses and lifetimes are shown below in Table 1.1:

Lepton	Mass (MeV/c^2)	Mean Lifetime
e	0.5101	$>4.6 \times 10^{26}$ years
μ	105.7	2.197×10^{-6} s
τ	1777.00	290.6×10^{-15} s
$\nu_{e,\mu,\tau}$	<2eV	-

Table 1.1: The properties of the Leptons [1].

Each of the three generations (e, μ and τ) displays separate lepton number conservation. Although the neutrinos are massless in the Standard Model, experimental results suggest that neutrino generations oscillate into each other, requiring that they have mass [2]. Quarks are shown in Table 1.2, and have fractional charge and occur in different "colours" (red, blue and green), or the corresponding "anticolour" (antired, antiblue, antigreen). This property was originally suggested to prevent bound states of quarks from violating

the Pauli Exclusion Principle. For example, the $\triangle^{++}$ baryon has a charge and spin consistent with the quark content "uuu". However, Fermi statistics forbid three identical spin-$\frac{1}{2}$ particles in the same ground state. If each quark carries a different colour charge, then this problem is overcome. The requirement that bound quark states occur only in "colour neutral" combinations such as "rgb" also explains the observed combinations of the quarks [3].

$$\begin{pmatrix} u \\ d \end{pmatrix} \begin{pmatrix} c \\ s \end{pmatrix} \begin{pmatrix} t \\ b \end{pmatrix}$$

Quarks are confined to colour-neutral states called hadrons, which may be fermionic three-quark combinations (qqq or $\overline{qqq}$) or bosonic quark-anti-quark pairs ($q\overline{q}$). The colour charge of the quarks enables them to strongly interact via the exchange of gluons (see Table 1.3). Quarks therefore experience the strong force. Due to this, the composite hadrons they form are also strongly interacting. "Normal" matter consists of protons and neutrons, formed from the first-generation quarks.

Quark	Mass	Charge (e)
u	1.5 - 3 MeV/c^2	$\frac{2}{3}$
d	3-7 MeV/c^2	-$\frac{1}{3}$
s	95±25 MeV/c^2	-$\frac{1}{3}$
c	1.25±0.09 GeV/c^2	$\frac{2}{3}$
t	174.2±3.3 GeV/c^2	$\frac{2}{3}$
b	4.2±0.07 GeV/c^2	-$\frac{1}{3}$

Table 1.2: The properties of the Quarks [4].

The Standard Model also contains bosonic force carriers, the gauge bosons, shown in Table 1.3. Each of these bosons corresponds to one of the fundamental interactions.

$$\gamma \quad W^{\pm} \quad Z^0 \quad g$$

The photon (γ) carries electromagnetic force. It is believed to be massless and an upper limit of 10^{-13} GeV/c^2 has been placed on its mass experimentally [4]. A massless photon

means that the electromagnetic interaction is unlimited in range. The massive $W^{\pm}$ and Z bosons interact over a range given by $\hbar c/M_{W^{\pm}/Z}$ $O(10^{-18}\text{m})$ where M is the boson mass. The $W^{\pm}$ and Z bosons carry the weak force, responsible for nuclear decay. The charged $W^{\pm}$ changes the flavour of quarks participating in an interaction, allowing the quarks to "mix" from one flavour to another [5]. The strong force is carried by the gluon (g), which is confined within hadrons due to its colour charge [6].

Boson	Mass (GeV/c^2)	Charge (e)
γ	$< 10^{-13}$	0
$W^{\pm}$	80.425 $\pm$ 0.038	$\pm$1
Z	91.1876 $\pm$ 0.0021	0
g	-	0

Table 1.3: The properties of the Gauge Bosons [1].

Although the Standard Model has had many successful predictions it is still believed to be incomplete. It does not include a description of gravity, and contains 18 free parameters such as particles masses which cannot be calculated [7]. In particular, the Standard Model in its simplest form assumes neutrinos are massless, a fact disproved when neutrino oscillations were observed in 1998 at the Sudbury Neutrino Observatory [2] [8]. Extensions to the Standard Model have been suggested which include the addition of neutrino masses, but there are still unanswered questions which have lead to the formulation of many new theories (see "Beyond the Standard Model", later).

1.3 The Cabbibo-Kobayashi-Maskawa matrix

The Standard Model contains three sources of charge-parity (CP) violation:

- CP violation occurs in mixing of the quark generations. This is discussed here.
- It is also thought possible for CP violation to occur via strong interactions in flavour conserving processes. However upper bounds on this effect have been established experimentally, suggesting it is very small or zero.

- If non-zero neutrino masses are included, CP violation is possible in neutrino mixing.

(CP violation is discussed further in Section 1.4). In 1963 Cabibbo suggested that quark mass eigenstates are not eigenstates of the weak force, and that "mixing" occurs between flavours [9]. This was done following earlier suggestions by Gell-Mann and Levy. It took the form of a mixing angle θ_C, describing the two families of particles known at the time. Although it solved the problem of strongly-suppressed K-decays as well as the difference in strength of the nuclear β decays and μ decays, it predicted Flavour Changing Neutral Current (FCNC) process which were not in agreement with experimentally measured values [10]. Strangeness-changing neutral currents (e.g. $K_L^o \rightarrow \mu^+\mu^-$) were heavily suppressed relative to the values expected.

This was not adequately explained until 1970, when Glashow, Iliopoulos and Maiani suggested the "GIM" mechanism which involved a new form for the weak current. It postulated a new (charm) quark [11] which was subsequently discovered in 1974 [12] [13]. Loops containing the c quark cancelled contributions from the u quark, explaining the observed rate of $K_L \rightarrow \mu^+\mu^-$ decays [14]. This was followed by the discovery of the bottom quark in 1977 [15] and the top quark in 1995 [16], [17] completing the three generations.

In 1973 Kobayashi and Maskawa showed that flavour mixing could be described by a 3×3 matrix. This matrix has enough degrees of freedom to explain CP violation as well as the flavour mixing [18]. The Cabibbo matrix was extended to the CKM (Cabbibo-Kobayashi-Maskawa) matrix which describes mixing between the mass (strong force) eigenstates q and the weak force eigenstates q$'$ of the quarks:

$$\begin{pmatrix} d' \\ s' \\ b' \end{pmatrix} = \begin{pmatrix} V_{ud} & V_{us} & V_{ub} \\ V_{cd} & V_{cs} & V_{cb} \\ V_{td} & V_{ts} & V_{tb} \end{pmatrix} \cdot \begin{pmatrix} d \\ s \\ b \end{pmatrix} \tag{1.1}$$

A complex 3×3 matrix will have 18 free parameters, but because the matrix is unitary (i.e. $VV^\dagger = I$) and overall common phases are unobservable, the number of free parameters is reduced to four. These are the three real mixing (rotation) angles, and one phase which

parametrises CP violation [7].

Wolfenstein proposed a parametrisation of the CKM matrix based on a power series expansion of each matrix element in terms of $\lambda \simeq sin\theta_C \simeq |V_{us}|$ [19]:

$$V = \begin{pmatrix} 1-\frac{\lambda^2}{2} & \lambda & A\lambda^3(\rho - i\eta) \\ -\lambda & 1-\frac{\lambda^2}{2} & A\lambda^2 \\ A\lambda^3(1-\rho-i\eta) & -A\lambda^2 & 1 \end{pmatrix} \tag{1.2}$$

$$+ \begin{pmatrix} 0 & 0 & 0 \\ -iA^2\lambda^5\eta & 0 & 0 \\ -iA\lambda^3(\rho+i\eta)/2 & A\lambda^4(\frac{1}{2}-\rho-i\eta) & 0 \end{pmatrix} \tag{1.3}$$

This parametrisation is useful as it clearly shows the hierarchical pattern of the matrix elements, with the diagonal elements close to unity and off-diagonal elements becoming progressively smaller [20]. The Wolfenstein parameters are:

$$\lambda = |V_{us}|/\sqrt{|V_{ud}|^2 + |V_{us}|^2} \tag{1.4}$$

$$A = |V_{cb}/V_{us}|/\lambda \tag{1.5}$$

$$\rho + i\eta = V_{ub}^*/(A\lambda^3) \tag{1.6}$$

Here, the η represents the CP-violating phase. This parametrisation is only an approximation of (1.1) and is valid up to λ^5.

The CKM matrix can be also be displayed by a series of unitarity triangles. The unitarity condition applied to different rows or columns of the CKM matrix can be described as a geometrical expression in the complex plane. Because it requires the sum of three phases to equal zero, it represents a closed triangle. Six unitarity triangles can be formed from these relations, all of which have the same area. If arbitrary phases are fixed so that the minimum number of phases is achieved, one non-zero phase remains, which is the source of CP violation [5].

The angles of the Unitarity Triangle, α, β and γ, are all accessible via B decays. Current results for the angles are as shown in figure 1.2 below. The areas which overlap show the allowed regions for the corners. It can be seen that the most severe constraints are on the

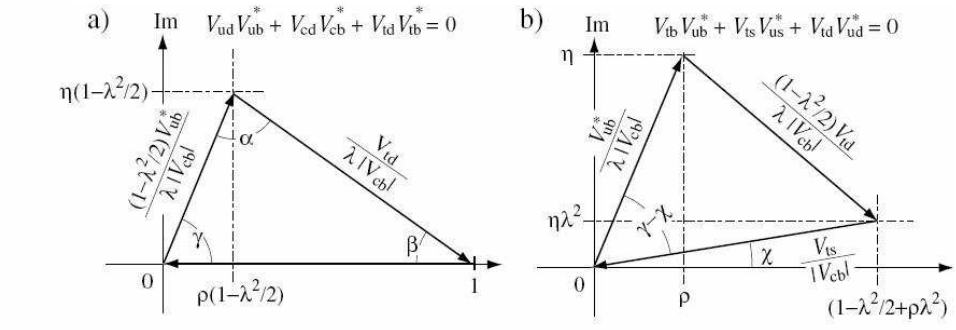

Figure 1.1: Two Unitarity Triangles

apex of the triangle. It is also possible to measure the edges of the triangle directly by measuring the ratios of the CKM matrix elements (for example $\frac{V_{ub}}{V_{cb}}$) and the B_s^o mixing rate [21].

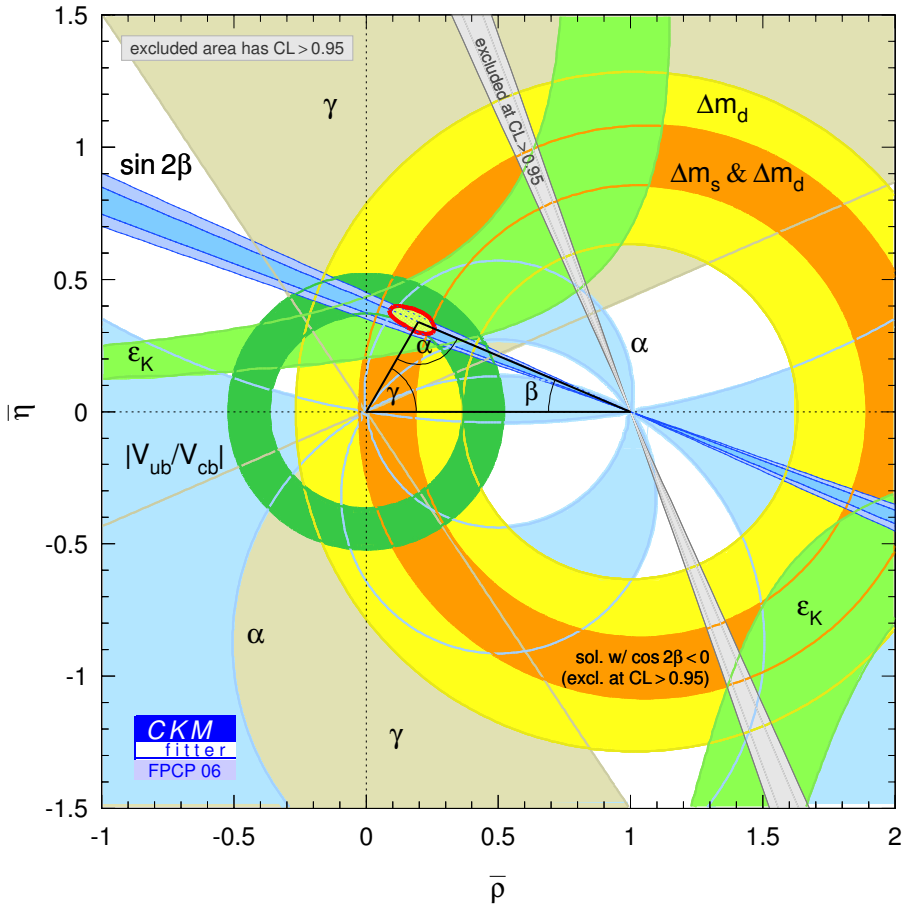

Figure 1.2: Current results from the CKM Fitter group, showing experimental bounds on the Unitarity Triangle [22].

1.4 Charge, Parity and CP Violation

The charge-conjugation operator (C) reverses the sign of all internal quantum numbers such as charge and magnetic moment. This is equivalent to exchanging a particle for its antiparticle [23]. Electromagnetic interactions are invariant under C. If a charge q were replaced with -q and the direction of electromagnetic fields inverted, then reactions would have the same form. However in the weak interaction the charge conjugation of a left handed neutrino ν_L gives a left handed antineutrino $\overline{\nu_L}$.

The charged weak interaction couples only to left-handed particles, and right-handed antiparticles. Since left-handed antineutrinos are never observed in nature the weak interaction violates C maximally.

$$C \mid \nu_L > \rightarrow \overline{\nu}_L$$

Similarly, the charge-conjugate of a right-handed anti-neutrino $\overline{\nu}_R$ is a right-handed neutrino, ν_R.

$$C|\overline{\nu}_R > \rightarrow \nu_R$$

Neither ν_R or $\overline{\nu_L}$ are observed in nature, and C-parity is clearly violated. Observations from β decay have found only neutrinos in J_z=-1/2 ("left-handed") and anti-neutrinos in J_z=$-1/2$ ("right-handed") states. Here, J_z is the z-component of angular momentum, J.

The Parity operator (P) inverts spatial coordinates, so that x,y,z $\rightarrow$ -x,-y,-z. This changes the sign of velocity and acceleration vectors, for example, but leaves axial vectors such as angular velocity and spin unchanged.

$$P|\psi(r) > \rightarrow \psi(-r)$$

Strong and electromagnetic interactions conserve parity and charge. When initial theories of the weak interaction were developed, it was assumed that charge and parity were conserved individually in weak interactions too. However, in the 1950s, the "Theta-Tau" puzzle led this to be reconsidered. A cosmic ray track was observed in which a particle, christened the θ, decayed into three pions. Another particle, the τ, appeared to have an

identical lifetime and mass to the θ, and was observed to decay into two pions. This raised the possibility that the θ and τ were actually the same particle, but there was no way of describing their decays which did not involve parity violation. It was known that the pion had odd parity [24], and so the 3-pion decay corresponds to odd parity ($P_{3\pi}$=$-1\times-1\times-1$ = -1) while the 2-pion decay corresponds to even parity ($P_{2\pi}$=-1×-1 = $+1$).

Yang and Lee realised in 1956 that there was no experimental evidence to prove (or disprove) parity conservation in weak decays [25], and suggested that parity might be violated. Parity violation was first observed in 1957, in the β-decay of ^{60}Co, following which Yang and Lee were awarded the Nobel prize.

Parity conservation is also violated in the lepton sector:

$$P|\nu_L > \rightarrow \nu_R$$
$$P|\nu_R > \rightarrow \nu_L$$

The parity operator acting on a left-handed neutrino will give a right-handed neutrino, and vice versa. Even after the discovery of separate C- and P- violation it was still expected that the combined operation CP (charge conjugation followed by parity reversal, or vice versa) was still conserved. Most processes are invariant under CP-conjugation, including all classical electromagnetic process (for example, classically Maxwell's equations are unchanged by parity or charge reversal). Invariance under CP implies that left-handed particles would behave in the same way as their equivalent right-handed antiparticles. In the example of neutrinos, CP acting on a left-handed neutrino will give a right-handed anti-neutrino and vice versa.

$$CP|\nu_L > \rightarrow \overline{\nu}_R$$
$$CP|\overline{\nu}_R > \rightarrow \nu_L$$

Therefore, the neutrino system is CP-invariant despite violating both C and P separately.

CP violation was first observed in the K meson (kaon) system in 1964, in an experiment carried out by Cronin and Fitch et al. at the Brookhaven AGS accelerator [26]. Neutral kaons are found in two distinct types, the short-lived K_S state and the longer lived K_L. The Brookhaven experiment aimed to study the interactions of the K_L in hydrogen. If

CP is conserved, only the K_S state should decay to $\pi^+\pi^-$, as $CP|\pi^+\pi^- >= |\pi^+\pi^- >$. They expected to prove CP conservation by showing that the decay products of K_S^o and K_L^o were distinct. They observed two states K_1 and K_2 where CP transformation gave:

$$CP|K_1 >= CP[\tfrac{1}{\sqrt{2}}(K^o + \overline{K^o})] = K_1$$
$$CP|K_2 >= CP[\tfrac{1}{\sqrt{2}}(K^o - \overline{K^o})] = -K_2$$

In a small number of cases with a branching ratio of about 10^{-3} the K_L^o decayed to the same two-pion final state as the K_S^o, violating CP conservation. This is due to the fact that the K_1 and K_2 states are not weak eigenstates. The short- and long-lived weak eigenstates K_S and K_L are actually given by:

$$K_S = \tfrac{1}{\sqrt{1+|\epsilon|^2}}(|K_1^o > +\epsilon|K_2^o >)$$
$$K_L = \tfrac{1}{\sqrt{1+|\epsilon|^2}}(\epsilon|K_1^o > +|K_2^o >)$$

where ϵ is a complex mixing parameter. For over thirty years the kaon system had the only evidence of CP violation. In the 1980s large CP violation effects were predicted for neutral B mesons [27] [28]. The B-factories PEP-II at SLAC and KEKB at KEK were built in order to investigate this. In 2001 both the BaBar [29] experiment at PEP-II and the Belle [30] experiment at KEK-B published the first observations of CP violation in B-mesons. Currently, the LHCb is finishing construction at CERN and will investigate these effects more closely (see Chapter 2).

1.5 CP Violation in the B Meson System

The CKM matrix predicts large CP-violating effects in B mesons. B mesons are observed in two mass eigenstates, light (L) and heavy (H), which are a linear combination of neutral B mesons (B^o) and neutral B anti-B mesons ($\overline{B}^o$) and can be described by:

$$|B_L> = p|B^o> + q|\overline{B}^o> \tag{1.7}$$

$$|B_H> = p|B^o> - q|\overline{B}^o> \tag{1.8}$$

where the complex parameters p and q are normalised so that:

$$|q|^2 + |p|^2 \ = 1 \tag{1.9}$$

An initially pure state of B^o or $\overline{B}^o$ will evolve with time as:

$$|B^o(t)> = f_+(t)|B^o> + \frac{q}{p} f_-(t)|\overline{B}^o> \tag{1.10}$$

$$|\overline{B}^o(t)> = \frac{p}{q} f_-(t)|B^o> + f_+(t)|\overline{B}^o> \tag{1.11}$$

where the time-dependent fractions $f_+(t)$ and $f_-(t)$ are given by:

$$f_+(t) \ \equiv e^{-it[(m_L+m_H)/2]} \ e^{-(\Gamma/2)t} \ \cos[(\Delta m)/2] \tag{1.12}$$

$$f_-(t) \ \equiv e^{-it[(m_L+m_H)/2]} \ e^{-(\Gamma/2)t} \ \sin[(\Delta m)/2] \tag{1.13}$$

where m_H and m_L are the masses of the B_L and B_H mesons respectively, and Δm is the mass difference between the B_L and B_H mesons. The average the decay width of the B meson, Γ, is defined as:

$$\Gamma \ \equiv (\Gamma_L + \Gamma_H)/2 \tag{1.14}$$

Where Γ_L and Γ_H are the decay widths of the B_L and B_H mesons respectively. Interference occurs due to the mixing between flavours [28], discussed below.

For a system of neutral mesons such as the B^o and $\overline{B}^o$, three types of CP violation occur:

1. CP Violation in Decay (Direct CP Violation): CP is violated if the amplitude for a decay A_f and it's conjugate process $\overline{A}_{\overline{f}}$ have different magnitudes, i.e. if

$$|A_f/\overline{A}_{\overline{f}}| \neq 1$$

   This process is possible for both charged and neutral decays. For charged hadron decays where mixing cannot happen, this is the only source of CP violation.

2. CP Violation in Mixing (Indirect CP Violation): If the mass eigenstates of neutral particles are not equal to CP eigenstates, CP violation can occur in the mixing between them. This is the case if:

$$|q/p| \neq 1$$

3. CP Violation in Interference: If both B^o and $\overline{B}^o$ can decay to the same final state f interference can occur between states where mixing has occurred and those where it has not. For example, for a final state f, interference occurs between the decays below:

$$\begin{array}{c} \mathrm{B} \longrightarrow f \\ \searrow \overline{B} \nearrow \end{array}$$

The second and third types of CP violation in neutral meson such as the B^o are possible due to meson-antimeson oscillations (B^o - $\overline{B}^o$).

Although CP is not a fundamental symmetry of nature, almost all theories assume CPT (charge-parity-time) invariance is [31]. CPT invariance is an extension of CP invariance, where the operator T will reverse the flow of time, reversing momentum and angular momentum vectors. To preserve CPT with CP violation, T must also be violated.

1.6 Higgs Searches and Beyond the Standard Model

Searches for the Higgs boson are planned at the LHC, particularly at the general-purpose ATLAS and CMS experiments. The Higgs mechanism has been suggested to account for the masses of the gauge bosons ($W^{\pm}$ and Z) which the Standard Model in its simplest form does not explain. The Higgs mechanism gives the gauge bosons mass due to the existence of a non-zero vacuum expectation value. The non-observation of the Higgs at the LEP at CERN and other colliders places its lower mass limit at 114.4 GeV/c^2 with 95% confidence [32]. Current theories suggest a Higgs mass of between 114 GeV/c^2 and 135 GeV/c^2 [33] which would be acessible at the LHC.

Many of the new theories that have been advanced to address deficiencies in the Standard Model will be accessible at the high energies of the LHC. Some of the main models are mentioned below.

String theories describe fundamental particles as small vibrating strings (of size $\mathcal{O}(10^{-35}$ m)). Models with extra dimensions have been suggested to explain the hierarchy problem (the large difference in strength between the weak force and gravity ($\sim 10^{32}$)), including flat and curved extra dimensions. Some of these models predict spin-2 massive gravitons, which have not been observed by collider detectors. They could appear in the LHC as a missing energy and missing transverse momentum signal [33].

Many new theories containing sources of CP violation will also be testable by the LHC. This is of particular relevance to the LHCb experiment, which aims to measure CP violation in the B-Meson system (see Chapter 2). Most extensions to the Standard Model predict new sources of CP violation [34], as observed CP asymmetries are not enough to explain the matter-antimatter asymmetry in the universe. Theories containing new sources of CP-violation include those arising from extra dimensions [35] and those from supersymmetric theories [36]. LHCb will also be sensitive to rare b decays induced by $b \to s$ and $b \to c$ transitions. These Flavour Changing Neutral Current (FCNC) decays are forbidden at tree-level in the Standard Model and so are sensitive to New Physics effects. FCNC decays occur in loops, and other particles may enter in loops where the W boson is found in the Standard Model. Many of these FCNC decays should be accessible at the LHC. Given that the CP violation contained in the Standard Model is insufficient to explain the observed baryon asymmetry in the universe, this strongly suggests that new

physics beyond the Standard Model exists and has yet to be observed [37].

Supersymmetric (SUSY) theories should also be testable at the LHC. Some SUSY theories are particularly attractive as they predict heavy stable particles such as neutralinos. These are weakly interacting and therefore candidates for dark matter. Supersymmetry predicts that each of the known particles has a more massive supersymmetric partner, known as a "sparticle" [38] [39]. These superpartners are higher in mass than the normal particles and are bosonic for known fermions and fermionic for the known bosons. It should be possible to study the production and decay of these heavier supersymmetric particles at the high energies of the LHC. SUSY theories predict that gluon-gluon and gluon-quark fusion should produce the gluon superpartners gluinos and quark superpartners squarks. Other SUSY particles may also be produced with lower cross sections. Even if the superpartners are too massive to be produced directly it may be possible to see SUSY effects from sparticle loops in decays such as $b \rightarrow s\gamma$ at the LHC or the Tevatron. Effects may also be visible in the B_S-$\overline{B}_S$ mixing at LHCb.

In conclusion, the LHC is expected to bring many new and exciting discoveries, many of which will involve the LHCb detector.

Chapter 2

The LHCb Detector

2.1 The Large Hadron Collider

The Large Hadron Collider (LHC) accelerator complex has been constructed at CERN, outside Geneva. It is currently under commission and is due to begin running in 2008. The LHC will collide protons onto protons at 14 TeV centre-of-mass energy at a rate of 40 MHz. This will allow precision measurements of Standard Model parameters and may reveal signs of New Physics beyond the Standard Model.

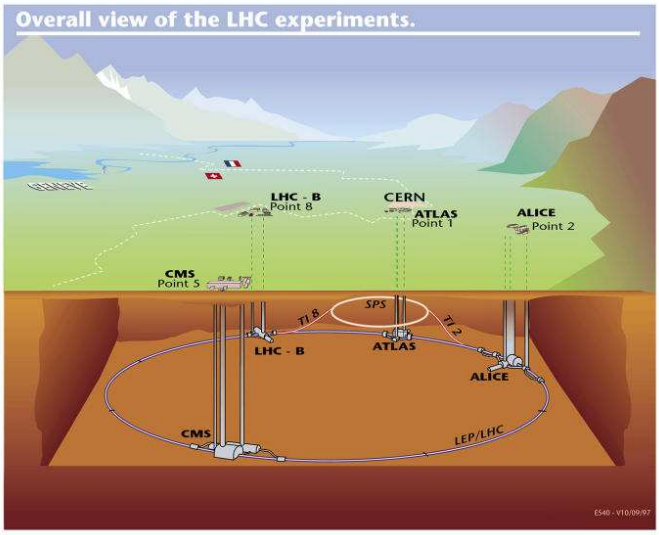

Figure 2.1: The Large Hadron Collider (LHC), showing the four experiments sited around the collider ring.[2]

Four experiments will be situated on the LHC ring. These can be seen in Fig. 2.1. **ATLAS** (**A** **T**orioldal **L**HC Apparatu**S**) and **CMS** (**C**ompact **M**uon **S**olenoid) are both general-purpose detectors. **ALICE** (**A** **L**arge **I**on **C**ollider **E**periment) will study the collision of lead nuclei. **LHCb** (**L**arge **H**adron **C**ollider **b**eauty experiment) will study b-physics and is discussed in more detail below.

2.2 The LHCb Experiment

The LHCb experiment will make precision measurements of Charge-Parity (CP) violation and rare B-meson decays. As well as providing a more detailed understanding of quark flavour physics it may reveal signs of physics beyond the Standard Model. The original LHCb design was reoptimised in 2003 to reduce the material budget and improve the trigger performance [40]. The main components of the detector can be seen in Fig. 2.2, comprising the beampipe, vertex locator (VELO), dipole magnet, tracking stations, two Cherenkov (RICH) detectors and the calorimeter and muon systems.

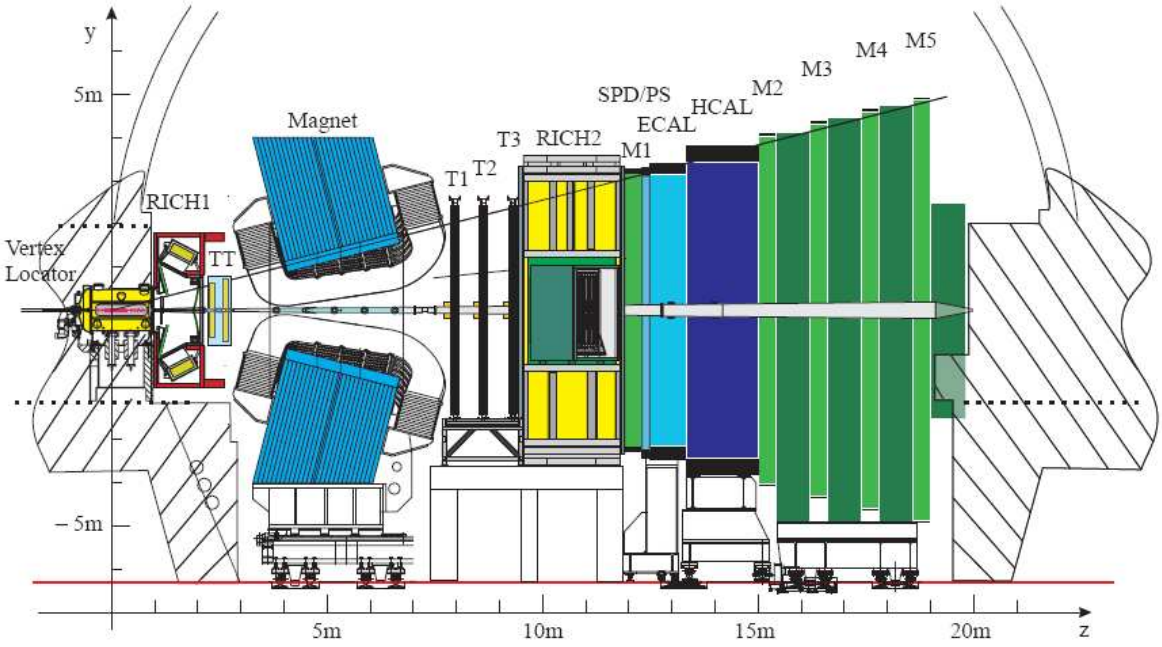

Figure 2.2: The Large Hadron Collider beauty (LHCb) experiment (side view) [40].

The LHCb experiment will measure hadrons containing b and $\overline{b}$ quarks, which are usually produced in correlated pairs at a small angle to the beamline. This enables it to be built as a forward-arm spectrometer covering a polar angle range of 15-300 mrad [41]. It is optimised for an average luminosity of $2{\times}10^{32}$ cm^{-2}s^{-1}, where there will be around 10 MHz of crossings with visible p-p interactions. This luminosity was chosen to maximise the probability of having one proton-proton interaction per event (see Fig. 2.3). This ensures

that the detector occupancy is kept low and simplifies event reconstruction. Due to the relatively high rate and high multiplicity environment of the LHC, excellent charged particle separation, very good proper-time resolution and high track reconstruction efficiency are needed.

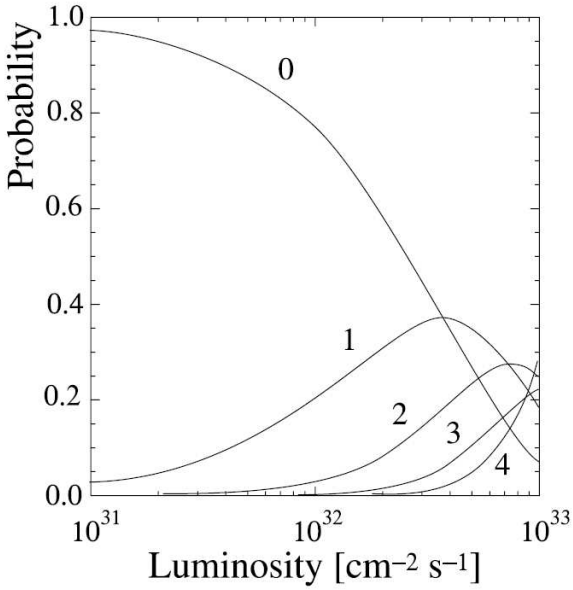

Figure 2.3: The probability of a given number of p-p interactions per bunch crossing as a function of luminosity [42].

Particle detection in the LHCb experiment occurs in two main stages, charged and neutral particle track reconstruction and particle identification. Information is passed to the trigger system which serves to extract the small fraction of events containing interesting B decays.

2.3 Particle Tracking

The tracking system finds charged particle tracks and measures the momenta of the particles. This is possible because a dipole magnet produces a magnetic field which affects the trajectories of charged particles, causing their tracks to become curved. The tracking system consists of the VELO vertex detector, situated close to the interaction point, and four tracking stations: one (the trigger tracker) before the magnet, and three (T1-T3) after it. Charged tracks are reconstructed with an efficiency of ∼95%.

2.3.1 The Vertex Locator

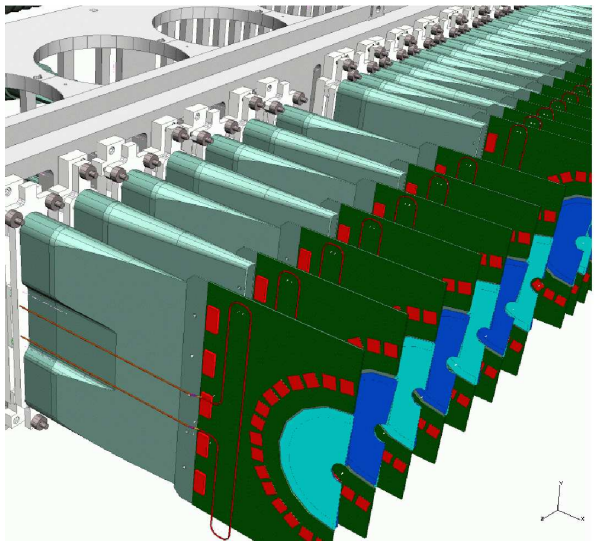

Figure 2.4: An impression of the left hand side of the Vertex Locator (VELO) detector showing the silicon sensors [43].

The silicon Vertex Locator (VELO) covers the area around the interaction point where the two proton beams collide. It provides track measurements around the primary vertex and allows displaced secondary vertices to be reconstructed. These secondary vertices are a feature of b-meson decays and allow the particle lifetime and impact parameter to be measured.

The VELO data are used in the high level trigger which selects events containing interesting B-meson decays. The size and position of the VELO is such that the full angular

acceptance of all downstream detectors is covered (15 mrad - 390 mrad). In addition to this the VELO has partial coverage of the backward hemisphere, used to provide primary vertex measurements. Because B hadrons have a mean decay length of $\sim$10 mm [41] the sensitive area of the VELO must be close to the beam axis ($\sim$8 mm). To avoid damage during beam injection the VELO is formed from two retractable sections allowing the sensors to be moved back 3 cm from their nominal position.

The Vertex Locator makes use of silicon strip detectors. Silicon is relatively inexpensive, with excellent spatial resolution and response time [44]. Charged particles traversing the sensor produce electron-hole pairs in the silicon. These are separated and collected by a reverse-biased external electric field. Charge collection at the anode and cathode produces a current pulse which signals a particle detection and gives a measure of the particle's energy.

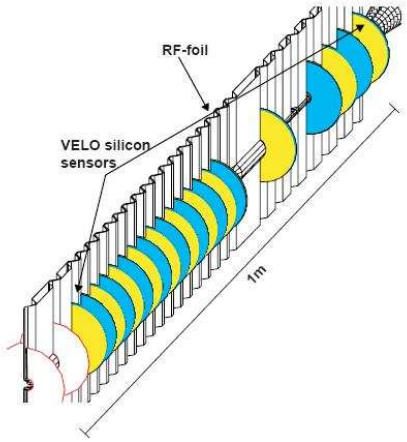

Figure 2.5: A schematic of the RF foil which runs parallel to the beam axis. The silicon sensors can also be seen.

The VELO comprises 21 stations, each of which has 2×2 sets of semicircular sections made from 300 μm silicon strips. These are separated by a Radio Frequency (RF) shield of corrugated metal foil running parallel to the beam axis. This separates the primary and secondary vacua. Sections overlap slightly to form circles of radius 34 mm, shown in Fig 2.5.

Each VELO station has one radial (R) and one angular (ϕ) measuring sensor, seen in Fig. 2.6. The R sensor has 512 strips arranged in four sectors of 45^o with constant-radius separation. This ensures that the smallest pitch is close to the beam axis where greatest

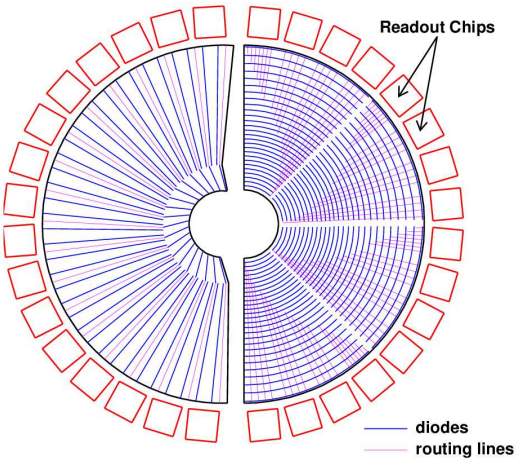

Figure 2.6: The arrangement of sensors in the VELO. Only sensors on one side of the RF foil are shown here. The RF foil separates the LHC vacuum and the detector vacuum [40]

accuracy is needed. It also ensures that the occupancy is balanced. This configuration is important for the L1 trigger as it is most efficient to reconstruct all tracks in the r-z projection and then fully reconstruct only those tracks with a high r-z impact parameter. Two R sensors placed upstream of the interaction point act as a pile-up veto. The pile-up veto uses the radial measurements of track positions and for any two given points the vertex is calculated for all possible combinations. From these the Primary Vertex positions are determined and any events with multiple Primary Vertices are rejected. The ϕ sensors consist of straight strips which are divided into inner and outer areas to equalise occupancy. The inner area is at a stereo angle of 10° while the outer is at 20°. The left and right detector halves overlap, aided by corrugations in the RF shield.

The VELO achieves a resolution of 42 μm in the z-direction, and 10 μm perpendicular to the beam [45]. For tracks with a high transverse momentum, an impact parameter resolution of 20 μm is obtained.

2.3.2 Magnet

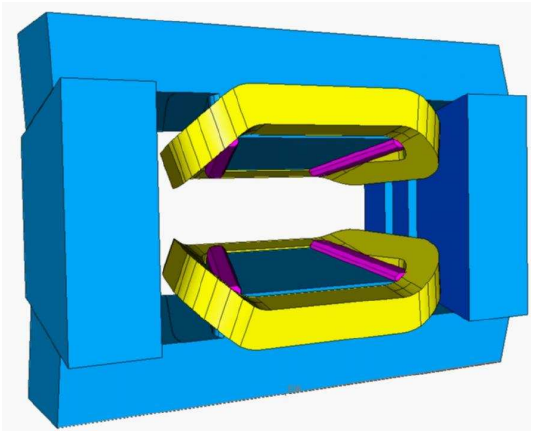

Figure 2.7: The LHCb dipole magnet. This is a warm magnet which allows the momenta of charged particles to be determined.

The LHCb dipole magnet is shown in Fig. 2.7. It is formed from two coils supported on an iron "window-frame" yoke and provides magnetic fields for momentum measurements [46]. It is a warm magnet and does not require cryogenic cooling. This permits easy ramping of the field and frequent field inversion as well as being significantly cheaper to manufacture than a cryogenic magnet. The pole faces are shaped to follow the acceptance angles of the experiments. The magnet provides a bending power of 4 Tm for tracks originating at the interaction point. The fringe region of the magnetic field extends as far upstream as the VELO to allow its use in the trigger together with the trigger tracker.

2.3.3 The Trigger Tracker

The Trigger Tracker (TT) is used to reconstruct the trajectory of low-mass particles which would be swept away by the magnetic field before reaching T1. It also provides transverse momentum information for tracks with large impact-parameters, used for triggering [40]. The TT station is composed of silicon sensors measuring 500 μm thick and 11 cm$\times$7.8 cm in area. A detailed description is given in reference [40]. The sensors have a strip pitch of 198 μm and are combined into "ladders". Depending on the position within the detector ladders of 5, 6 or 11 or 12 sensors are used. Short ladders of five or six sensors are used above and below the beam pipe, while longer ladders of eleven or twelve sensors are used in areas to the left and right of the beampipe. These ladders are arranged into four layers,

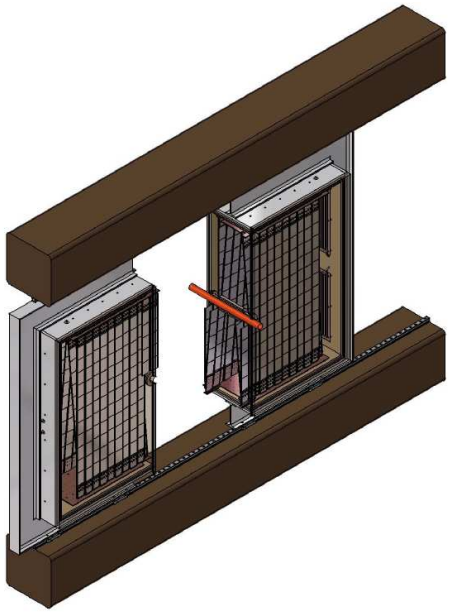

Figure 2.8: The front view of a layer in the Trigger Tracker (TT) [40].

made from ladder pairs with a 30 cm gap between the second and third layer. The first and last layers have vertical readout strips to measure the x-coordinate of tracks. The readout strips in the second and third layers are rotated by a stereo angle of $+5^o$ and -5^o from vertical respectively allowing the y-coordinate to be measured. A total of 180k readout channels are used for the four detector layers. The momentum resolution is expected to be in the range 3-6 per mill, depending on the momentum of the particle [47]. The nominal resolution on position is 50 μm [48].

2.3.4 The Tracking Stations

The tracking stations T1-T3 are situated at equal distances along the beamline in the field-free region behind the magnet (see Fig. 2.2). Together with the VELO and the Trigger Tracker they form the particle tracking system for the LHCb [49].

The particle flux is very high near the beam region but falls off quickly with distance. Due to this, the tracking stations are divided into two distinct areas with different detector technologies. The inner regions will be covered will a fine grained Inner Tracker, and the remaining 98% of the surface will be covered by the more coarsely grained Outer Tracker. In order to have full acceptance coverage the sensitive areas of the Inner Tracker

modules slightly overlap with each other and with adjacent Outer Tracker modules in both horizontal and vertical directions. The arrangement of the stations can be seen in Figs. 2.9 and 2.10.

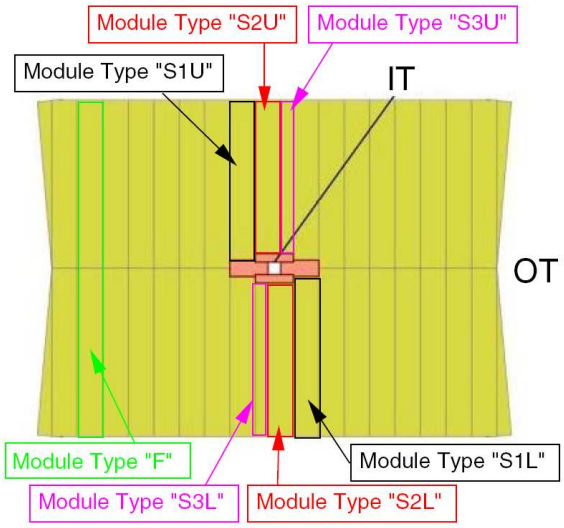

Figure 2.9: A schematic of a tracking station showing the Inner Tracker (IT) and Outer Tracker (OT) with different types of Outer Tracker modules indicated [49]. The tracking station is 450 cm high and 595 cm wide [50].

The Inner Tracker covers a cross-shaped area around the beam pipe, approximately 120 cm wide and 40 cm high, and comprises of a total of 504 identical silicon strip sensors. It covers areas where higher fluxes of up to 5×10^5 cm^{-2}s^{-1} are expected and is more granular to ensure that hit occupancies are not more than a few percent. Each silicon sensor has an area of 11×11.8 cm^2 and thickness 320 μm. Sensors have a pitch of 200 μm and are grouped into equal numbers of one- and two-sensor "ladders" which are read out as one unit. This is a similar system to the Trigger Tracker, discussed above. Layers of seven staggered ladders are arranged into four detector boxes. Each detector boxes contains four layers, with all ladders in a box mounted on a common cooling plate, giving an overall sensitive surface of 4.2 m^2.

Particle detection in the Outer Tracker region is carried out by gas-filled straw tubes. These work on similar principles to multiwire proportional chambers. The outer surface of each tube is maintained at a negative high voltage. An anode sense wire runs along the centre and is maintained at virtual ground. Charged particles will ionise the gas

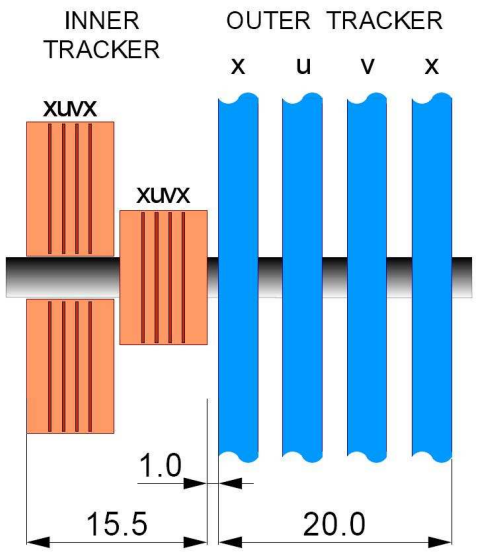

Figure 2.10: A schematic showing the top view of one of the tracker stations [47]. Layers marked as x are vertical. The u and v layers are rotated by a 5° stereo angle clockwise and anticlockwise respectively with respect to this. Dimensions are given in cm.

creating electrons which drift to the sense wire under the applied voltage. The high electric field near the wire causes the electrons to multiply, amplifying the signal. This causes a detectable pulse induced on the sense wire. Straw tubes can be used in high-rate environments as each wire has a separate source of electric field and broken wires only affect a single tube [51], [52].

The Outer Tracker straw tubes are made from a carbon-doped polyimdide (a heat- and chemical-resistant plastic) with an inner diameter of 5.0 mm, and a wall thickness of 75 μm. Each tube is 4.7 m long and is filled with $Ar/CF_4/CF_2$ in the ratio 75:15:10 [41], [53]. The gas was chosen to optimise the drift time - the total time from avalanche to preamplifier can be less than 50 ns (i.e. two bunch intervals) [50]. Read out is by means of a custom made time-to-digital converter (TDC). This gives a measurement of the drift time of the electrons in the gas, and hence the position of the ionising particle.

The Outer Tracker stations are made from a series of separate modules. The basic elements of each module are the sandwich panels on which straw tubes are mounted in two staggered layers 5.5 mm apart. Standard modules contain 64 straw tubes per layer, with modules of 32 tubes per layer occurring above and below the Inner Tacker acceptance area (see Ref. [50]). Each module is hermetically sealed with its own electronic readout and high

voltage power supplies. To allow installation around the beam-pipe the modules are mounted on a frame which is separated into halves.

The tracking stations are optimised for momentum measurements and are expected to have an average momentum resolution (δp/p) <0.6% over a wide momentum range (5<p<140 GeV/c), shown in in Fig. 2.11 [49].

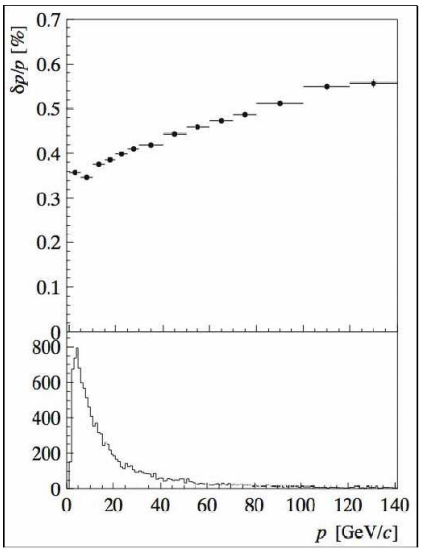

Figure 2.11: The momentum resolution of a reconstructed track as a function of momentum (top). The typical momentum of a B decay particle is shown for comparison (bottom) [50].

2.4 Particle Identification

Particle detection in the LHCb experiment occurs in three stages. The calorimeter is used to detect particles with high transverse momentum, muon chambers identify muons, and the two RICH detectors identify charged particles.

2.4.1 The Ring Imaging Cherenkov (RICH) detectors

Two Ring Imaging Cherenkov Detectors (RICHs) provide charged particle identification for the LHCb experiment. RICH 1 is situated downstream of the VELO and provides particle identification over the momentum range 1-60 GeV/c. The full acceptance of the LHCb experiment is covered, from 10 mrad to 300 mrad horizontally and 250 mrad vertically. The RICH 1 detector is placed close to the interaction point to minimise the area required (2 m×3 m). Because of its positioning between the VELO and TT station its longitudinal size is limited to 1 m. RICH 2 is located after the tracking stations and will separate kaons and pions at energies up to 100 GeV.

Both RICH detectors work by imaging Cherenkov radiation. Cherenkov radiation is produced when charged particles travel through a medium m of refractive index n faster than the speed of light in that medium ($c_m = c/n$). As the charged particle passes, its electric field distorts the neutral atoms of the medium [54]. This causes a temporary local polarisation and the distorted atoms act as dipoles. The particle will create a brief electromagnetic pulse at each region as it passes through the medium. Due to the symmetry of the field surrounding the charged particle there will be no resultant field at large distances and no radiation if the particle is travelling at a velocity less than c_m. However, if the charged particle is moving at a speed larger than c_m there will be a resultant dipole field along the axis of motion. Each charged particle passing a given point will set up its own field and the radiated light from all parts of the track may interfere constructively. This

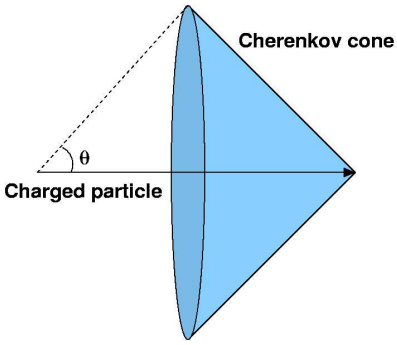

Figure 2.12: The cone of light emitted during Cherenkov radiation.

produces radiation in a characteristic cone shape which can be seen in Fig. 2.12. The condition for constructive interference is shown in equation 2.1, where β is the velocity of the charged particle divided by c, the speed of light in a vacuum. Radiation will be visible at the Cherenkov angle θ_c.

$$cos\theta_c = \frac{1}{\beta n} \tag{2.1}$$

In the RICH detectors Cherenkov photons will be brought out of the LHCb acceptance using tilted spherical mirrors. The Cherenkov photons will be imaged and read out by arrays of photodetectors. Magnetic shielding around the photodetectors will attenuate the magnetic field by a factor of 25 to limit image distortion. Depending on the speed of the particle and the refractive index of the medium, different sizes of ring will be formed. Fitting to these rings enables the speed of the particle to be determined. Combining this information with momentum measurements from the tracker gives the particle's mass. This enables charged particle identification, particularly K-π separation. A simulation of the rings expected in both RICH counters is shown in Fig. 2.13, with fitted rings superimposed in red. Circles are slightly elliptical due to the tilt of the mirrors which bring the image out of the detector acceptance.

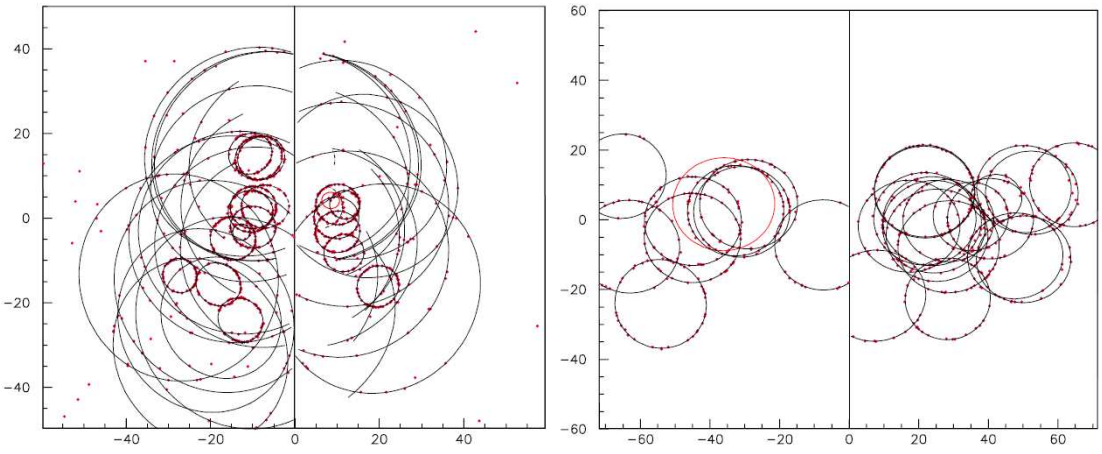

Figure 2.13: Cherenkov rings in a simulated event ($B_d \rightarrow \pi^+\pi^-$). The same event is shown for the RICH 1 planes (shown side-by-side, left) and the RICH 2 planes (right) [55].

In order to cover the full momenta range two RICH detectors are used, with three different radiators. Fig. 2.14 shows the angular distribution of charged particles in the LHCb detector. RICH 1 is optimised for low-momentum particles at wider angles while RICH 2

is optimised for higher momentum particles closer to the beamline.

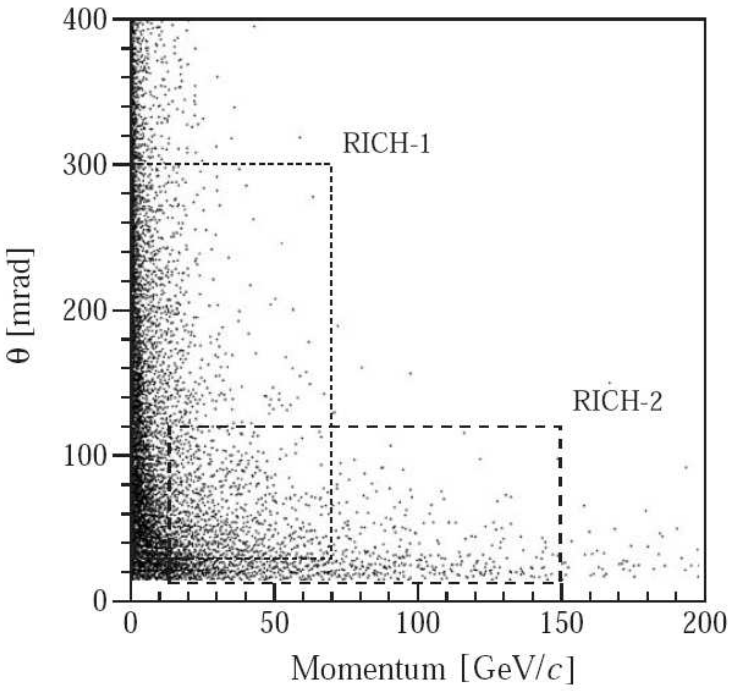

Figure 2.14: The polar angle (θ) of a charged particle versus the momentum of the particle in GeV/c [56].

It can be seen from Equation 2.1 that Cherenkov photons will be produced when $\beta > \beta_t = 1/n$, giving a velocity and hence momentum threshold characteristic to different types of particle. The characteristics of the radiators used are summarised in Table 2.1.

Radiator:	Aerogel	C_4F_{10}	CF_4
Refractive Index (n)	1.03	1.004	1.0005
Number of photoelectrons (N_γ)	6.6	32.7	18.4
Cherenkov angle (θ_C) (mrad)	242	53	32
π Momentum threshold (GeV/c)	0.6	2.6	4.4
K Momentum threshold (GeV/c)	2.0	9.3	15.6

Table 2.1: The properties of the different Cherenkov radiators [57]

2.4.1.1 RICH 1

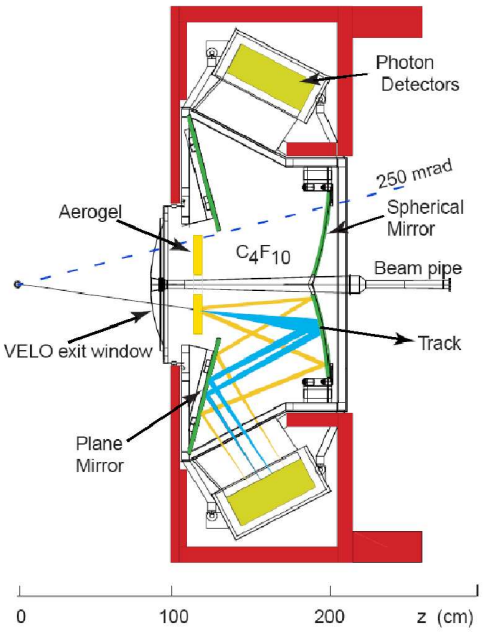

Figure 2.15: A schematic showing the side view of the RICH 1 detector [40].

RICH 1 is located upstream of the magnet to cover the low momentum range. It is exposed to a fringe field of around 60 mT, improving track momentum measurement, and covers the full angular acceptance of the spectrometer. Two Cherenkov radiators are used to cover the required momentum range of 1-60 GeV/c. Aerogel tiles of 5 cm thickness are situated immediately after the entrance window. This radiator has a refractive index of n=1.03 and provides positive kaon identification above 2 GeV/c and π-K separation up to 10 GeV/c. A gas Cherenkov radiator (C_4F_{10}) is also used. This has a refractive index of 1.0014 at standard temperature and pressure (STP) and provides π-K separation up to 60 GeV/c. The Cherenkov light produced in the radiators is focused by spherical mirrors of radius 2400 mm. These are made from a 2 mm thick carbon-fibre composite coated with aluminium and have a radius of curvature of 2700 mm [58] [59]. Secondary plane mirrors reflect the ring images onto arrays of photodetectors. The plane mirrors are formed from 6 mm thick borosilicate glass (Simex) [59]. The plane mirrors are arranged in halves above and below the beam with each half measuring 1500 mm$\times$775 mm and composed of eight 1500 mm$\times$775 mm segments. This arrangement of mirrors positions the photodetectors outside the spectrometer acceptance, and ensures that the photodetector material does not

degrade the tracking and calorimetry. The photodetector array is formed from pixellated Hybrid Photon Detectors (HPDs), discussed further in Chapter 3. The total radiation length for RICH 1 including the entrance and exit windows, mirrors and both radiators is estimated to be around 0.07 X_o.

2.4.1.2 RICH 2

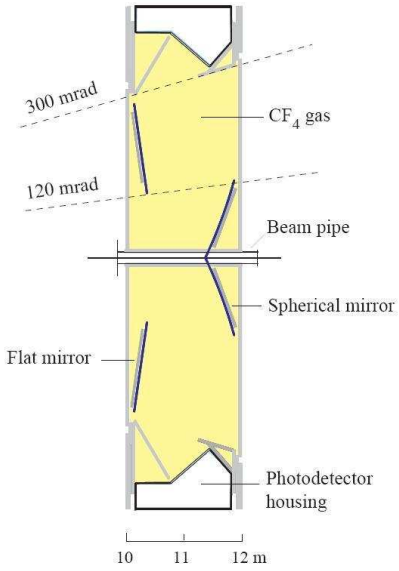

Figure 2.16: A schematic showing the side view of the RICH 2 detector [55].

RICH 2 is located after the tracking stations and separates kaons and pions at energies up to 100 GeV. As it is optimised to detect high momentum particles that have traversed the magnet it covers a more limited acceptance of 15-120 mrad horizontally and 100 mrad vertically. The radiating gas is CF_4 at STP with a refractive index of n=1.0005. The Cherenkov light produced is focused using spherical mirrors, tilted to keep the photodetector out of the spectrometer acceptance. Secondary flat mirrors reflect the image on the photodetector plane. The spherical mirror array is formed from 56 hexagonal borosilicate glass mirror segments, and has a radius of curvature of 8000 mm. The plane mirrors are made from rectangular segments measuring 437×437 mm^2. The plane mirrors for RICH 1 and 2 are made in the same process and from the same material (borosilicate glass). The total radiation length for RICH 2 including the entrance and exit windows, mirrors and radiator, is estimated to be 0.124 X_o.

For both RICH detectors, the electron and μ identification efficiency is expected to be $\sim$95% with π misidentification rate of $\sim$1%, while the K/π detection efficiency will be $\sim$90%, with a misidentification rate of <10% for 10-80 GeV/c tracks [41]. (Here, the efficiency refers to the probability of correctly identifying a particle, e.g. correctly identifying a kaon as a kaon. The misidentification rate refers to the probability of identifying a particle as another particle, e.g. identifying a kaon as a pion.) The RICH detectors will significantly improve the performance of the LHCb detector. As an example, the B_s mass peak from the decay $B_s \rightarrow D_s^- K^+$ is shown in Fig. 2.17 with and without information from the RICH detectors.

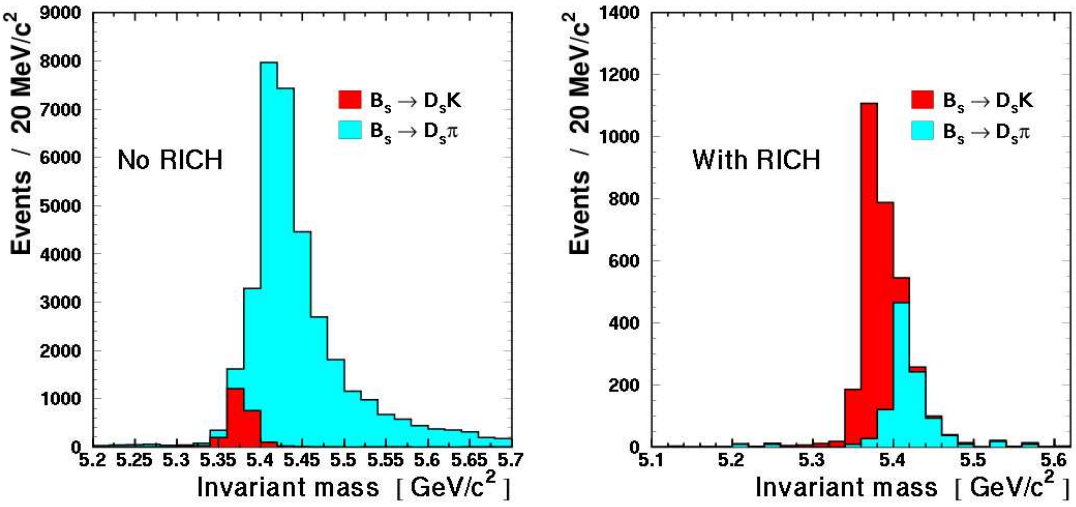

Figure 2.17: The invariant mass separation of the decays $B_s \rightarrow D_s K$ and $B_s \rightarrow D_s \pi$. Without information from the RICH detectors the decays are indistinguishable (left). Using information from the RICH detectors the background from the $B_s \rightarrow D_s \pi$ decay is reduced considerably (right). This is due to the efficient K-π separation provided by the RICH counters.

It can be seen that in the absence of particle identification from the RICHs the background from $B_s \rightarrow D_s^- \pi^+$ is dominant, which has a branching ratio 10 times higher than the signal channel. However the RICH detectors allow the K and π to be separated, leaving the signal dominant [60].

2.4.2 The Calorimeter

The LHCb Calorimeter consists of four subdetectors: The Scintillator Pad Detector (SPD) and Preshower Detector (PS) find the charge and electromagnetic nature of a particle, while the Electromagnetic and Hadron calorimeters provide energy and position measurements for showering particles [61]. Measurements are obtained for charged particles such as electrons and neutral particles such as photons, hadrons and neutral mesons (π^o and K^o) which are not picked up during the charged particle tracking. All of the calorimeter subdetectors have similar technology with scintillating tiles and wavelength shifting fibres, allowing similar electronic readout. The arrangement of these subdetectors can be seen in Fig. 2.2. The tiles are arranged in three regions of different pad size, depending on their distance from the beam axis. Cells in the outer region measure 121.2 mm×121.2 mm , cells in the middle region measure 60.6 mm×60.6 mm, and cells in the inner region measure 40.4 mm×40.4 mm. This arrangement allows good spatial resolution near the beam. To avoid radiation damage and to keep occupancies low, the calorimeter detectors only extend to within 30 mrad of the beamline. The calorimeter is important for the fast first level (L0) trigger which identifies high transverse momenta particles as well as providing information for offline reconstruction.

2.4.2.1 Scintillator Pad Detector

The Scintillator Pad Detector (SPD) uses 15 mm thick scintillator pads, made from a polystyrene-based plastic which produces fluorescent light when ionised by charged particles or electromagnetic radiation [62]. Charged particles will produce ionisation in the scintillator, enabling them to be separated from neutral particles which will not [63]. Scintillator light is collected by wavelength shifting fibres which are read out by multianode photomultpilers. A range of 1-100 minimum ionising particles (MIPs) is covered, with 25 photoelectrons produced in response to one MIP. This enables separation between electron and photon showers. The SPD measures 6.2×7.6 m^2 and comprises 6000 cells. The total depth in Z is 180 mm, i.e. around 2.0 radiation lengths (X_o).

2.4.2.2 Preshower Detector

The plane of the SPD sits in front of the preshower detector. The preshower detector consists of a 12 mm ($\approx 2X_o$) lead converter which allows e-γ separation, followed by a scintillator plane. The same 15 mm scintillating pads are used as in the SPD detector and the same geometry of increasing pad size with distance from the beam is used. Both the scintillator pad detector and the preshower detector signal the presence of charged particles. The SPD is used to improve electron triggering, while the PS is used to reject the high charged-pion background.

2.4.2.3 Electromagnetic Calorimeter

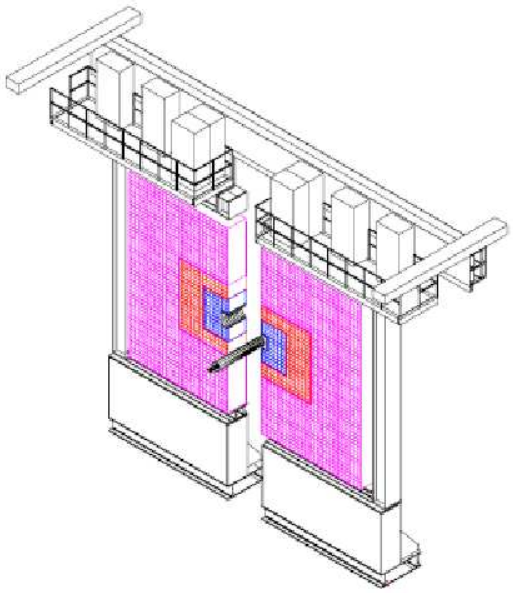

Figure 2.18: A schematic showing the Electromagnetic Calorimeter (ECAL) detector. The regions of different pad sizes are shown as different colours [65].

The Electromagnetic Calorimeter (ECAL) is situated downstream of the preshower detector and is used in coincidence with the SPD and PS to identify electrons and photons [61]. It is also important in the reconstruction of π^0 and η particles. It has and area of 6.3×7.8 m^2 and a depth of 835 mm ($25X_0$) for optimum resolution of high-energy photon showers [64]. It is made from 4 mm scintillator tiles separated by 2 mm lead plates, through which wavelength shifting fibres pass like a "shashlik" or shish kebab. The scintillating

plates are segmented and correspond to a size from 1-3 Moliere radii [61]. Each module has 66 lead plates and scintillators and a total of 6000 scintillator tiles are used. The cell sizes vary with distance from the beam and have the same measurements as the SPD/PS cells. There are a total of 5952 channels. The energy resolution is expected to be $\sigma_E/E \sim$ 10% covering a dymamic range of 0-10 GeV [65].

2.4.2.4 Hadron Calorimeter

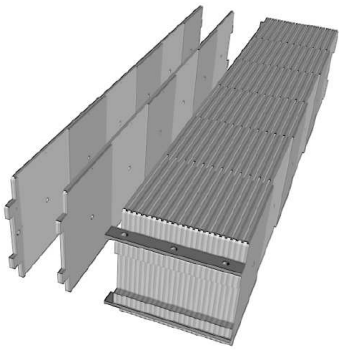

Figure 2.19: A schematic showing the Hadronic Calorimeter (HCAL) detector. An expanded view of the iron plate and scintillator layers can be seen.[4] The HCAL covers an area of 6.9×8.4 m^2 and extends to 1655 mm in the z-direction [65].

The Hadron Calorimeter (HCAL) is a scintillating tile calorimeter situated downstream of the ECAL, and its main purpose is to provide data for the first level (L0) trigger. It covers an area of 6.9×8.4 m^2 and extends to 1655 mm in the z-direction. It is formed of 16 mm iron plates sandwiched between 2 mm thick scintillating tiles and runs parallel to the beam axis. At total of 26 modules consisting of 1468 cells are used. These are larger than cells of the other calorimeter subdetectors and are split into two regions. Cells in the outer region measure 262.6×262.6 mm^2 and cells in the inner region measure 131.3×131.3 mm^2. The spacing between the tile is of the order of $1X_0$, allowing electromagnetic cascades to develop. The HCAL covers an energy range of 0-10 GeV and is expected to have a resolution of $\sigma_E/\mathrm{E} = 80\%\sqrt{E}\oplus$ 1.5%.

2.4.3 Muon System

Accurate muon identification is very important for LHCb, as muons are contained in many CP-violating decays. The muon detector provides muon identification and triggering information for high-P_T muons. Muons in semileptonic decays also provide an important flavour tagger, used for track reconstruction. Knowing the charge of the muon allows the flavour of the b-quark and hence the B-meson to be determined. For example a negatively charged muon in the decay corresponds to a $\overline{b}$ quark and so a B^0 meson.

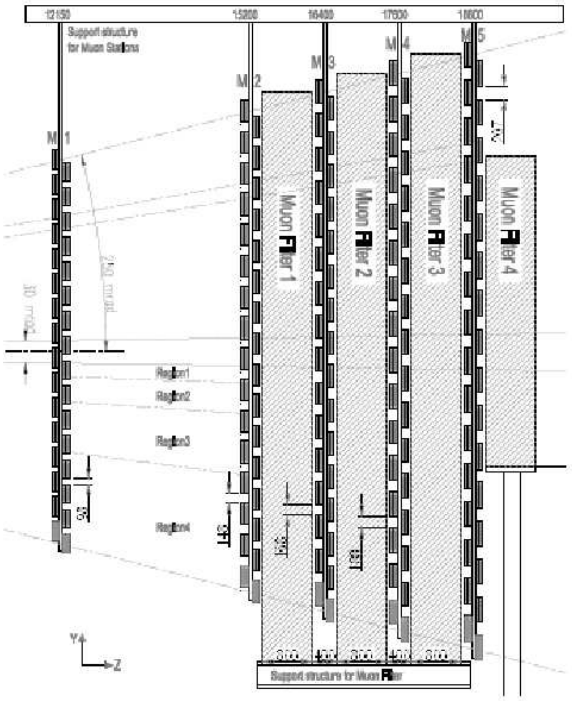

Figure 2.20: A schematic of the muon detector showing the side view. There are five muon stations (M1-M5). M1-M3 use Multiwire Proportional Chambers while M4-M5 use Resistive Place Capacitors. The regions 1-4 are defined by the pad sizes [66].

The muon detector is formed from five separate stations, M1-M5. M1 is located in front of the calorimeter, and M2-M5 are behind it. The final three stations are separated by four iron absorbers of 80 cm to attenuate hadrons, electrons and photons, with a total absorber thickness of 20 X_o. The muon chambers use two different technologies depending on the occupancy. The first three stations use Multiwire Proportional Chambers (MWPC) consisting of parallel, equally spaced ground wires between two negatively charged cathode plates which are separated by a 5 cm gap. The gap is filled with a non-flammable mixture

of Argon,CO_2 and CF_4 gas in a ratio of 40:50:10, producing an average of 50 e^- for a muon crossing. Ionising particles are detected by collecting the charge produced in the gas. Each chamber contains four sensitive gaps, functioning as two double gaps to provide redundancy, providing an efficiency of ∼99%. The lower particle rate in the outer regions of the last two stations means that resistive plate capacitors (RPCs) are suitable. These are formed from resistive electrode plates, separated by a gas gap of 2 mm. The gas used is a mixture of $C_2H_2F_2$, C_4H_{10}, and SF_6 in the proportion 95:4:1. Muons ionise the gas, creating a multiplication of the order of 10^7. Because this avalanche grows very fast, the RPCs have excellent timing properties [66]

2.5 The Trigger System

The trigger serves to extract the small fraction of events containing interesting B decays (around 1 in 160). Interesting events are recognised by several characteristics. Because the b-quark has a relatively high mass, decays containing bs are expected to have a high transverse momentum. Due to the long lifetime of the B hadron ($\sim$ 1.6 ps) there will also be secondary vertices detached from the primary vertex [61].

The **First Level Trigger (LO)** is a pure hardware trigger made using custom electronics which runs at 40 MHz, synchronous to the LHC bunch-crossing frequency,. It aims to reduce the initial 10 MHz of visible $b-\overline{b}$ collisions to a rate of 1 MHz [67]. The L0 trigger exploits the fact that B hadrons are relatively heavy and so will decay into heavy particles with large transverse momentum (P_t). High-P_t particles are identified using information from the calorimeter and muon systems.

A number of separate channels are considered: muon, dimuon, hadron, electron and π^0 [68]. Muons are triggered on if the momentum of one muon in an event is higher than a threshold of $\sim$1.1 GeV/c. A dimuon trigger is issued if two muons in an event pass this threshold. Events with low particle multiplicity and few interactions will cause a hadron trigger to be issued, provided that there is a hadron cluster with a transverse momentum greater than 3.5 GeV/c [67]. The output rate is around 200 kHz for the muon and dimuon channels and around 700 kHz for the hadron channel. The L0 trigger has $\sim$50% efficiency for hadronic channels, $\sim$90% for μ channels and $\sim$70% for radiative channels [41]. It has a total latency of $\sim$ 4 μs, with a further 1ns latency added due to the reconstruction algorithms of the calorimter and muon system [68].

The **Level One Trigger (L1)** was initially planned as an off-detector electronic trigger. It was to reduced the data rate by a factor of $\sim$25 using information from the L0 trigger, the VELO and the trigger tracker. It aimed to reconstruct tracks in the VELO and match them to a L0 or Calorimeter cluster in order to identify them and measure their momenta. Tracks with a large transverse momenta and high impact parameter were triggered on. The L1 has since been combined with the High Level Trigger (HLT), but is still used for processing DC04 Monte Carlo data.

The **High Level Trigger (HLT)** is a software trigger which uses specialised algorithms to reduce the initial data rate to a suitable level to write to tape. Three dimensional pattern recognition separates events which contain b-hadrons from any minimum bias background which has passed the L0 trigger. Separate "alleys" exists for each of the trigger types from L0: muon, dimuon, hadron, electron and π^0. 85% of events will only trigger one of the requirements and hence will only be processed in one alley [68]. Around 10 kHz of events will pass at least one of these trigger alleys. This rate is low enough so that tracks can be reconstructed by the inclusive trigger, which reconstructs composite particles. There is also an excluive trigger which fully reconstructs certain final B-states, for example $B_s \to \phi\phi$. The final HLT decision is a logical-OR of the inclusive and exclusive trigger decisions. The HLT has a total output rate of ~ 2 kHz [45].

Chapter 3

Hybrid Photon Detectors

3.1 Hybrid Photon Detectors (HPDs)

Cherenkov light in the RICH detectors will be observed using arrays of Hybrid Photon Detectors (HPDs). HPDs are a hybrid between photomultipliers and solid-state technology, and have been developed in a collaboration between industry and CERN.

Figure 3.1: A Hybrid Photon Detector (HPD). Scale shown =10 cm.

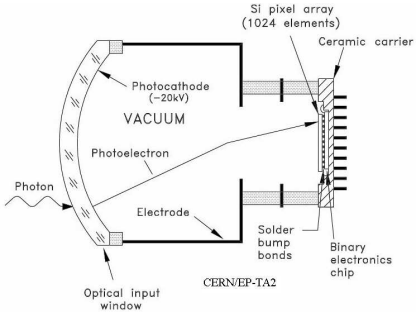

Figure 3.2: A schematic drawing of an HPD showing the production and acceleration of photoelectrons.

3.1.1 HPD Properties

An HPD is shown in Fig. 3.1[1] with a scale of 10 cm. It is formed from an evacuated metal tube with a base of diameter 87 mm, sealed with a quartz window. The quartz

[1]Taken from http://kwyllie.home.cern.ch/kwyllie/LHCBPIX1doc/wylliebeaune2005.*ppt*

window is coated on the inside surface with an S20 multialkali photocathode. Cherenkov light produced by charged particles will enter the HPD through this window producing photoelectrons with wavelengths of 200-800 nm [41]. The typical integrated quantum efficiency is $\sim \int$QEdE= 0.7 eV and HPDs are most sensitive in the UV at 270 nm. The photoelectrons are accelerated and focused through a 20 kV electrostatic field, as shown in Fig. 3.2[2]. They then strike a pixellated silicon sensor in the base of the tube creating around 5000 e^--hole pairs. This sensor chip forms the anode and was developed jointly by the LHCb and ALICE experiments (see Chapter 2). It has a sensitive area of 16×16 mm^2 and is divided into 8192 "ALICE" pixels. These are arranged in 32 columns by 256 rows and measure 500 μm horizontally and 62.5 μm vertically. In ALICE mode each pixel is read out individually in a column-wise fashion. In "LHCb" mode logic circuits on the chip OR the binary signal from eight ALICE pixels together to create a square LHCb pixel of 500 μm × 500 μm. This group of ALICE pixels then acts as an individual pixel and is read-out as a single unit. Pixel cells have an analogue front-end and digital back-end which require separate power supplies [69].

A photoelectron striking a pixel creates a "hit" if a current above a certain threshold is produced. This threshold is set in the course of testing to a value which minimises noise but maximises signal. The resulting signal is digitised by a bump-bonded readout chip. The analogue HPD signal is converted to a binary signal, shaped and amplified. When given an external trigger the binary data is buffered and read out at the rate of one row per clock cycle. The chip also contains a JTAG[3] serial interface, control and biasing and the threshold circuit for each pixel.

3.1.2 HPD Production

Production takes place in several separate stages. The first step is the fabrication of the 750 μm thick silicon wafers used to make the binary readout chips. These undergo testing with a specialised probe station allowing good dies to be selected. The wafer is diced by IBM in France forming readout chips. The sensor chips are fabricated on 300 μm thick silicon wafers at Canberra in Belgium. Both the sensor and readout chips are then sent to VTT in Finland where they undergo high temperature bump-bonding to form an

[2]Taken from http://tilde-gys.web.cern.ch/ gys/LHCb/PixelHPDs.http.

[3]JTAG stands for Joint Test Action Group and is a standard interface for testing digital circuitry.

assembly. The assembly is tested electronically and a process of irradiation is used to check the quality of the bump bonds. In parallel to this, ceramic carriers are produced by Kyocera in Japan. The carriers are brazed to a Kovar ring at Photonis (formerly Delft Electronics Products, or DEP) in the Netherlands [70]. This ring will be attached to the tube body. Gold-plating occurs at CERN, followed by a visual inspection to check the quality of the plating. The assemblies are then packaged to the ceramic carriers by HCM in France, forming the anode. Lastly, the completed anode undergoes electronic testing [71], [72].

The HPD tube body is manufactured at DEP, where is coupled to the anode. The photocathode is deposited on the quartz window and the tube then undergoes vacuum sealing. A "bake-out" at $\sim$300°C removes residual gases. Finally the tube is cabled and potted to a plastic base for mechanical fixture.

3.2 HPD Testing

Facilities have been set up at the universities of Edinburgh and Glasgow to test the 550 HPDs needed for the RICH detectors. The design and operation of these test stations will be discussed in this chapter. The main purpose of testing is to ensure HPDs meet contract specifications, and the results of the standard tests allow HPDs to be placed in one of five categories (A^+, A, B, E or F). All 550 HPDs have been tested over the course of 18 months.

3.2.1 Test Stations

In order to test the HPDs four identical stations have been set up, two in Edinburgh and two in Glasgow. One station in each test centre is used for the standard tests performed on all HPDs. The second is used for extended tests on a sub-sample of HPDs and as a fallback for standard testing if the first station develops a hardware failure.

One of the test stations at the University of Edinburgh is shown in Fig. 3.3. A test station consists of a light tight box, a series of power supplies and electronic circuits to power and control the HPD, and a data-taking PC. Tests are carried out with the HPD mounted inside

Figure 3.3: An HPD test station at the University of Edinburgh, showing the light tight box (left) and electronics (centre). The data acquisition PC can also be seen (right).

a light tight box because ambient light is intense enough to damage the photocathode. A photomultiplier tube placed inside the dark box is used to check that light levels are below a rate of 10 Hz before the HPD is switched on. A Keithly 6485 picoammeter measures the reverse bias current at the anode sensor, and an Agilent E6347A power supply provides and measures the bias voltage for the silicon chip. A Matsusada power supply provides high voltage (HV) of up to 20 kV which creates the electrostatic field in the HPD. This is distributed via a custom made voltage divider to the cathode, focus and zoom electrodes of the HPD. An interlock on the dark box ensures that the HV supply will drop immediately to 0 V if the box is accidentally opened with the HPD power switched on. When inside the dark box a blue LED (470 nm) is used to illuminate the HPD via a fibre optic cable. This provides an approximately flat light source and is tuned so that in each event an average of 2-4 photons are recorded in the HPD. The LED is controlled by a trigger box situated outside the dark box, which varies the duration and separation of the light pulses. It also allows the delay of the pulses with respect to the data taking trigger to be altered.

The HPD is controlled and the data read out by a PC, with the signals and data passing through a series of specialised printed circuit boards. The HPD is connected to the electronics via a zero insertion force (ZIF) socket on the side of the dark box. This is mounted on a mostly passive printed circuit board which receives and transmits signals to the HPD chip. Double-layer twisted pair cables connect the ZIF board to the next layer

of electronics, the MB[4] and FB[5] printed circuit boards [73].

The MB board generates the reference signals and supplies power to the pixel chip. These are transmitted via the ZIF board. The power supply voltages and currents are monitored using ADCs on the MB board. The MB adjusts the voltage levels of input and output signals to ensure the correct logic is used to communicate with external electronics. The HPD pixel chip produces signals using GTL[6] logic, which is translated to TTL[7] for use within the MB board and then to LVDS[8] for transmission to the FB board. The reverse happens for signals to the chip, which arrive to the MB board as LVDS and are converted to TTL and then GTL before transmission to the pixel chip. Configuration of the HPD and the MB board is achieved via a JTAG interface. JTAG is a commercial protocol [74] which provides TTL signals to set and monitor the voltage level on the MB board and HPD pixel chip. The MB board and FB board are connected with two twisted pair cables. The "Data" cable transmits the data from the pixel chip,via the MB board, and the "Control" cable transmits control signals from the FB board to the MB board.

The FB board is used to generate the clock signals and triggers needed by the HPD pixel chip. A Field-Programmable Gate Array (FPGA) on the FB board generates the signals used to read out the pixel chip, which are transmitted to the chip via the MB board. These include clock and reset signals and a test-pulse signal which allows the pixel chip to be triggered for testing purposes. In addition to this, the FB board also transmits the data it receives from the MB board back to the PC. The data are received via the "Data" channel from the MB board and formatted and buffered before transmission to the PC. Transmission of the serialised data occurs at a rate of 40 MHz via a shielded twisted pair cable. The S-link protocol [75] [76] is used and data are transmitted to a mezzanine receiver card. The receiver card is mounted on the FLIC[9] PCI card in the data-taking PC. The receiver card de-serialises the data and transmits it to the FLIC card. The FLIC card then writes the data to memory which is accessible by the PCI card. When requested to by software the FLIC card also generates the signals needed to reset or read out an event.

[4] after Mike Burns, who designed the board at CERN.
[5] after Francois Bal, who designed the board at CERN.
[6] GTL stands for "Gunning Transceiver Logic", a type of logic used in integrated circuits.
[7] TTL stands for "Transistor-Transistor Logic", a type of logic used in integrated circuits.
[8] LVDS stands for "Low-Voltage Differential Signalling".
[9] FLIC stands for "Flexible I/O Card"

3.3 HPD Test Programme

Each of the HPDs needed for the RICH detectors is shipped to Glasgow or Edinburgh to undergo a standard sequence of tests. This sequence consists of visual and mechanical tests to check the physical characteristics of the HPD and software-controlled tests which check the pixel chip operation and the performance of the full HPD. A subset of HPDs also undergo extended testing to measure their photocathode efficiency or the collection efficiency of the anode sensor. In this chapter the test sequence will be described in detail with typical screenshots shown where appropriate.

3.3.1 Visual and Mechanical Tests

Once an HPD arrives at a test centre it is visually inspected and cleaned. During handling and mounting care must be taken to not damage the HPD, and the person handling the HPD must wear a grounding strip to prevent electrostatic discharge. Unpowdered latex gloves are worn during handling. This avoids fingerprints and marks on the HPD surface which may cause microdischarges once the HPD is at high voltage. During cleaning any silicon remaining around the edges of the chip or on the pins at the base is removed using deionised water and a small brush. Excess water is blown off with bottled air, and the chip edges blotted. A check is made for bent pins. The HPD body and window are then cleaned using acetone, ethanol and dry air. A layer of teflon tape is placed around the indium lens seal, to prevent the uneven surface from generating discharges under high voltage. After this, a measuring jig is used to check that the size of the HPD tube and the angle at which it sits are within mechanical tolerances of ± 0.5 mm. The mechanical tolerance is important to allow HPD mounting within the LHCb detector.

3.3.2 Software-controlled Tests

Software has been written using Labview 7.1 on Windows XP. This allows automatic control of the test stations and provides monitoring and logging of the HPD output [77]. In addition, safety features can be implemented to minimise the possibility of human error, for example the maximum High Voltage (HV) ramping rate is set to be 50 V/s rising, 500 V/s falling, and 50000 V/s emergency falling. The software displays separate

monitors for bias voltage, HV, temperature and the status of the LED light source. These Virtual Interfaces (VIs) log the data they display and handle emergency ramping down of the high voltage if predefined limits on HV or bias voltage are passed. The bias voltage and HV will also ramp down at a slower (i.e. non-emergency) rate if the voltage set and the voltage which is read back differ by more than a certain amount. There is a "HV emergency stop" button which can be used to ramp down the HV if the operator notices anything unusual. In addition, environmental data such as ambient temperature are also displayed and logged by the VIs.

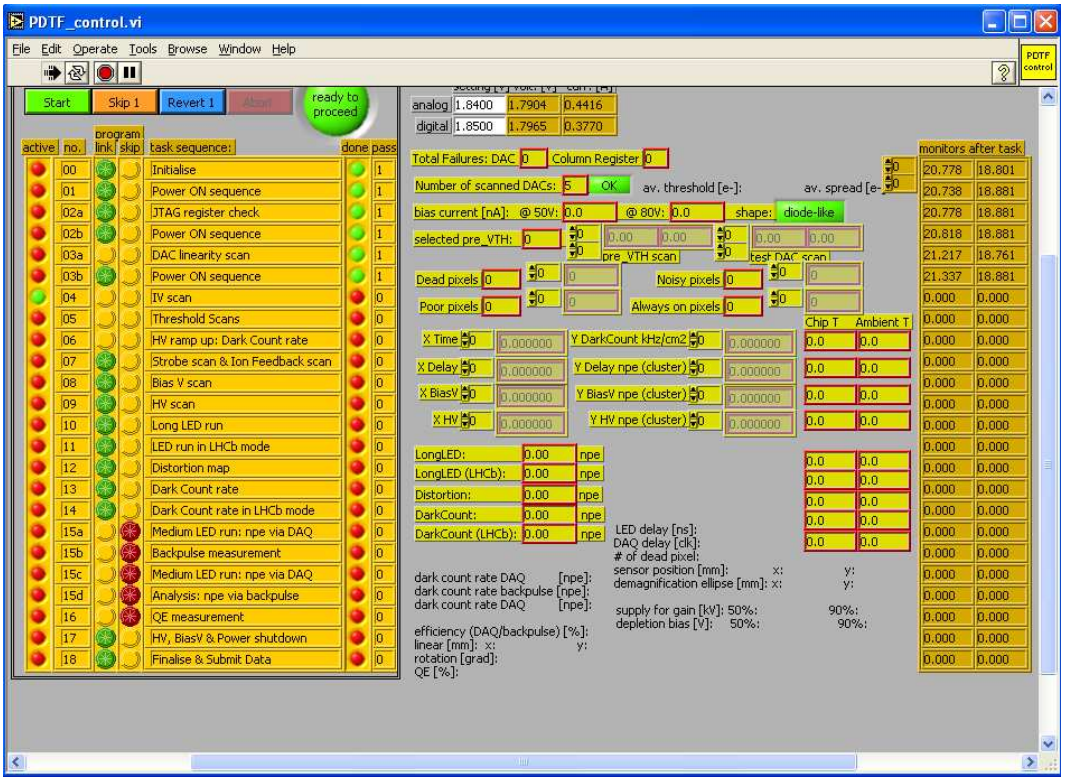

Figure 3.4: A screenshot of the main LabView control screen used for HPD testing. The sequence of test can be seen, along with the number of times each test has been performed ("pass"). A green light in the "active" column indicated which test is currently being performed. The analogue and digital currents (in mA) being supplied to the MB and FB boards are also shown at the top centre.

The main VI used in testing is the "PDTF_Control" VI, which monitors the sequence of tasks involved in a standard test sequence. A screenshot of this VI is shown in Fig. 3.4. Where appropriate it will automatically starts the next test in the sequence once the current test has finished running successfully. Analysis of the data taken at the test

stations is carried out under CYGWIN, using pre-complied C++ code.

3.3.3 Pixel Chip Operation

The first step of HPD testing is to verify the operation of the pixel chip before the HV is powered on. Tests are carried out which ensure that communication can be established between the data-taking PC and the pixel chip, and that pixel chip register can be set and read back.

- JTAG Register Check

  After initial powering on of the circuit boards and associated electronics communication with the chip and setting of internal registers is tested. A JTAG register check writes data to the chip and reads it back. Failure to write or read back data will show as a "stuck" bit on this scan.

- DAC linearity scan

  Next, a DAC linearity scan runs through the range of voltages and currents needed

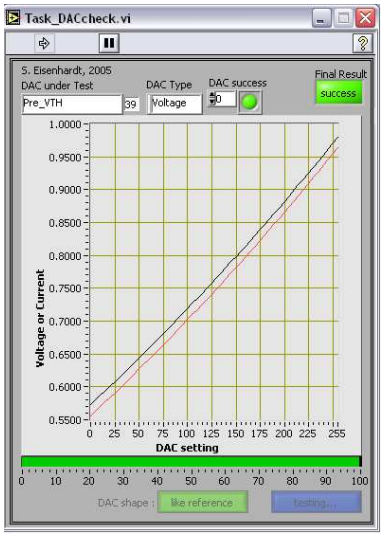

Figure 3.5: A screenshot of the DAC Linearity Scan. The x axis shows the DAC values which are set and the y axis shows the values read back. The red line is provided for reference, while data is shown with a black line. The result of this test is judged by the operator.

to set the values on a given Digital-to-Analogue Converter (DAC). A typical scan

is shown in Fig. 3.5. The user compares the output (shown as a black line) to a reference function displayed on the screen (shown as a red line) and if judged to be OK instructs the programme to continue. A linear output is expected but if the setting or read-back is faulty then the output of the scan will be a horizontal flat line, easily distinguished by the user.

- IV Scan

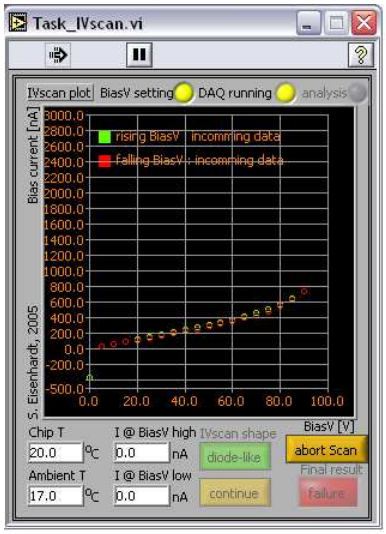

Figure 3.6: A screenshot of an IV scan showing the characteristic current response of the anode. The y axis shows the current drawn (nA) and the x axis shows the bias voltage applied (V).

The IV scan shown in Fig. 3.6 measures the characteristic current (I) response of the HPD anode to a range of bias voltages (V) from 0-90 V. This curve should be diode-like and is again judged by the user.

- Threshold Scan

The Threshold Scan is used to find the optimum setting for the voltage threshold. This threshold sets the level above which pixel hits will be recorded and is controlled by the DAC supply line "Pre_VTH". A pixel is counted as "hit" if the voltage pulse shaped from the collected charge exceeds this threshold value, causing the discriminator to fire. Testing is carried out in several stages. During the first stage the optimum global threshold (Pre_VTH) setting is determined. The next stages involve injecting a test-pulse of variable charge size at the input to the chip. This is implemented via the JTAG control, and triggers the pixels to fire. The four test steps are:

i. A coarse scan of Pre_VTH, with test-pulse injection. The operator is asked to

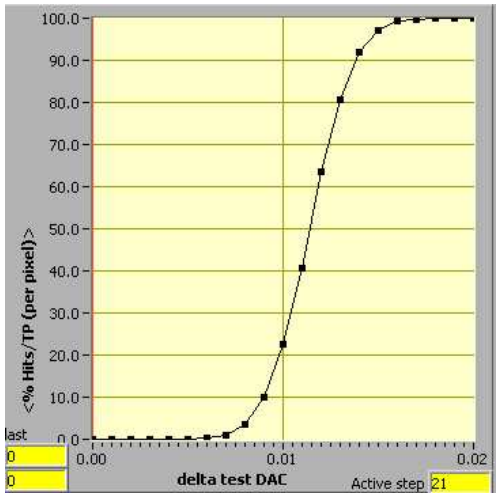

Figure 3.7: The S-curve from a Threshold Scan. The y axis shows the number of pixel hits recorded and the x axis shows the threshold setting. The result shown is the average across all 8192 pixels of a chip.

verify that the chip is operating as expected. There is also the opportunity to change the standard range of the more detailed scan if necessary.

ii. A fine scan of Pre_VTH. No test-pulse injection is used so only electronic noise should be detected. The Pre_VTH is scanned across a range of values one step at a time, and the resulting number of hits recorded. Based on this scan a Pre_VTH setting is found which places the threshold just above the level of background noise, minimising noise but maximising the amount of signal allowed to pass. Once the optimum setting for Pre_VTH has been found has been it is set to this value for the remainder of the tests.

iii. A quick scan with coarse variation of test-pulse size, at the optimum Pre_VTH. The last part of the threshold scan varies the size of the injected test pulse. The operator is required to verify that hits are measured, and the range of values used for the fine test-pulse scan can be adjusted if necessary.

iv. A fine scan of test-pulse size, at the optimum Pre_VTH. The hit rate at each value of test-pulse is recorded individually for each pixel. A fit to the recorded response determines the most effective threshold setting for each pixel.

In idealised conditions a vertical step from 0% to 100% would be seen when the test pulse size passes the threshold, but because of noise a characteristic “S-curve” is obtained, seen clearly in Fig. 3.7. This shows the response averaged over all pixels,

allowing the 50% point and slope to be found. Similar S-curves are recorded for each individual pixel on the chip. This information can be used to make fine adjustments to the threshold setting in each pixel. The position of any noisy pixels, which always respond even without the test pulse, and dead pixels, which never respond, is also recorded.

3.3.4 HPD operation at high voltage

Once the operation of the pixel chip has been established the voltage is ramped up to test the working of the full HPD. Generally, little HPD output except noise is visible below ∼5 kV. Tests are performed to measure the vacuum quality of the tube (ion feedback) and the characteristics of the anode. The behaviour of the HPD under illumination with LED light and in darkness is qualified.

- High Voltage (HV) Ramp-Up

  In order to power the HPD cathode, zoom and focus electrodes, the HV is ramped up to the standard working voltage of 20 kV. Voltage ramp-up occurs in steps and after each ramping step the response to light is tested using the LED source. Once the HV has reached 20 kV a dark count rate is monitored over 30 minutes, allowing time for the HPD to settle at the nominal operating voltage.

  The HV ramp up is controlled by software and is automatically raised from 0 to -20 kV at a rate of 50 V/s. The HPD output is monitored by the user in case of excessive ion feedback rates, or microdischarges. If a microdischarge occurs or if light levels rise due to a light leak, the bias current will be seen to "jump". While a short microdischarge is tolerable, a persistent current could easily damage the cathode and the user must check for this.

  Fig. 3.8 shows the number of hits per event against the High Voltage in kV in response to pulsed LED light. It can be seen that the number of pixels firing rises with the applied voltage. As the HV is increased to around 5 kV the number of clusters begins to rise at a rate of around 0.03 photoelectron hits per event for every 1 kV voltage increase. At around 10 kV the number of clusters begins to flatten off until a maximum rate of 0.41 photoelectron hits per event is reached. This behaviour can be seen in both methods of measuring the number of photoelectrons,

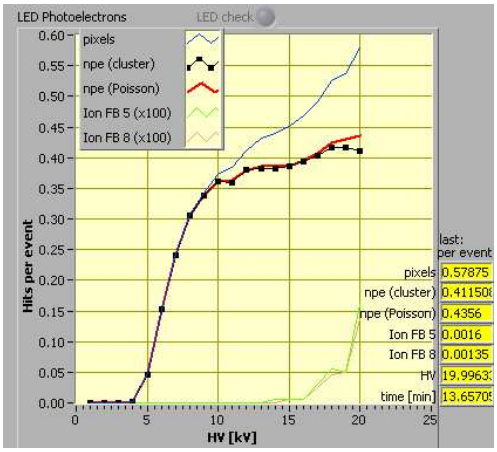

Figure 3.8: A screenshot showing the High Voltage ramp-up. Two different measures of the number of photoelectrons (npe), Poisson and from the number of clusters, are shown as red and black lines respectively. The rate of ion feedback is shown for clusters of five hits (green line) and clusters of eight photoelectron hits (yellow line). Both of these measures of ion feedback show good agreement.

and the number of clusters. Standard tests were performed with the LED light level set to yield 2-3 photoelectrons per event. The ion feedback rate does not begin to rise until around 15 kV. Ion feedback is explained in more detail below.

- Strobe Scan/Ion Feedback Scan

  After this settling period, a strobe scan is carried out to find the optimum delay of the LED light with respect to the data-taking trigger. The profile of photoelectron hits is recorded. "Strobe" refers to one of the control signals sent to the chip, which defines the sensitive time window of the pixel chip. At the test centres a strobe width of 50 ns was used to integrate over possible signal tails. The strobe width in the LHCb experiment will be 25 ns. The strobe scan is immediately followed by an ion feedback scan across a wider range of delay settings. This records the profile of clusters of hits caused by ion feedback. Ion feedback occurs when stray gas molecules in the HPD tube become ionised by incoming photoelectrons. This produces ions which are accelerated by the electric field and drift back towards the photocathode. When they hit the photocathode this releases a shower of photoelectrons which are accelerated and hit the anode, creating a signal in several adjacent pixels. These hits can easily be identified using a cluster-finding algorithm.

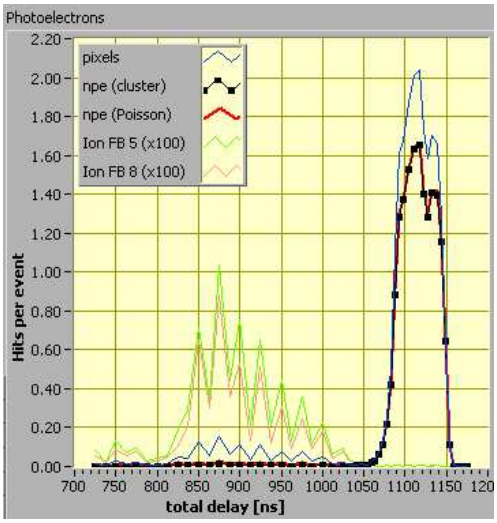

Figure 3.9: A screenshot of a Strobe Scan. The time axis is in the negative x direction. The blue line shows the number of pixels hit, while the red and black lines show two different measures of the number of photoelectrons. The green and yellow lines show the ion feedback rate, measured as clusters of five hits or eight hits respectively.

In the strobe scan the time delay of the LED with respect to the strobe signal is varied in ∼5 ns steps across a 150 ns range, and the ion feedback is recorded in the range 100-300 ns after the light pulse. A typical screenshot is shown in Fig. 3.9.

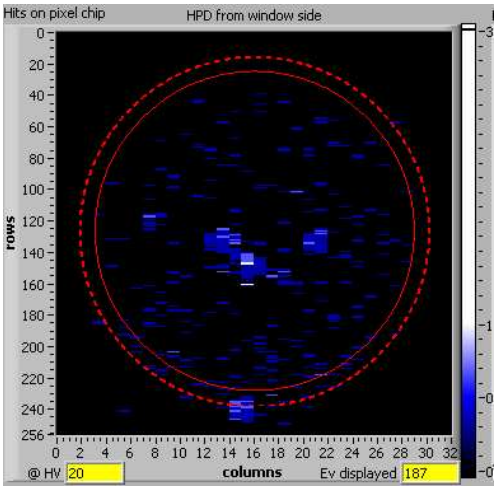

Figure 3.10: A screenshot of the ion feedback scan. This shows the image of the photocathode, with the outer edge marked as a red line. The number of hits in a given pixel are shown in a colour scale, and several clusters of hits can be seen. These "blobs" are caused by ion feedback.

The ion feedback scan varies the delay in a wider range from 0-400 ns in 25 ns steps, and measures the clusters of ion feedback hits at each time setting. The ion feedback hits will therefore be delayed in time with respect to the initial hit. This can be seen in Fig. 3.9. It can also be seen that the ion feedback signal is more than 100 times smaller than the signal from the LED light. The typical cluster of hits caused by an ion-feedback signal can be seen in Fig. 3.10. This indicates that the vacuum achieved in the tube body is excellent. The time delay of the data taking with respect to the initial LED light is varied. This enables the rate of ion feedback to be determined, and the time delay at which the ion feedback is maximum to be found.

- Bias Voltage Scan

  This scan ramps the voltage applied to the silicon anode from 0-90V, and records the photoelectron response. This determines that depletion of the anode is occurring as expected.

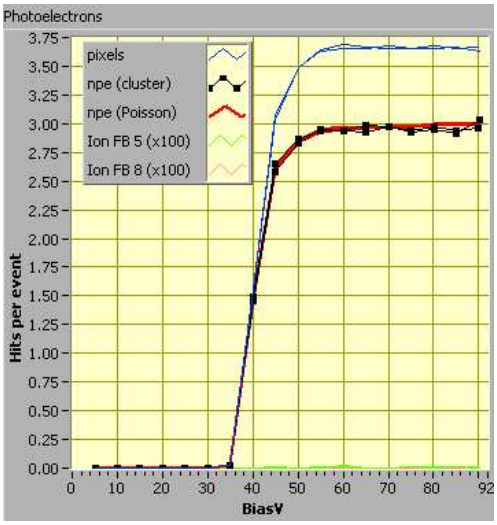

Figure 3.11: A screenshot of the bias voltage scan which ramps the voltage applied to the silicon anode from 0-90 V, then back down to 0 V. The number of hits per event is shown on the y axis, while the bias voltage (V) is shown on the x axis. The blue line corresponds to the number of pixel hits, while the red and black lines show the number of photoelectrons, as before. The green and yellow lines show the number of ion feedback clusters of five and eight hits respectively.

  The silicon anode is operated at a nominal 80 V. The bias voltage scan gradually steps this voltage from 0-90 V and then 90-0 V in 5 V steps. Fig. 3.11 shows the photoelectron hits versus the bias voltage applied to the anode. It can be seen that the number of hits rises sharply at ∼35 V, and reaches a plateau after this. Overdepletion occurs at ∼60 V. Following this test the photoelectron response to the LED light is recorded, as well as the voltages needed to achieve 50% and 90% of the maximum photoelectron response.

- High Voltage Scan

  The High Voltage Scan records the response to LED light as the HV is ramped from 0 to -20 kV, and verifies that the shape of this response is as expected. The High Voltage (HV) applied to the HPD is ramped from 0 kV to -20 kV. Fig. 3.12 shows

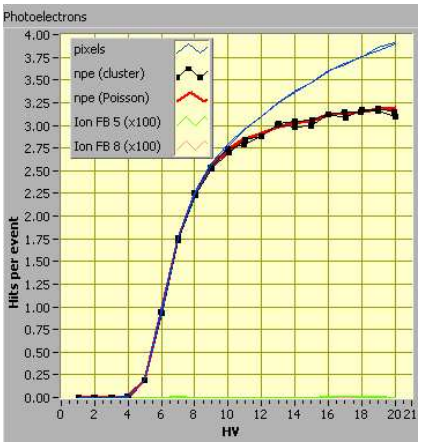

Figure 3.12: A screenshot of the High Voltage scan, which ramps the high voltage applied to the HPD from 0 kV to -20 kV. As before, the blue line shows the number of pixels hit, while the red and black lines show two different measures of the number of photoelectrons. The green and yellow lines show the ion feedback rate, measured as clusters of five hits or eight hits respectively.

the number of hits per event against the High Voltage (HV) in kV. At low voltages no photoelectron hits or clusters are visible, as expected. The number of hits and clusters starts to increase at around 5 kV, when the photoelectrons gain enough energy for signals to pass the detection threshold.

At around 10 kV the curves separate. This happens when photoelectrons gain sufficient energy to cause "charge-sharing" hits in adjacent pixels if striking the pixel boundary. This will increase the number of photoelectron hits but not affect the cluster rate. The number of cluster and Poisson hits (black and red lines respectively) rises more slowly. The increase in clusters is due to photoelectrons scattering off the anode surface which have an increasing probability of detection at higher voltages. This back-scattering rate is estimated to be ∼18%. In this example, no ion feedback clusters are visible at the delay setting. The profile of the response to LED light is recorded, and the HV at which 50 % and 90% of the maximum response is achieved.

- Long LED Run

  The Long LED Run exposes the HPD to short pulses of LED light for 200k triggers (i.e. over a period of ∼3.5 minutes). This allows the photocathode area to be

determined and any dead or unresponsive pixels to be found.

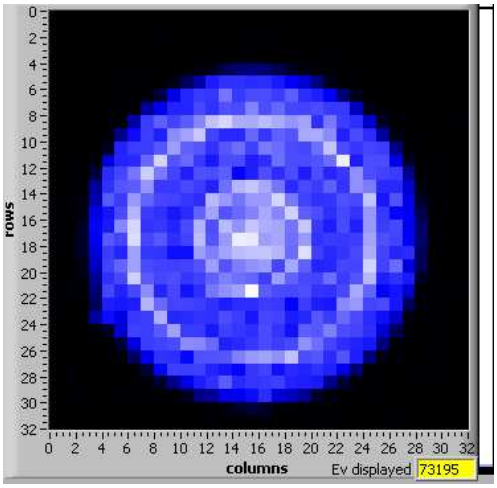

Figure 3.13: A screenshot of the Long LED Run in LHCb mode. A colour scale shows the number of hits in each pixel, recorded over the length of the run. The square LHCb pixels can be clearly seen.

This scan is also used to determine the size and position of the photocathode image on the silicon sensor (see later), and hence the demagnification and offset of the image. The Long LED run is also taken in LHCb mode. An example of this is shown in Fig. 3.13. The circular photocathode image can be clearly seen. The ring structure visible has ∼20% more hits than the surrounding areas. It is due to internal reflection from an aluminium ring near the quartz window. Events outside the active area of the photocathide are due to thermal noise or "backscatter", where a photoelectron rebounds off the pixel chip and causes a hit in a different place. Following the Long LED run, a list of dead and unresponsive pixels is logged.

- Dark Count Rate

  A Dark Count Rate measurement is carried out next. One criteria on which HPDs are categorised is their dark count, as it is important in determining their signal-to-noise performance.

  To asses the dark count rate data is taken for 5 million triggers with no LED illumination. This is carried out toward the end of the test sequence to allow the HPD time to have settled at high voltage. It has been observed that after around 2 hours HPDs exhibit a relatively settled DC. Fig. 3.14 shows a typical example, with the number of hits in each pixel displayed as a colour scale. It can be seen that

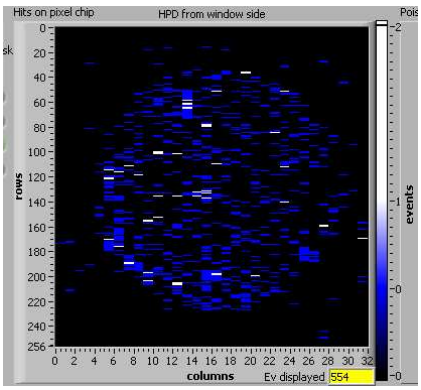

Figure 3.14: A screenshot from the Dark Count Rate measurement taken over 5 million triggers. Hits are shown in a colour scale across all pixels.

there is a low level of background hits, mainly due to thermal noise. Hits are evenly distributed across the whole HPD, with no light leaks or microdischarges apparent. The number of clusters, the cluster size and the number of photoelectrons per event are determined from the data analysis. The measurement of the dark count is then repeated in LHCb mode.

- Distortion and Demagnification

In order to test the electrostatic focusing of the HPD, a pinhole mask is positioned between the HPD and the light source. An iterative fitting procedure which maps the light passing through the holes to reference positions is used to find the distortion of the photocathode image.

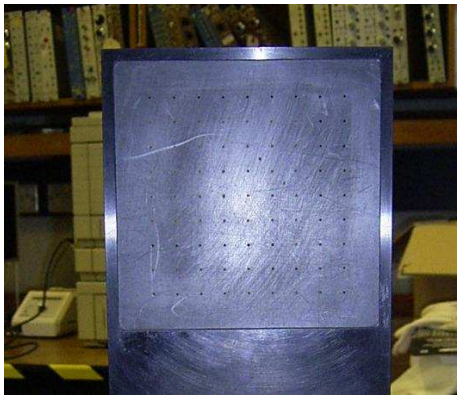

Figure 3.15: The pinhole mask, which is placed between the LED light source and the HPD.

The pinhole mask illuminates pixels in a regular array and is shown in Fig. 3.15. Mask holes are 1 mm in diameter and separated by a pitch of 11 mm. To allow easy determination of the absolute position of the mask, two additional holes are added within the grid pattern. Data is taken with 200k triggers, which takes ∼2.5 minutes. In normal operation this mask lies flat, but a small motor enables it to be raised to vertical position when required.

3.3.5 Extended HPD Tests

This sequence of standard tests described above is carried out on all HPDs. In addition to these, two further tests are carried out on a subsection of the HPDs. Adaptations have been made to one test station at Edinburgh and one at Glasgow to carry out quantum efficiency measurements and backpulse measurements respectively.

3.3.5.1 Backpulse Measurement

The Backpulse Measurement is carried out to determine the efficiency η_{Si} of the pixel chip. It is necessary to know η_{Si} accurately for correct reconstruction of the Cherenkov rings. The efficiency is defined as the probability of the readout chip registering a hit when a 20 kV photoelectron hits the silicon sensor [78], and is given by:

$$\eta_{Si} = \frac{n_{PE} < digital >}{n_{PE} < analogue >} \tag{3.1}$$

where n_{PE} refers to the number of photoelectrons. In order to monitor any fluctuations in light intensity, $n_{PE} < digital >$ is measured, followed by $n_{PE} < analogue >$, then another measurement of $n_{PE} < digital >$ is made.

A digital measurement is performed using standard data taking, with a long LED run containing 20, 000 events. The number of clusters of hits is calculated, giving $n_{PE} < digital >$. After this, the front-end electronics are switched off to reduce electronic noise, as signals such as clocking for the pixel chip will be picked up otherwise. In addition to turning off the electronics, noise reduction is also achieved by placing a grounded copper mesh over the ZIF board which acts as a Faraday cage. Noise is a significant problem in this measurement as it is affected by the capacitance across the entire sensor, not just a single pixel. For the measurement of $n_{PE} < analogue >$ the backpulse signal from a HPD is detected on the bias voltage supply line. This involves detecting the charge pulse which replenishes the charge in the anode, and integrating the pulse in a pre-amplifier. This signal is sent to an Ortec fast filter amplifier, then to a Trump multi-channel analyser card inside the data-taking PC and finally read out using the program Maestro. The LED run is repeated with triggering supplied by a pulse generator. The analogue spectrum is measured over a period of one hour ($\sim$ 10 million events). This gives a pulse-height spectrum which can be fitted to give $n_{PE} < analogue >$. Finally $n_{PE} < digital >$ is measured again, using the same method as before, which gives the LED intensity as a function of time.

3.3.5.2 Quantum Efficiency Measurement

The Quantum Efficiency (QE) is the probability of photoconversion, and is defined as the ratio of the number of photoelectrons produced to the number of photons falling on the

photocathode. In order to measure the QE it is necessary to measure the photocurrent drawn by the photocathode when exposed to a light source. This measurement enables the number of photoelectrons to be determined. In order to calculate the number of photons arriving at the photocathode it is also necessary to know the intensity of the light source.

A 50 W Quartz-Tungsten-Halogen Lamp is used as the light source. The LED light fibre is repositioned so as not to obscure the path of the light from the lamp. A pW-sensitive photodiode (Newport 818-UV) is used to measure the photocurrent. After this measurement the photodiode is removed so that the lamp illuminates a circle of 50 mm diameter at the centre of the HPD, which is slightly smaller than the sensitive area. Filters and optics are housed in an external box. An infrared (IR) blocking filter prevents the IR component of the light being detected by the HPD and biasing the results. A narrow-band filter ensures that only selected wavelengths pass through. Measurements are carried out in the range 270-800 nm at seven wavelengths (270 nm, 340 nm, 400 nm, 440 nm, 520 nm, 640 nm and 800 nm). Comparing the current drawn by the self-calibrating photodiode to the current drawn by the HPD allows the quantum efficiency to be determined. This enables a comparison to be made with the QE measured by DEP for a subsample of HPDs as a cross-check. Good agreement is seen, with the average QE at 270 nm found to be 31%. This is relatively high compared to the typical quantum efficiencies of other photodetectors. For example the Multianode photomultiplier tubes chosen as a backup option for the RICH photodetectors had a quantum effieciency of 25% at a wavelength of 360 nm [79].

3.3.6 HPD storage

Before and immediately after testing, HPDs are stored in sealed units under nitrogen flow to prevent the diffusion of helium gas through the quartz window. The status and location of HPDs are entered in a bookkeeping database, accessible from both test sites and CERN. Helium atoms in air are small enough to diffuse through the quartz window and into the evacuated tube body, so that over time performance would degrade due to ion feedback. Periodically batches of tested tubes are shipped to CERN where they are currently being installed in the RICH detectors.

3.4 HPD Test Results

3.4.1 Test Station Calibration and Results from Standard Tests

Several checks were carried out between the different test stations to ensure their calibration with respect to each other so that test results were comparable. Two of these checks are detailed below. In the first, the bias scans taken with one HPD at different test stations are compared. In the second, the characteristic IV curves of an HPD are compared.

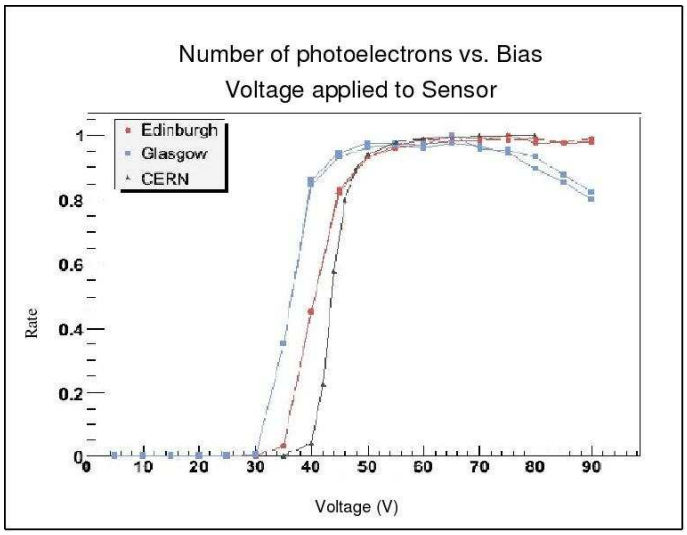

Figure 3.16: A series of bias voltage scans taken for the same HPD at different test stations. The y axis shows the rate at which photoelectron hits are measured (arbitrary scale) and the x axis shows the bias voltage applied to the silicon sensor (V). Incorrect timing means that the curves have different shapes.

Fig. 3.16 shows the number of photoelectrons detected as a function of the bias voltage applied to the silicon sensor. These curves are normalised to the maximum value for easy comparison. The shape of these curve is very sensitive to the timing in the electronic readout. This is because the bias voltage determines the velocity at which the collected charge drifts through the silicon sensor. An increased bias voltage will increase the drift velocity of the ions. It can be seen that initially the timings are incorrect, and that the curves have different shapes. The curve measured at Glasgow (blue) shows that the sensor becomes depleted at around 45 V. This depletion point changes to $\sim$ 55 V for the curve

measured at Edinburgh (red) and for the curve measured at CERN (black). The rate at which the number of photoelectrons increases with applied voltage is greater for the Edinburgh measurement than the measurement at CERN. The difference in these curves corresponds to a timing difference of $\sim$ 8 ns.

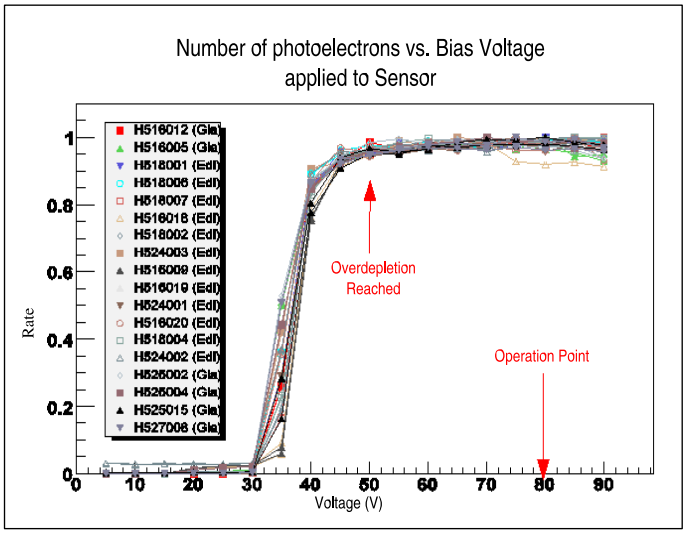

Figure 3.17: A series of bias scans taken for the same HPD at different test stations. The y axis shows the rate at which photoelectron hits are measured (arbitrary scale) and the x axis shows the bias voltage applied to the silicon sensor (V). Correct timing has been achieved, and the curves all show the same behaviour.

Fig. 3.17 shows the same measurement, with results again normalised to the maximum value. The timing of the data taking with respect to the LED light has been adjusted to within 4 ns, and it can be seen that excellent agreement is achieved between the different test sites. Full depletion now occurs at the same voltage ($\sim$ 50 V) for all three curves, and the rate of increase in the number of photoelectrons with applied voltage is the same in each case.

Fig. 3.18 shows the characteristic IV curves of one HPD measured in different test stations at Edinburgh and Glasgow. It can be seen that the current drawn when depleting the silicon sensor is dependent on the temperature of the anode, which correlates with the temperature of the readout electronics which is indicated in degrees Centigrade. At higher temperatures the leakage current increases, as expected for a semiconductor. The shapes of the curves are comparable between test stations and are independent of the anode temperatures.

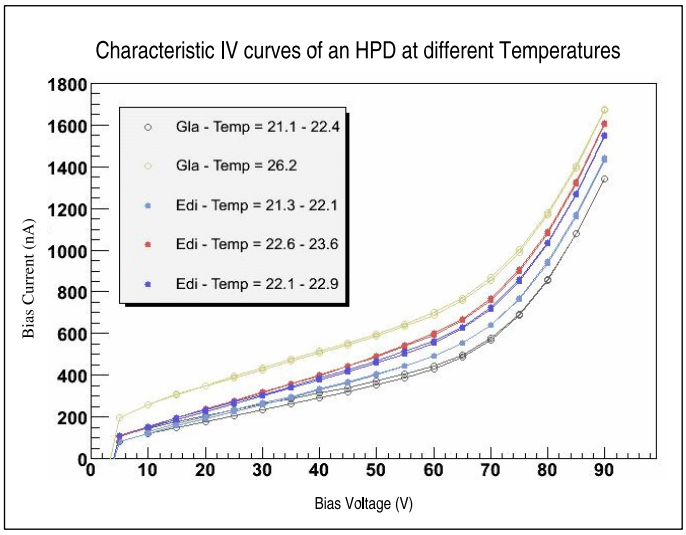

Figure 3.18: A series of IV scans for a single HPD measured at different test stations. The y axis shows the bias current (nA) and the x axis shows the bias voltage applied to the silicon sensor (V).

3.4.2 Demagnification and Photocathode Image Position using Long LED Run Data.

Limits on the mechanical placement of the anode and the precision of the electrostatic focusing may mean that the photocathode image does not fall on the nominal centre of the HPD. Offline analysis of the data from the Long LED Run uses an iterative fit approach to measure this offset.

3.4.2.1 Method

Although the photocathode image in the LED runs appears circular the fitting is done as though for an ellipse, with two degrees of freedom for the radii rather than one. This takes into account the elongated pixel shape in ALICE mode. The analysis is carried out on the accumulated data for an LED Run in ALICE mode rather than on an event-by-event basis. This clearly shows the image of the whole photocathode in good resolution. The first step of the analysis is to apply a cut at 60% of the average occupancy. This aims to remove hits which lie outside the illuminated area. The next step defines the edge of the photocathode image. If a given pixel has more than two neighbouring pixels with

no hits, it is designated as an "edge hit". This gives a rough measure of the illuminated area, but will also pick up "fake" edges surrounding dead pixels. An inital fit is made to the edge, with radii R_x and R_y. In order to minimise the effect of "fake" edge hits, edge pixels which lie inside 55% of this intial fit radius (R) are discounted, and the edge refitted. This process is repeated, removing edge pixels at incresing distances from the centre at intervals of 0.1R and refitting, until a distance of 0.95R. The fit should now give a reasonable measure of the image edge, allowing the area and centre of the image to be found. In order to refine the fit further, edge hits which lie more than 2 pixels away from the fit are removed, and then the final fit is made.

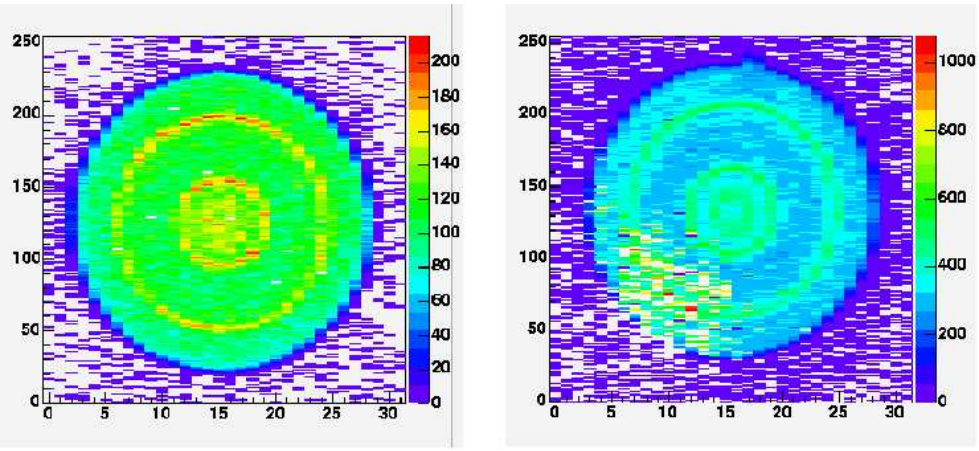

Figure 3.19: Data from two Long LED runs with the number of hits in each pixel shown as a colour scale. A typical HPD is shown on the left. An atypical HPD run is shown on the right. This HPD has many dead pixels in the illuminated area.

Fig. 3.19 shows two examples of the raw data from the LED Run, for a typical HPD (left) and an HPD with many dead pixels (right). It should be noted that the HPD on the right was the only HPD having such a high number of bad pixels, and is included to illustrate the robustness of the fit.

The iterative fitting results are shown for the HPD with many bad pixels in Fig. 3.20. The first attempt at fitting is shown on the left hand side. It can be seen that this initial fit is biased by the unusually high number of dead pixels. The final fit is shown on the right hand side of the figure. The process of discarding "edge" hits far from the initial fit has removed the contribution from the dead pixels, and the final fit closely approximates the edge of the photocathode image. The final fit can be seen superimposed on the raw LED

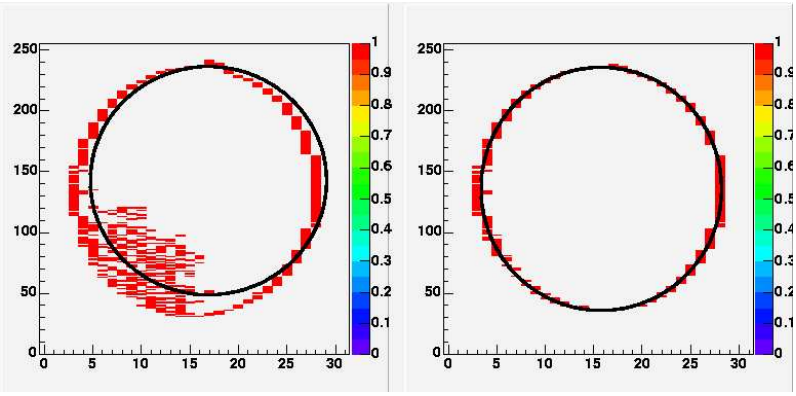

Figure 3.20: An example of the analysis of LED Run data to find the size and position of the photocathode image. The data being fitted are from the HPD with many dead pixels, shown on the right hand side. An initial attempt at edge-finding (left) and the final fit after several iterations (right). Pixels which have been designated as lying on the edge of the illuminated area are shown in red.

Run data in Fig. 3.21. Despite the high number of dead pixels a good fit is achieved.

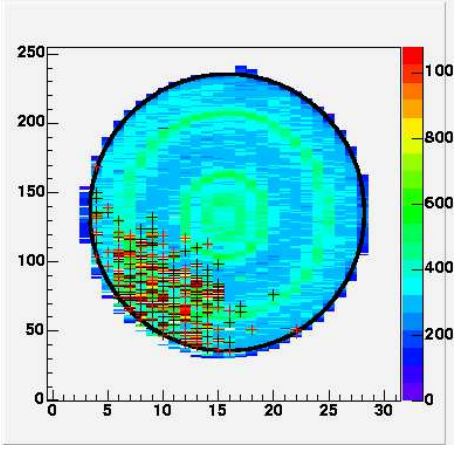

Figure 3.21: The results of the photocathode image fitting are shown superimposed on the raw data from the LED Run. The occupancy cut has been applied, removing the hits outside the illuminated image area. The fit is shown as a black ring and pixels designated as dead are marked with crosses.

In order to define poor and dead pixels the occupancy of the illuminated area must first be determined. First the active area (A) is used to define two sections, an inner ellipse with an area of 0.99A and an outer section which lies between the ellipses with area 1.10A and 0.99A. This is in order to take into account that the edge of the illuminated area is likely

to have a different occupancy to the rest of the area. The average number of hits per pixel is found for both these areas, and the number and positions of pixels which under-respond are recorded. Pixels are defined as dead if they have less than 5% of the number of hits in the surrounding area, and poor if they have less than 50% of the average. Dead pixels are marked with alternating red and black crosses in Fig. 3.21. Although this HPD showed no dead pixels when the chip was triggered with a test pulse, a total of 290 dead and 341 poor pixels were found with the LED run. This shows that the fault is not in the pixel chip iteslf, but is likely to be due to poor bump-bonding of the pixel chip to the sensor chip. This fit returns the centre position of the photocathode image, and the radii in the horizontal and vertical directions, which are stored.

3.4.2.2 Results

Data from the Long LED Runs of a subset of HPDs was analysed as described above. This subset consisted of 39 HPDs, representing 10% of the HPDs which had undergone standard tests at the time of this analysis. The HPDs with serial numbers H615018-H542002 were tested at Edinburgh, using test station 2, H527004-H650009 were tested at Glasgow station 1, and H607002-H644009 were tested at Glasgow station 2.

Fig. 3.22 shows the numbers of pixels per HPD designated as "poor" or "dead" following the criteria described above. The results obtained at different test stations show no trends between stations, as expected. It can be seen that HPDs with high numbers of dead pixels also tend to have high numbers of poor pixels. This may be due to non-optimal bump bonding across the pixel chip. An HPD is classified as category E if it has more than 2.5% bad pixels. None of the HPDs tested here fail this threshold.

Fig. 3.23 shows the vertical radius (R_Y) versus the horizontal radius (R_X) determined from LED Run data. This ratio is expected to be 8.0 due the size of ALICE pixels (500×62.5 μm^2). However, the average ratio was found to be 8.2. Lines corresponding to both of these ratios are shown on Fig. 3.23 for comparison. This result is likely to be due to charge sharing across a given pixel. When grouping pixel hits into clusters the hit is assumed to lie at the geometric centre of the pixel. However the pixels are eight times larger in the horizontal direction than in the vertical direction. Due to this the falloff in illumination levels will be greater in the vertical direction than the corresponding

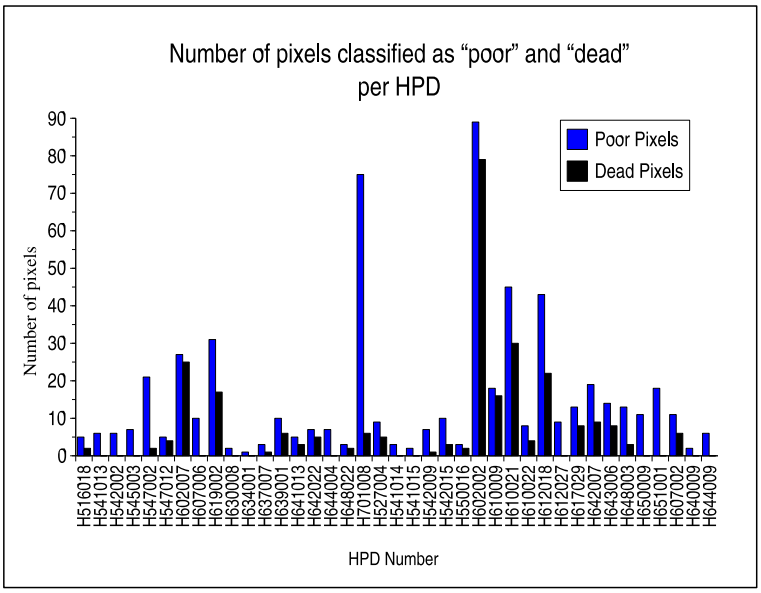

Figure 3.22: Numbers of pixels classified as poor or dead per HPD, determined using data from the Long LED Run. The number of poor/dead pixels is shown on the y axis, with the HPD number on the x axis. It can be seen that there is a correlation between the number of poor and dead pixels in a given HPD.

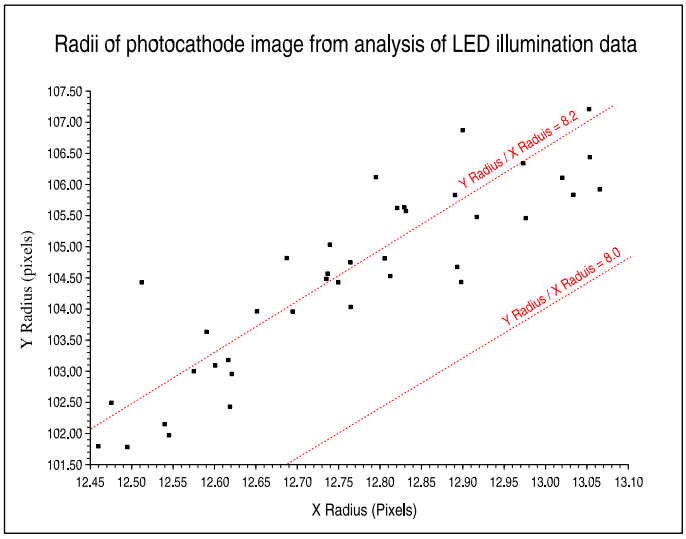

Figure 3.23: Radii of photocathode image (in ALICE pixels), determined from the Long LED Run. The x axis shows the radius in the horizontal direction, while the y axis shows the radius in the vertical direction. It should be noted that the pixels are eight times larger in the horizontal direction than in the vertical direction.

horizontal direction. This will lead to a distortion of the fit.

The average radii were found to be 12.7 pixels (6.35 mm) in the horizontal direction and 104.5 pixels (6.53 mm) in the vertical direction. Based on these radii and considering the photocathode image as a circle, the average radius was calculated to be 6.44 mm. The photocathode at the quartz window, if projected onto a plane, has a radius of 36 mm. By considering the ratio of the photocathode radius to the average photocathode image radius, the average demagnification was found to be 5.6.

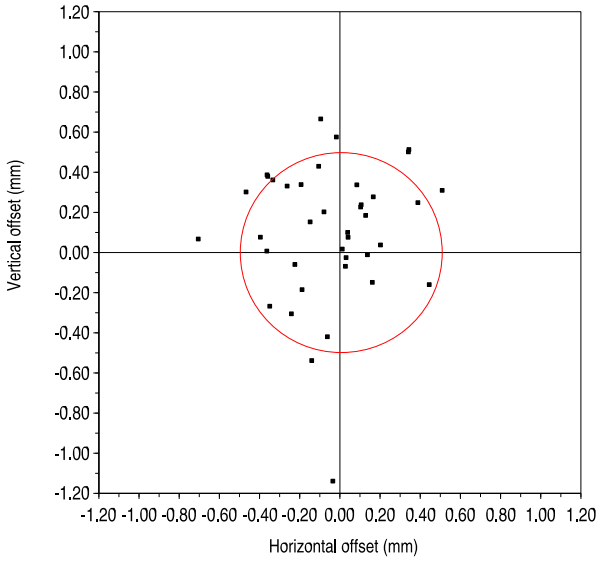

Figure 3.24: The difference in mm between geometric pixel chip centre and the centre of the photocathode image on the pixel chip. This was determined from the Long LED Run analysis. The y axis shows the vertical offset and the x axis shows the horizontal offset, both in mm.

Fig. 3.24 shows the offset in mm of the centre of the photocathode image from the nominal (geometric) centre of the pixel chip. It can be seen that the majority of points fall within ± 0.5 mm of the nominal centre (marked as red circle). This corresponds to the size of one LHCb pixel. Offsets of larger than ± 1 mm (2 LHCb pixels) will be classed as Category E and will lie outside contract specifications. Image distortions in the fringe magnetic field of the RICH may lead to signal loss with photoelectron hits falling outside the sensitive area. The offsets shown in Fig. 3.24 are not significant and will not affect the performance of the HPDs.

3.4.3 Rotation and Demagnification using Pinhole Mask Data

As discussed before, the positioning of the silicon sensor during manufacturing may mean that the nominal centre of the sensor does not lie along the axis of the HPD tube. Also, imperfections in the electrostatic focusing of an HPD may mean that the image formed on the photocathode is rotated or skewed. A method has been developed to measure any such rotation using data taken with a pinhole mask in place.

3.4.3.1 Method

An example of data taken with the mask in place is shown in Fig. 3.25. Most of these hits will be from LED light passing thorough the holes in the mask, though some may be from back-scattered electrons or ion feedback signals.

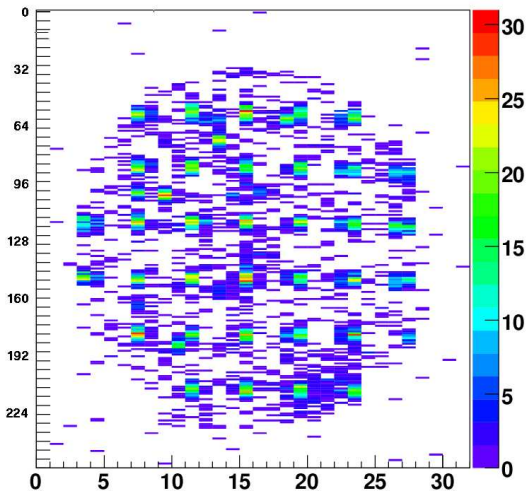

Figure 3.25: Data taken with a "pinhole" mask between the HPD and light source.

The analysis to measure any rotation of the silicon sensor is an iterative process. It involves fitting the position of the pinhole images on the photocathode to reference points with no rotation or distortion. This is carried out using data accumulated over 200k events, rather than on an event-by-event basis.

The first step of the analysis is to adjust the pinhole mask data so that it is centred on the geometric chip centre. In order to do this the offset determined from the LED Run is used. This adjustment corrects for any chip offset within the HPD tube. The pinhole

mask data are also adjusted to the average photocathode size.

The next step is to eliminate background hits outside the photocathode image. A cut is applied which removes pixels with less than 20% of the maximum occupancy. Any noisy or always on pixels must be masked before this step to prevent a distortion of this maximum. After this hits are grouped into clusters. Collections of hits on adjacent pixels are grouped into a cluster with each pixel weighted by the number of hits [80]. The Centre of Gravity (C) of the cluster is found and this is taken as the mid-point of the image from a particular mask hole.

In order to eliminate hits which do not originate from the pinhole mask certain hits are then discarded. Hits lying more than one pixel in the horizontal direction or eight pixels in the vertical direction from the nearest point C are unlikely to originate from a pinhole image. These are eliminated and the clustering step is repeated. A new Centre of Gravity (C) is found for each cluster, j. These steps result in a series of measured positions (C_j)

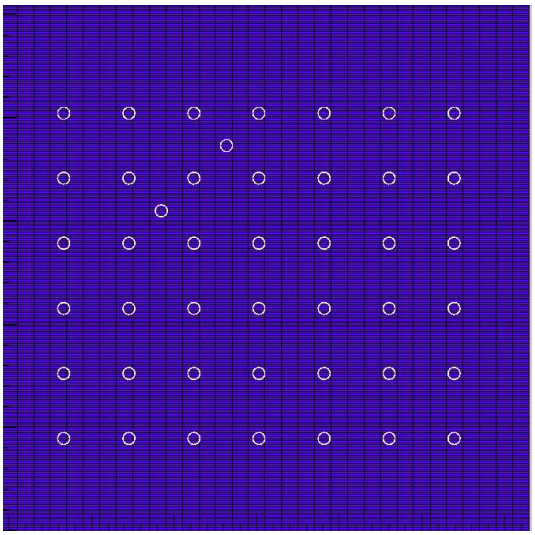

Figure 3.26: Reference points for the analysis of the pinhole mask data. These points are an approximation of an HPD with no distortion.

which are then compared to a series of reference positions. These reference points were defined by calculating the position that the images of the pinholes would lie on the HPD pixel without any distortion, and are shown in Fig. 3.26. A linear demagnification is assumed and the average demagnification from LED Run data is used. This reference grid is centred on the geometric HPD centre. A fit is carried out to map the series of

measured points onto the reference points. The distance (d_j) from each of the measured points C_j to the nearest reference point is calculated. The total distance $\sum d_j$ is found. This total distance is minimised by a TMinuit fit (a minimisation function available from ROOT [81]). The fit parameters are the demagnification, rotation and x/y displacement of the image from the geometric centre.

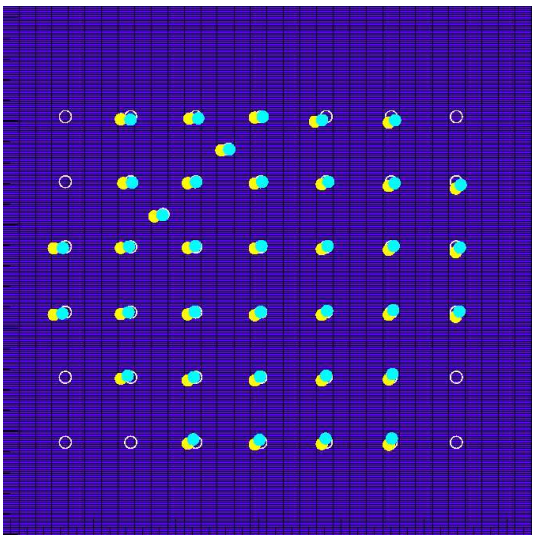

Figure 3.27: An example of data taken with the pinhole mask in position (see text for details). White open circles show the positions of the reference points. Yellow points represent data taken with the pinhole mask in place. This has been adjusted to the geometric chip centre. Cyan points are the results of a TMinuit fit to map the data points onto the reference points.

Fig. 3.27 shows the reference points in white. The clustered data points C_j are shown in yellow, after correction to the geometric centre and average demagnification. The "best fit" points after the fit has been carried out are shown in cyan.

3.4.3.2 Results

Data from the 39 HPDs considered previously were analysed as described. This allowed the rotation, x/y displacement and size of the pinhole mask image to be found.

Fig. 3.28 shows the distance from the geometric chip centre to the centre of the pinhole mask image on the photocathode. These displacements are mainly due to the mechanical

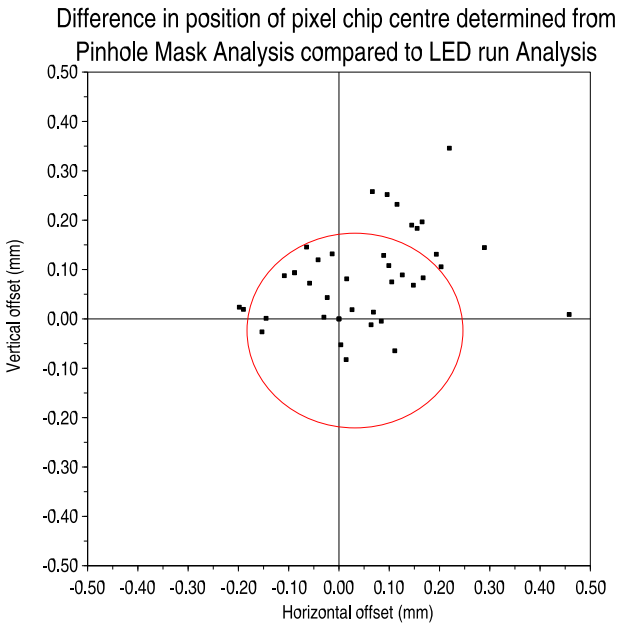

Figure 3.28: The distance of the pinhole mask image centre from the geometric chip centre. The y axis shows the vertical offset and the x axis shows the horizontal offset, both in mm. The red circle indicates an offset of ±0.2 mm and encompasses most of the points. Note that a smaller scale has been used than in Fig. 3.24.

precision of the HPD base and the dark box mounting ∼0.5 mm. No significant offsets were seen.

Fig. 3.29 shows the change in image size which best fits the data from the pinhole mask to the grid of reference points. A change of +0.01 means that the fitted image from the pinhole mask data is 1% bigger than the reference image. Similarly, a demagnification of -0.01 means that the demagnified image will be 1% smaller than refence image. The change in image size ranged from +0.01 to -0.125, with most being less than a factor of ±0.03. The majority of the differences were negative, suggesting that the reference points are biased. This is likely to be due to the simplistic linear demagnification assumed when calculating the reference positions. This does not take into account the divergence of the LED light, which will make the image larger and hence the demagnification appear smaller. Neither does it take into account ray tracing through quartz which will make the image smaller and the demagnification appear larger. A simulation would give the means to separate the two effects.

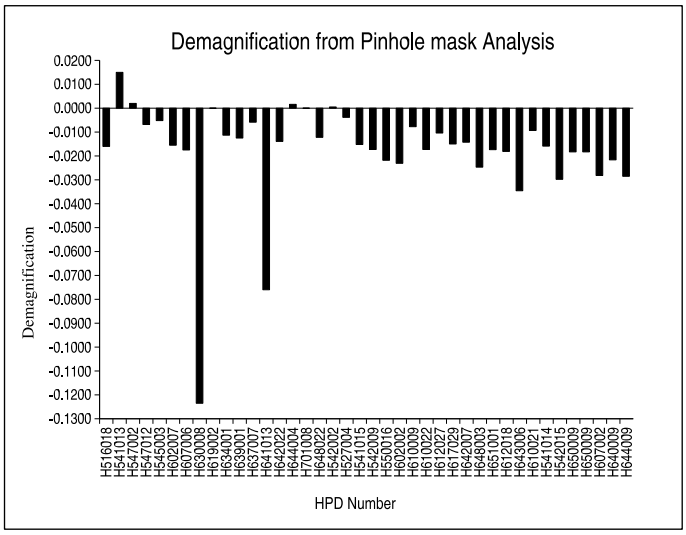

Figure 3.29: The change in image size which best fits the data from the pinhole mask to the grid of reference points. The y axis shows the change in image size and the x axis shows the HPD number. Entries which are positive on the y axis represent an increase in image size with respect to the reference points, while those which are negative represent a decrease.

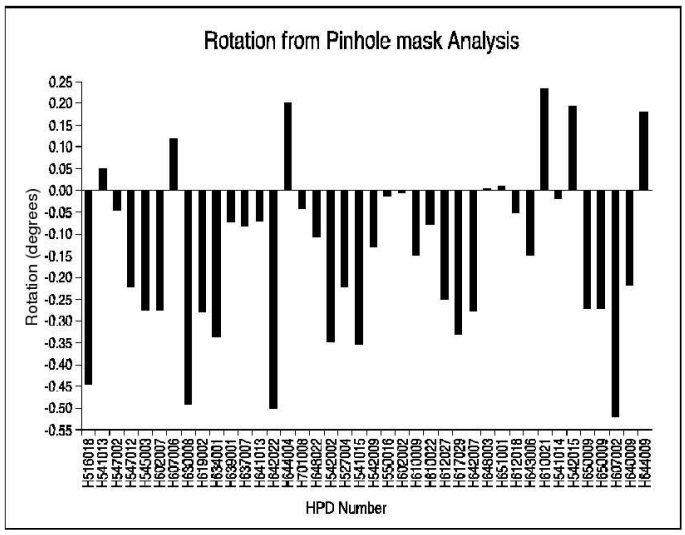

Figure 3.30: The rotation in degrees of the pinhole mask data with respect to the grid of reference points. The y axis shows the rotation in degrees and the x axis shows the HPD number. Positive rotations are clockwise while negative rotations are anticlockwise.

Fig. 3.30 shows the rotation of the pinhole mask data with respect to the grid of reference points. Positive rotations are clockwise and negative rotation are anticlockwise. There

are a higher number of anticlockwise rotations than clockwise rotations. This is likely to be due to the absolute orientation of the HPD mount and pinhole mask. Most of the rotations are between $\pm 0.25^o$, suggesting that no significant distortion is occurring in the HPD focusing. Comparing Figures 3.29 and 3.30 it can be seen that the demagnification and rotation of a particular HPD are not related.

3.5 HPD Performance in a Testbeam

A testbeam was carried out at CERN in November 2004 using six pre-production prototype HPDs and a prototype of the on-detector electronic system. A 10 GeV/c π^-/electron beam at the CERN-PS was used. In order to obtain a pion beam with low electron contamination a threshold Cherenkov counter was used.

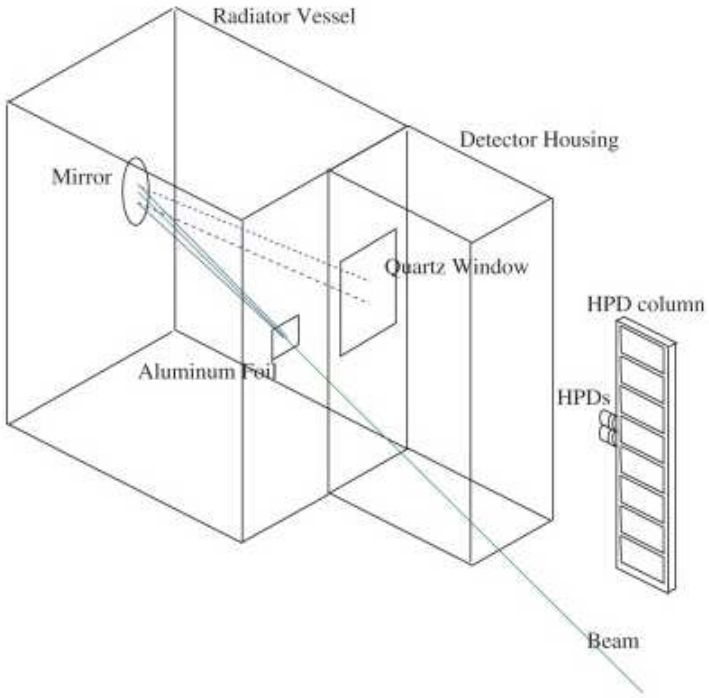

Figure 3.31: A schematic showing the arrangement of the radiator vessel and HPDs used in a testbeam. One column with two HPDs mounted upon it is shown. [82]

The HPDs were mounted in close-packed arrangement on two columns, which were placed in a light-tight box containing N_2 gas. Another section of the box contained N_2 gas which acted as a Cherenkov radiator. The two regions were separated by a 5 mm quartz window. The testbeam arrangement is shown in Fig. 3.31. Particles entered the radiator vessel through an aluminium foil window. The resulting Cherenkov light was reflected from a parabolic mirror tilted at 13.4° from the beam axis. This light then passed through the quartz window into the detector housing where it was imaged by the HPDs. HPD data taken with LED illumination is shown in Fig. 3.32.

A series of conditions were defined to select interesting events. These are described

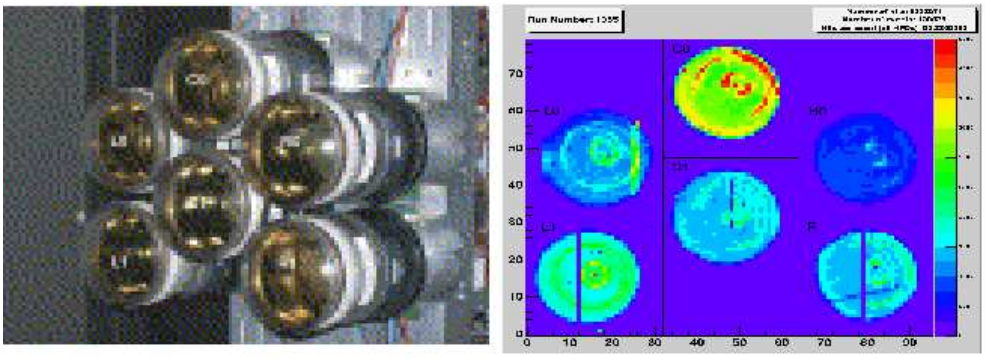

Figure 3.32: The arrangement of prototype HPDs tested in a 10 GeV pion testbeam is shown on the left. In this close-packed arrangement the active area is ∼70%. An example of the data taken during the testbeam using an LED light is shown on the right hand side. The HPDs were labelled L0-R1 according to their position [82].

Ref. [82]. The photoelectron yields in the testbeam were measured to be ∼ 10 photoelectrons per 1.1 m of N_2 radiator. This agrees with a simulation carried out using the GEANT detector description and simulation package [83]. The full analysis of the testbeam data is available in Ref. [82]. Here, we describe a method used to remove background hits in the Cherenkov ring region, and an estimation of the charge-sharing between pixels in a run taken with LED light.

In order to define the area and position of the Cherenkov ring, 'slices" were taken horizontally and vertically across the ring. Data-taking runs where the Cherenkov light was focused on a single HPD were used. An example is shown in Fig. 3.33. The slices were fitted with Gaussian functions.

It can be seen that the data correspond to a Gaussian shape as expected. The horizontal slices have a bigger width and smaller radii than the vertical slices, due to the divergence of the beam. By averaging the results from both horizontal and vertical slices the width of the ring (3σ) and the centre of the ring were defined. Two other areas were also defined, which can be seen in Fig. 3.34. The background and centre regions were defined using data for the radius and position of the photocathode for each HPD [84].

In order to get a more accurate measurement of the number of photoelectrons from Cherenkov light it was necessary to subtract the number of "background" hits. This was found by finding the number of hits in the "background" and "centre" regions and

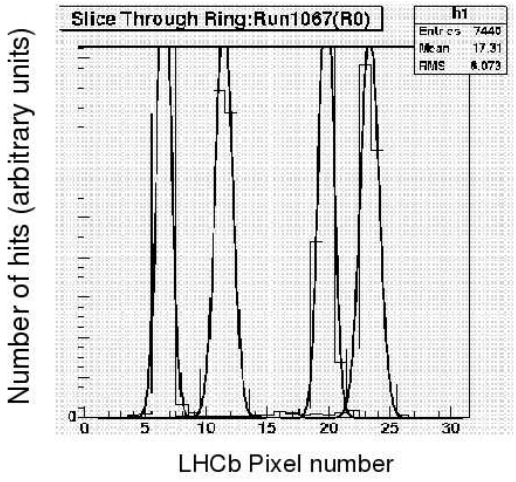

Figure 3.33: The superposition of a vertical and a horizontal slice through a Cherenkov ring. The two peaks corresponding to the horizontal slice are in the centre while the two peaks corresponding to the vertical slice are on the outside. Peaks have been fitted with Gaussian functions. The y axis shows the number of hits (arbitrary scale) and the x axis shows the LHCb pixel number.

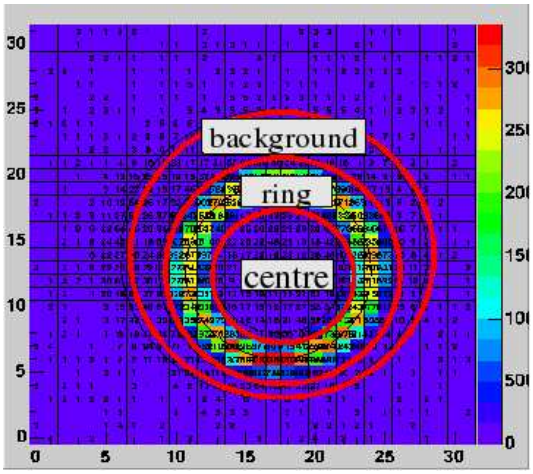

Figure 3.34: The different regions used in testbeam data analysis.

normalising for the area of each region. This enabled the average number of background hits per pixel to be found. The number of background hits in the ring region were estimated by multiplying this by the area of the ring in pixels. The background hits were subtracted from the number of hits in the ring region, and the result was normalised by dividing by the number of events. The number of photons per event in the ring region was found to range from ∼3-10 in different data-taking runs.

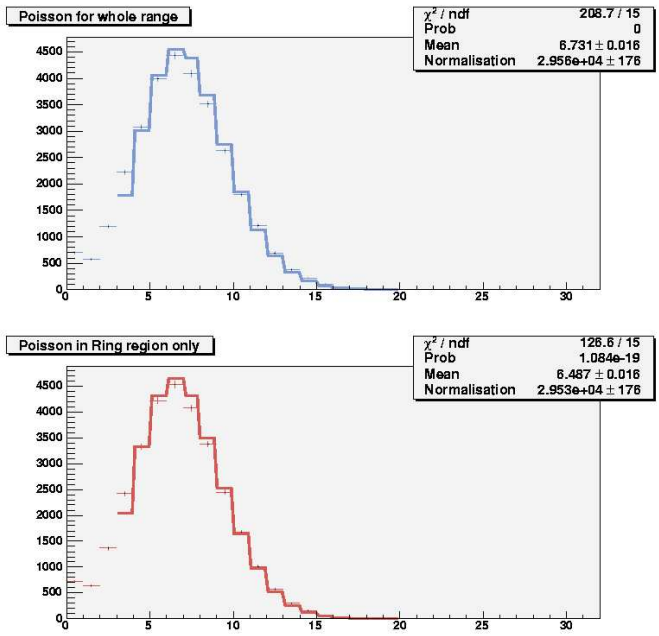

Figure 3.35: An example of Poisson functions fitted to data from the ring region. The crosses represent data points while the solid lines are the fitted Poisson function. The y axis shows the number of hits and the x axis shows the pixels hit. The top plot (in blue) shows the fit to the raw data. The bottom plot (in red) shows the fit made after background hits have been removed.

Poisson functions were fitted to data from the ring region, shown in Fig. 3.35. The top plot (in blue) shows the fit to the raw data. The bottom plot (in red) shows the fit made after background hits have been removed. It can be seen that removing the background hits in the ring region improves the χ^2 of the fit significantly. The Poisson functions do not peak at 10 , the average number of photons per track. This is due to the photoelectron detection efficiency of the HPDs (85%) and the probability that two photoelectrons hit in the same pixel and cause only one hit.

Also investigated was the number of horizontally and vertically adjacent hits, which gives a measure of the charge sharing between pixels. Data from runs where the HPD array was illuminated with LED light were used. These have a low luminosity and so a low chance of photoelectrons hitting adjacent pixels. Any adjacent hits are likely to be from charge sharing. The results from one data-taking run are summarised in Table 3.1 below. Due to variations in luminosity between HPDs the number of adjacent hits has been normalised by dividing by the total number of hits in a HPD for a data-taking run. There was a

HPD Position	Prob. of Horizontally Adjacent Hits	Prob. of Vertically Adjacent Hits
L0	0.033	0.020
L1	0.026	0.030
C0	0.048	0.052
C1	0.027	0.075
R0	0.020	0.025
R1	0.022	0.027

Table 3.1: The numbers of horizontally and vertically adjacent hits in HPDs at different positions. Data were taken with a 10 GeV/c π^- beam and an N_2 radiator. These results have been normalised by dividing them by the total number of hits in a given HPD.

known timing problem with HPDs C0 and R0, which may have affected the results for these HPDs. An unusually high number of hits in vertically adjacent pixels was observed in the HPD C1. The distribution of hits in this HPD was found to be uneven with respect to the position in rows and columns. This may be due to a readout problem in which some columns of data became "garbled".

These results were compared to charge sharing estimates made using "fake" hits. In this procedure single hits from different testbeam events were combined into a new event. This gave a measurement of probability of having adjacent hits which where not due to charge-sharing [82]. The number of hits in adjacent pixels was estimated to be in the range 2-4%.

3.6 Summary of results

The majority of HPDs studied in the pion test-beam and at the test centres showed good performance and reliability. HPDs appear to be an excellent choice for the LHCb RICH detector.

The analysis of data from the LED run shows that the HPDs have low numbers of poor and dead pixels, with all the HPDs tested having less than 1% dead pixels. The ratio of the vertical to horiozontal pixels was found to be ∼8.2, higher than the 8.0 expected from

geometrical considerations. This is due to the different rates at which light intensity falls off when moving across pixels in the vertical and horizontal directions. The offset between the geometric pixel chip centre and the centre as measured from the LED run was found to be tolerable, at less than ± 0.5 mm for the majority of HPDs tested.

The analysis of data from the pinhole mask showed that the distance of the pinhole mask image centre from the geometric chip centre was also negligible. Most offsets were found to be less than ± 0.2 mm. The demagnifications were all less than a factor of 0.13, with the majority less than a factor of 0.03. Most demagnifications were found to be negative, indicating that the fitted image was smaller than the average from the LED runs. This is likely to be due to a bias in the reference points.

The standard sequence of tests allowed categorisation of the HPDs. Tubes in Category A^+ exceed design specifications. Category A tubes meet the specifications and are fully working. Category B tubes do not fully meet specifications but are acceptable for use in the RICH detector. Category E tubes exhibit more serious issues but may still be usable as a backup option. Category F tubes clearly fail and cannot be used in the RICH detector. Categorisation was performed as follows:

- Category A+: Exceeds design specifications. An HPD with a leakage current <3 μA and a dark count of $<2\times10^{-4}$ in any given pixel. They have a Quantum Efficiency (QE) of better than 30% at a wavelengh of 270 nm. The photocathode displacement from the nominal centre is less than 1 LHCb pixel (0.5 mm). There are less than 20 faulty channels in the active area.

- Category A: A fully working tube within contract specifications. The leakage current is <5 μA and the dark count is <5 kHz per cm^2. There are <1% dead pixels (i.e. $<$ 80 ALICE pixels).

- Category B: A fully working HPD which may be out of contract specifications in some respects. The leakage current is <5 μA but the dark count rate may be between 5 kHz/cm^2 and <20 kHz/cm^2. The number of dead pixels may be between 1% and 2.5% (i.e. 80-200 ALICE pixels).

- Category E: A working tube with some test results lying out of contract specifications. The HPD could be used if required and will be kept as a spare. The HPD may

have a leakage current between 5 μA and 20 μA or the anode may exhibit resistive behaviour at bias voltages as low as 50 V. There may be more than 2.5% bad pixels.

- Category F: HPD failed testing and is not to be used. The HPD may have a leakage current of >20 μA , a break down voltage of <50 V , and dark counts of more than 20 kHz/cm^{2}or fail mechanically. There may be more than 5% bad pixels.

A total of 550 HPDs are needed for the RICH detectors, including 66 (14%) spares. HPD manufacture is now complete, with a total of 563 HPDs deliverd by the manufactuer DEP. This includes nine HPDs which failed and were replaced by the manufacturer, and four other HPDs which initally failed but were repaired. Of the 557 tubes tested in Scotland over 97% were fully working. More than three quarters meet or exceed the design specifications (catagory A+/A). The catagorisation was as follows:

- A+: 161 HPDs.
- A: 281 HPDs.
- B: 61 HPDs.
- E: 42 HPDs.
- F: 12 HPDs (including 9 HPDs which were replaced by the manufacturer).

Commissioning of the RICH detector is underway, and the HPDs are poised to play an essential part in the LHCb experiment.

Chapter 4

Analysis of the Rare Decay $B_s^o \to \phi\phi$

This chapter describes the analysis of the rare decay $B_s^o \to \phi\phi$ using Monte Carlo data. We concentrate on the possibility of measuring the weak mixing phase ϕ_s using this decay at the LHCb experiment, and the expected sensitivity of LHCb to this parameter. The related decay $B_s^o \to J/\psi\phi$ is discussed first. This provides a means of measuring ϕ_s at tree-level which can be compared to the measurement from the $B_s^o \to \phi\phi$ decay.

4.1 The $B_s^o \to J/\psi\phi$ decay

The $B_s^o \to J/\psi\phi$ decay is a $b \to c\bar{c}s$ transition which occurs at tree level in the Standard Model and is shown in Fig. 4.1. This decay has negligible direct CP violation in the Standard Model [85] and allows measurement of the weak mixing angle ϕ_s. This phase is due to interference between the decay and the $B_s^o - \overline{B}_s^o$ oscillations, where the B_s^o transforms into its antiparticle before decaying.

The decay $B_s^o \to J\psi/\phi$ is reconstructed with the final states $J/\psi \to \mu^+\mu^-$ and $\phi \to K^+K^-$ [40]. Because this is a B→VV (B-meson to vector-vector) decay, an angular analysis is required to separate out the CP eigenstates. This is described in more detail below for the similar decay $B_s^o \to \phi\phi$.

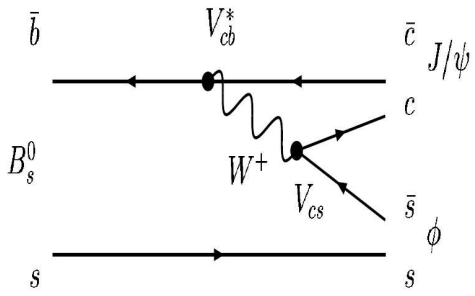

Figure 4.1: The $B_s^o \to J/\psi\phi$ decay occurs at tree level and has a b→c quark transition [40].

As this decay occurs only at tree level, it is expected to be insensitive to New Physics effects occurring in loops. New Physics effects are predicted to be small at tree-level in the Standard Model [85]. A measurement of the time-dependent decay rate allows the Standard Model values for the weak mixing phase ϕ_s to be determined:

$$\phi_S^{SM}(B_S \to J/\psi\phi) = arg(V_{ts}V_{tb}^*) \sim -2\chi = -2\eta\lambda^2 \tag{4.1}$$

where V_{ts} and V_{tb} are CKM matrix elements, η and λ are variables used in the Wolfenstein parametrisation of the CKM matrix, and χ is the (convention-dependent) phase of the matrix element V_{ts} (see Chapter 1).

4.2 The $B_s^o \to \phi\phi$ Decay

As discussed in Chapter 1 Flavour Changing Neutral Currents (FCNC) are forbidden at tree level in the Standard Model, and occur only in loops. This means that such decays are particularly sensitive to New Physics effects. The $B_s^o \to \phi\phi$ decay is shown in Fig. 4.2 and is a pure $b \to s$ penguin decay, with the ϕ mesons most likely to decay to to K^+K^-. The first evidence of the $B_s^o \to \phi\phi$ decay was obtained at Fermilab in 2004 [86]. This was measured by the analysis of 180 pb^{-1} of data taken by the CDF experiment.

In the Standard Model coupling between quarks in this decay is dominated by the CKM parameter V_{ts}. This parameter is real (i.e. it has no phase) to the third order in λ but in higher orders of λ V_{ts} has a phase of χ, which is predicted to be small (≈ 0.02). This can

be seen in Fig. 1.1 of Chapter 1.

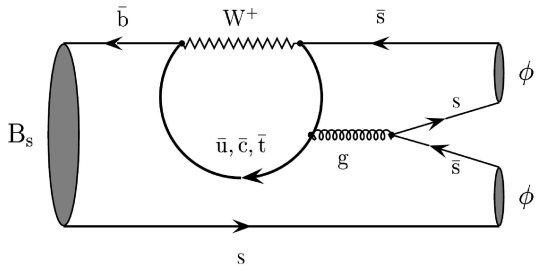

Figure 4.2: The $B_s^o \to \phi\phi$ decay is a pure penguin decay with a $b \to s$ transition [87].

For the $B_s^o \to \phi\phi$ decay, both B_s^o mesons and their antiparticles $\overline{B}_s^o$ can decay to the same final state. Because of this, it is possible for one meson to "mix" to the other before decaying, for example a B_s^o can oscillate to a $\overline{B}_s^o$. CP violation can be observed in the interference between decays with mixing and without mixing.

The physical mass eigenstates for neutral B mesons are described by:

$$|B>_{H,L} = p|B_s^o> \mp q|\overline{B_s^o}> \tag{4.2}$$

where the heavy (H) and light (L) mass eigenstates have masses $M_{H,L}$ and decay widths $\Gamma_{H,L}$. The interference between the mixing and decay is given by λ_f, defined as:

$$\lambda_f = \frac{q}{p}\frac{\overline{A}_f}{A_f} \tag{4.3}$$

Here A_f is the decay amplitude of a B meson into the CP eigenstate f, and $\overline{A}_f$ is the amplitude of its conjugate process. The amplitude ratio $|\frac{\overline{A}_f}{A_f}|$ has a phase ϕ_D, and the mixing has a phase ϕ_M, described by:

$$M_{12} = |M_{12}|e^{i\phi_M} \tag{4.4}$$

where M_{12} is an off-diagonal element of the CKM mixing matrix. The phases ϕ_M and ϕ_D cannot be measured separately. However, both phases may be measured by considering the CP violation in the interference:

$$\lambda_f^{B_s^o \to \phi\phi} = \pm e^{-i\phi_M}\frac{\overline{A}_f}{A_f} \tag{4.5}$$

It is expected that there will be no direct CP violation in the mixing or in the decay, meaning $|\frac{q}{p}|=1$ and $|\frac{\overline{A}_f}{A_f}|=1$. Because of this the mixing phase ϕ_s can be extracted by

considering the time evolution of the decays.

$$\phi_s(B_s^o \to f) = \phi_M(B_s^o \to f) - \phi_D(B_s^o \to f) \tag{4.6}$$

This allows the two separate measurements for ϕ_s from $B_s^o \to \phi\phi$ and $B_s^o \to \mathrm{J}/\psi\phi$ to be compared. If the time-dependent CP asymmetries are significantly different this will signal New Physics process in the loops. In the Standard Model, the mixing and decay phases cancel, and the net phase will be zero:

$$\begin{aligned} \phi_s^{SM} &= -arg(\eta_f \lambda_f) = -arg(\eta_f \frac{q}{p}\frac{\overline{A}_f}{A_f}) = \phi_M^{SM} - \phi_D^{SM} & (4.7) \\ &\approx 2arg(V_{ts}^* V_{tb}) - arg(V_{tb}V_{ts}^*)/(V_{tb}^* V_{ts}) = -2\chi + 2\chi = 0 & (4.8) \end{aligned}$$

where $\eta_f = \pm 1$ is an eigenvalue of the final state. A value of ϕ_s significantly different to zero will therefore signify New Physics.

4.3 Helicity Formalism

Decays such as $B_s^o \to \phi\phi$ and $B_s^o \to J/\psi\phi$ are examples of $B \to VV$ decays where the final state consists of two vector mesons. The final state of these decays is not a CP eigenstate, but is a mixture of CP-even and CP-odd components. This will "smear out" or dilute the mixing-induced CP violation. In order to measure the weak mixing phase ϕ_s these states must be separated out by an angular analysis. Angular analysis considers the total orbital angular momentum J (=L+S) which is conserved in the rest frame of the decay.

Three helicity states (H_λ) exist in the final state, H_0 where the net spin is zero, H_+ where the spin of the ϕ is parallel to the direction of motion, and H_- where is is antiparalell. Each of these helicity states corresponds to a state of well-defined Charge-Parity (CP), with:

$\lambda = 0$ (A mix of Parity-Even and -Odd states)

$\lambda = +1$ (Parity-Even)

$\lambda =$ -1 (Parity-Odd)

Allowed states of orbital angular momentum for the two meson system are:

L=0 (CP-even)

L=1 (CP-odd)

L=2 (CP-even)

where the parity P=(-1)^L. This corresponds to the S,P and D waves. L=0 and L=2 are parity-violating, while L=1 is parity conserving. Since both ϕ and J/ψ are C-odd eigenstates, their properties under parity transformation are the same as those under CP. Therefore it is possible to separate CP-even and -odd components by performing an angular analysis to separate the P-states. This analysis is usually carried out in the transversity basis. As the two ϕ mesons are symmetric, the helicity basis is chosen in order to treat the decay symmetrically [87]. Fig. 4.3 shows the $B_s^o \to \phi\phi$ in the helicity basis. The planes in which the ϕ(K^+ K^-) decays lie can be seen.

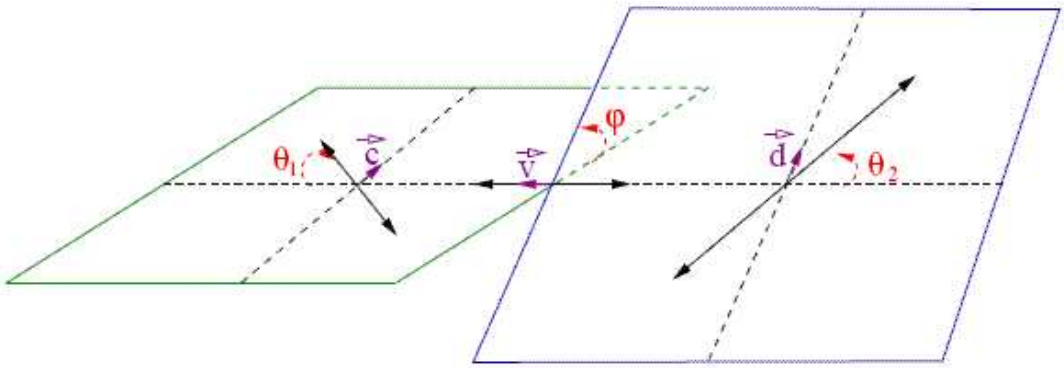

Figure 4.3: The $B_s^o \to \phi$(K^+ K^-) $\phi(K^+K^-)$ decay in the helicity frame [88].

Here θ_1 is the polar angle of the K^+ in the rest frame of ϕ_1 and θ_2 is the polar angle of the K^+ in the rest frame of ϕ_2. However, since the two ϕ mesons are indistinguishable, there are essentially only two angles to consider (φ and $\theta_1 \equiv \theta_2$). This is the polar angle of the K^+ momentum vector in the rest frame of the decay with respect to the helicity axis [89].

The helicity formalism describes the angular distribution of the decay as a function of three helicity angles. The differential decay width has three complex amplitudes which correspond to the helicity of the ϕ meson [90]. The equivalent angles in the transversity basis are given by:

$$A_0(t) = H_0(t) \tag{4.9}$$

$$A_{\parallel} = \frac{H_{+1}(t) + H_{-1}(t)}{\sqrt{2}} \tag{4.10}$$

$$A_{\perp} = \frac{H_{+1}(t) - H_{-1}(t)}{\sqrt{2}} \tag{4.11}$$

which are normalised so that $|A_0|^2 + |A_{\parallel}|^2 + |A_{\perp}|^2 = 1$. From these, the differential decay rate can be established. The time-dependent distribution allows the strong and weak phases to be measured. The distribution in the transversity basis can also be fitted to obtain the CP-even and CP-odd components.

4.4 Event Selection

4.4.1 Simulation

The $B_s^o \rightarrow \phi\phi$ decay was generated at CERN (DC04v1) using specialised programs designed to simulate the conditions at LHCb. Simulation and reconstruction were carried out in three stages, as follows:

- Event generation is carried out using GAUSS, the LHCb simulation program based on GEANT4. A Monte-Carlo (MC) simulation generates $p - p$ collisions and then tracks the particles produced and their effects in the detector. Records of Monte-Carlo "truth" are also produced for each "hit" in the detector, recording whether or not it came from a generated particle [91].

- BOOLE simulates the response of the LHCb detector to the physics events produced by GAUSS. Hits may also be added to mimic spillover events and background. BOOLE produces digitised data in the same format as that foreseen for real data and includes a simulation of the detector response, L0 trigger hardware and readout electronics [92].

- BRUNEL performs reconstruction based on the digitised hits produced by BOOLE. It is intended that it will be used for real data once the detector starts running [93]. BRUNEL outputs "Proto Particles" which have no definite identity associated with them but have values such as momentum, charge etc. The mass values are assigned during off-line analysis based on particle identification criteria such as log-likelihoods.

An analysis was performed in order to define cuts which would select $B_s^o \rightarrow \phi\phi$ decays while minimising the $b\overline{b}$-inclusive background. The first step in the analysis was to reconstruct the decay, starting with the kaon candidates. A series of requirements was employed in order to define the full decay chain. Once the decay chain had been reconstructed the data were subjected to a series of cuts to remove $b\overline{b}-$inclusive background events. After this, further optimisation of the cut values was carried out. A final estimate of the annual yield and background to signal ratio was obtained.

4.4.2 Event Reconstruction

A reconstruction was carried out with Monte Carlo (MC) data. This simulates the offline reconstruction which will be performed at LHCb. The steps of the reconstruction are as follows:

Proto Particles from the BRUNEL analysis are used to form Particles. A DaVinci Particle Maker assigns a particle identification (PID) to tracks from the detector. Long tracks traverse the full detector and hence give an accurate momentum measurement. They are assigned a kaon hypothesis if they have a difference in log likelihood (DLL) for the kaon and pion hypotheses greater than -2. It is also required that particle identification information from the RICH detector is present.

An unconstrained vertex fit is used to create ϕ candidates from the kaons. Because the number of four-prong tracks will be large, preselection cuts were used to reduce the tracks to a manageable level. Following this another vertex fit selects B_S candidates. The cuts used were defined as follows:

- The RICH detector was required to identify kaon candidates with a DLL value of larger than -2.
- The kaon tracks used to form ϕ candidates were required to have an impact parameter significance greater than 2 with respect to the primary vertex.
- The χ^2 of the vertices forming a ϕ candidate must be less than 100.
- The ϕ candidates were required to have a mass less than 1050 MeV/c^2.
- The B_s^o candidates were required to have an invariant mass between 4 GeV/c^2 and 7 GeV/c^2
- The χ^2 of the B_s^o vertices must be less than 36.

4.4.3 Preselection of Events

The DaVinci analysis was performed as described above. A total of 59,000 signal events were processed. From these, a total of 684,416 $K^{\pm}$ candidates 176,294 ϕ candidates were selected. A full reconstruction of the decay chain yielded 3535 MC-true B_s^o candidates. This corresponded to 2,412,241 seconds of data taking at standard luminosity. Not all K candidates were used to form ϕ meson candidates, and not all ϕ candidates were used to form a B_s^o.

For the $b\overline{b}-$inclusive background data, 881,882 stripped events were processed. Stripped events are $b\overline{b}-$ inclusive events which are flagged as having passed a series of loose cuts. Of these events a number were flagged as "preselected", having passed loose cuts which select the $B_s^o \rightarrow \phi\phi$ decay. The 881,882 stripped events correspond to ~32.4M $b\overline{b}-$ inclusive events. 9,883 of these were flagged as having passed the preselection cuts. A total of 353,677 $K^{\pm}$ candidates, 176,294 ϕ candidates and 8,513 B_s^o candidates were found. This corresponds to 780 seconds of data taking.

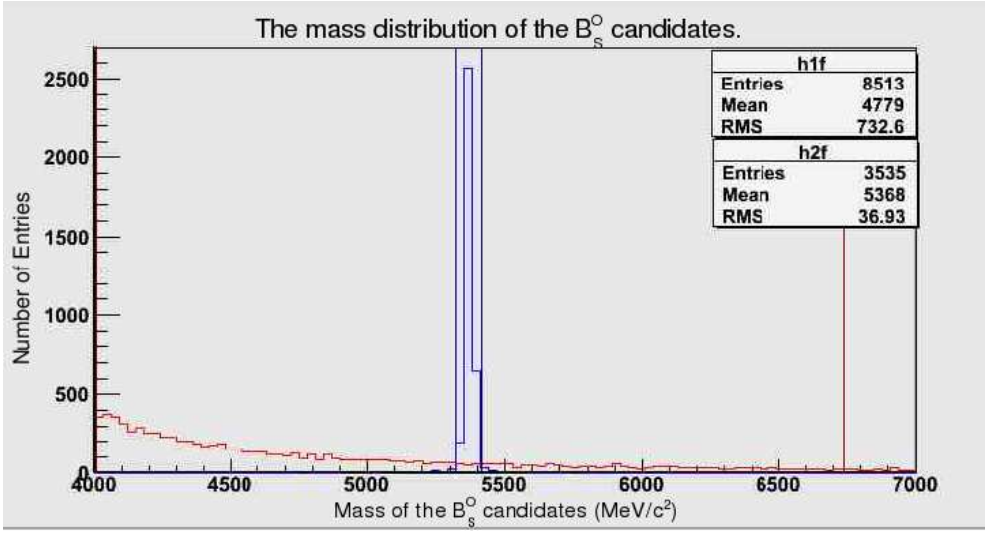

Figure 4.4: The mass distribution of the B_s^o meson candidates is shown. The blue line indicates signal data, while the red line indicates $b\overline{b}-$ inclusive events. The statistics boxes show information for the signal graph (h2f) and $b\overline{b}-$inclusive graph (h1f). The cuts applied to the signal events are shown as vertical blue lines, while the preselection cuts are shown as vertical red lines.

The distribution of the masses of B_s^o candidates is shown in Fig. 4.4. The preselection cuts

restricted the B meson mass to the range 4-7 GeV, shown. It can be seen that the signal events peak at the B_s^o mass of 5369.6±2.4 MeV [4] while the $b\overline{b}-$inclusive events form a flatter background. Mass cuts were applied to reduce the number of events. Signal data was considered in the mass window ±50 MeV around the nominal B_s^o mass. These cuts are shown as vertical blue lines. In order to have adequate statistics with $b\overline{b}-$inclusive data the mass cut applied on the background events was wider than this, at ±1370 MeV. These cuts are shown as vertical red lines. It can be seen that the background mass window is 27.4 times bigger than the signal mass window. Applying these mass cuts gave a total of 3,429 MC-true signal events, and 8,363 events from $b\overline{b}-$inclusive background.

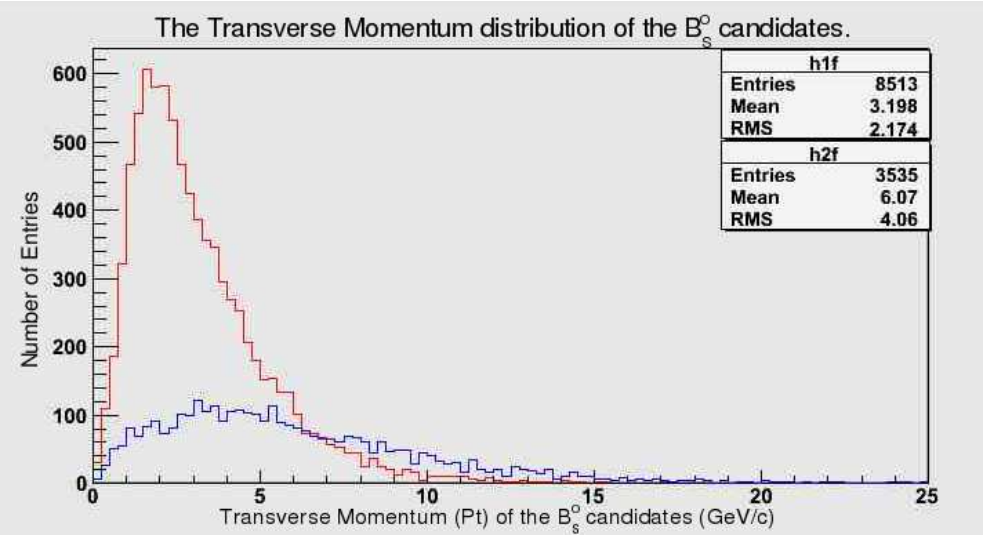

Figure 4.5: The transverse momentum distribution of the B_s^o candidates. The blue line indicates signal data, while the red line indicates $b\overline{b}-$ inclusive events. The statistics boxes show information for the signal graph (h2f) and $b\overline{b}-$inclusive graph (h1f).

Fig. 4.5 shows the transverse momentum (Pt) distribution of the B meson candidates. It can be seen that the $b\overline{b}-$inclusive events (shown in red) peak at lower value than the signal events (shown in blue). The $b\overline{b}-$inclusive events have a mean of ∼3 GeV/c, while the signal data has a mean of ∼6 GeV/c. No preselection cuts were applied to the transverse momentum, and no further cuts were made on this observable.

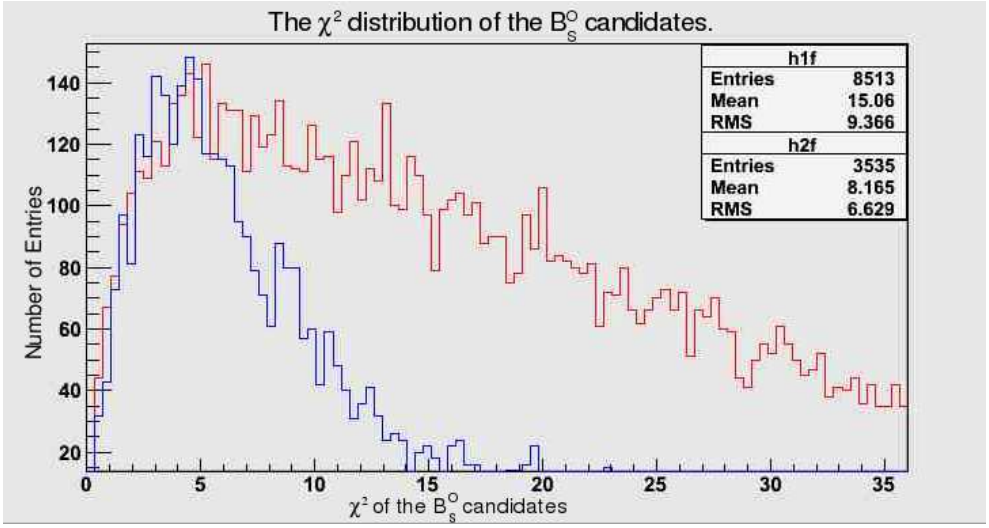

Figure 4.6: The χ^2 distribution of the B_s^o candidates. The blue line indicates signal data, while the red line indicates $b\overline{b}-$inclusive events. The statistics boxes show information for the signal graph (h2f) and $b\overline{b}-$inclusive graph (h1f).

Fig. 4.6 shows the χ^2 distribution of the B_s^o candidates. It can be seen that the χ^2 of the signal events peaks at a lower mean (8.165) than the $b\overline{b}-$inclusive events (15.06). A cut requiring the χ^2 to be less than 36 was applied in the preselection.

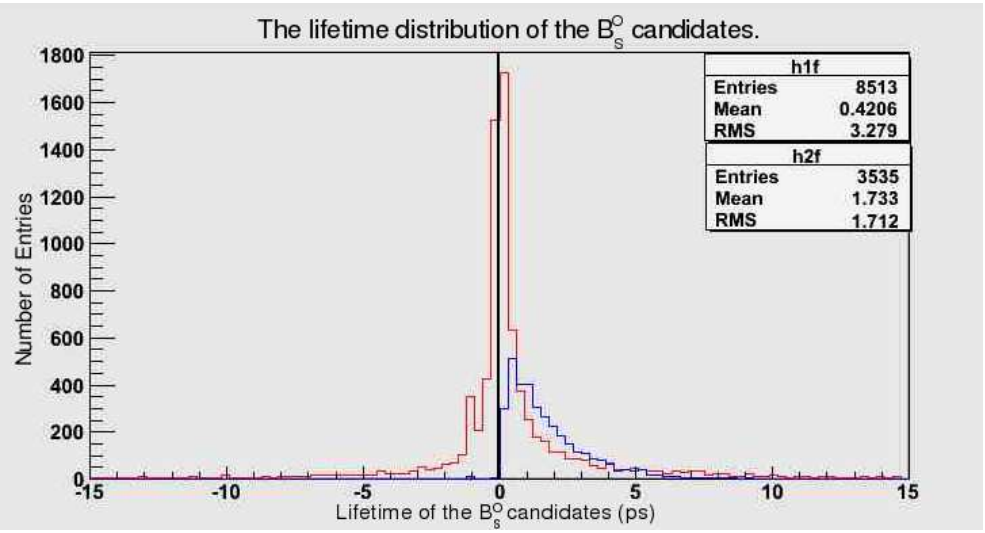

Figure 4.7: The lifetime distribution of the B_s^o candidates. The blue line indicates signal data, while the red line indicates $b\overline{b}-$inclusive events. The statistics boxes show information for the signal graph (h2f) and $b\overline{b}-$inclusive graph (h1f).

The lifetime distribution of the B_s^o candidates is shown in Fig. 4.7. All of the signal events have lifetimes greater than zero, while the $b\overline{b}-$inclusive events have lifetimes that have an approximate range of -10 ps to 10 ps, and are symmetric about zero. It can be seen that the number of signal events shows an exponential fall off as expected, with a mean of 1.73 ps. From these data a cut was defined which required the lifetime to be greater than 0 ps.

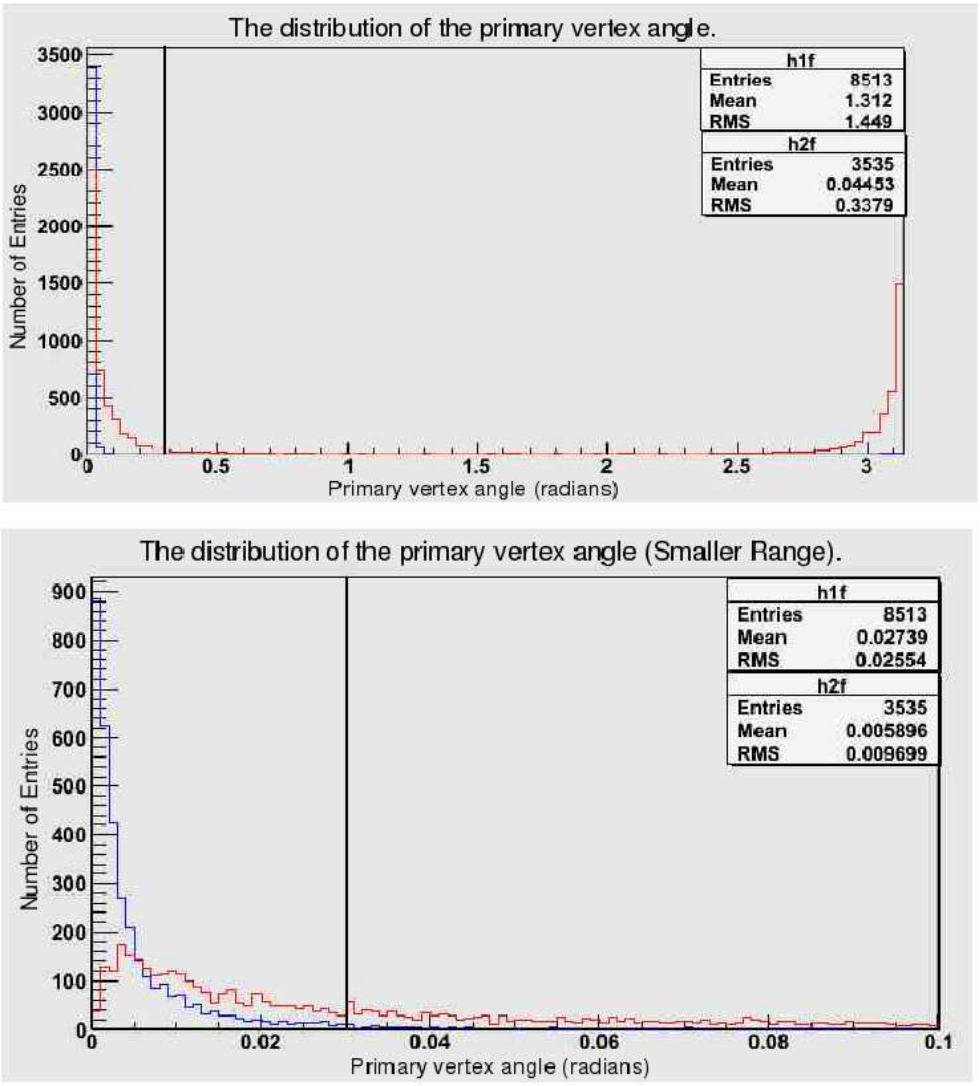

Figure 4.8: The angle between the flight path and momentum vector of a B_s^o candidate. The x axis shows the angle in mrad, while the y axis shows the number of entries. The full angular distribution is shown, up to a value of 2π. The blue line indicates signal data, while the red line indicates $b\overline{b}-$ inclusive events. The statistics boxes show information for the signal graph (h2f) and $b\overline{b}-$inclusive graph (h1f).

Fig. 4.8 shows the angle θ between the flight path of the reconstructed B candidate and the direction of its momenta. It can be seen that there are clear differences in the distribution of this angle between signal and background events. True signal events tend to have well-reconstructed momenta and direction, while MC false events may be reconstructed travelling in the opposite direction. These events form the peak at $\sim \pi$ radians which can been seen in Fig. 4.8. This figure shows that a cut applied at 0.03 radians removes most of the background while leaving the majority of signal events.

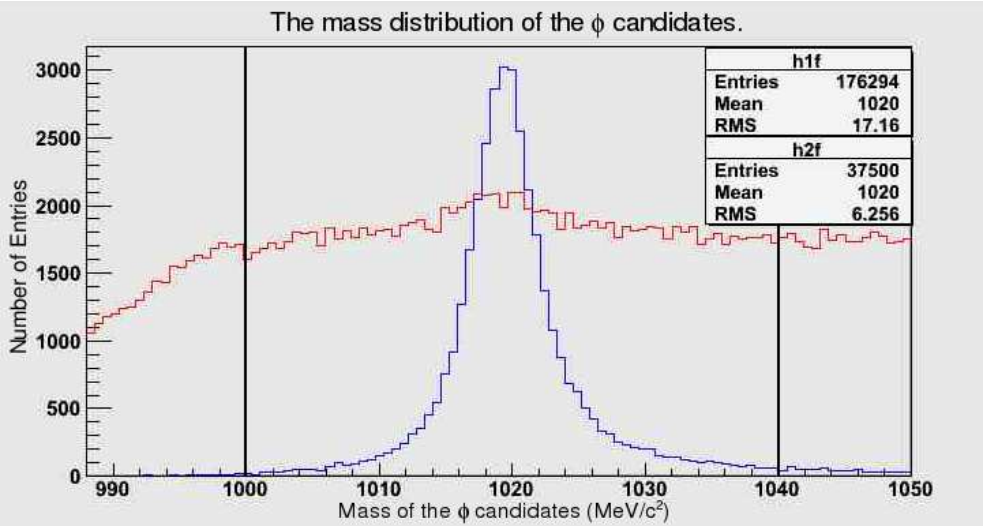

Figure 4.9: The mass distribution of the ϕ candidates. The blue line indicates signal data, while the red line indicates $b\overline{b}-$inclusive events. The statistics boxes show information for the signal graph (h2f) and $b\overline{b}-$inclusive graph (h1f). The cuts applied are shown as a vertical black line.

Fig 4.9 shows the mass distribution of the ϕ candidates. All ϕ candidates created by DaVinci are shown, not just those used to make B_s^o mesons. The preselection required the mass of the ϕ candidates to be less than 1050 MeV/c^2. It can be seen that the signal events (shown in blue) peak at the ϕ mass of 1020 GeV. The $b\overline{b}-$inclusive events (shown in red) show a much flatter distribution with a small peak. The applied cut is shown as vertical black lines. The cut chosen was a symmetric $\pm$20 MeV/c^2 around the ϕ mass.

It can be seen from Fig 4.10 that the transverse momentum (Pt) of the ϕ candidates from signal events peaks at $\sim$2.7 GeV/c. The background has a peak at $\sim$0.5 GeV/c. No cuts were applied during the preselection and the range shown was chosen to include the majority of events. The signal events have a broader distribution with a mean of

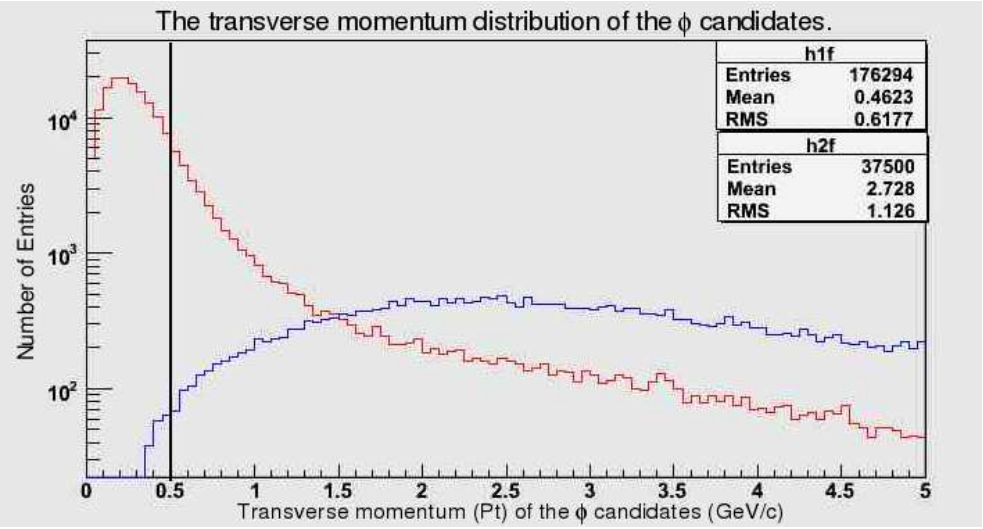

Figure 4.10: The transverse momentum distribution of the ϕ candidates. The blue line indicates signal data, while the red line indicates $b\overline{b}-$ inclusive events. Data are shown using a log scale on the y axis. The statistics boxes show information for the signal graph (h2f) and $b\overline{b}-$inclusive graph (h1f).

2.7 GeV/c. A cut requiring the Pt of the ϕ candidates to be greater than 0.5 GeV was chosen. This will remove most of the background events while leaving the majority of the signal events. This cut is shown as a vertical black line.

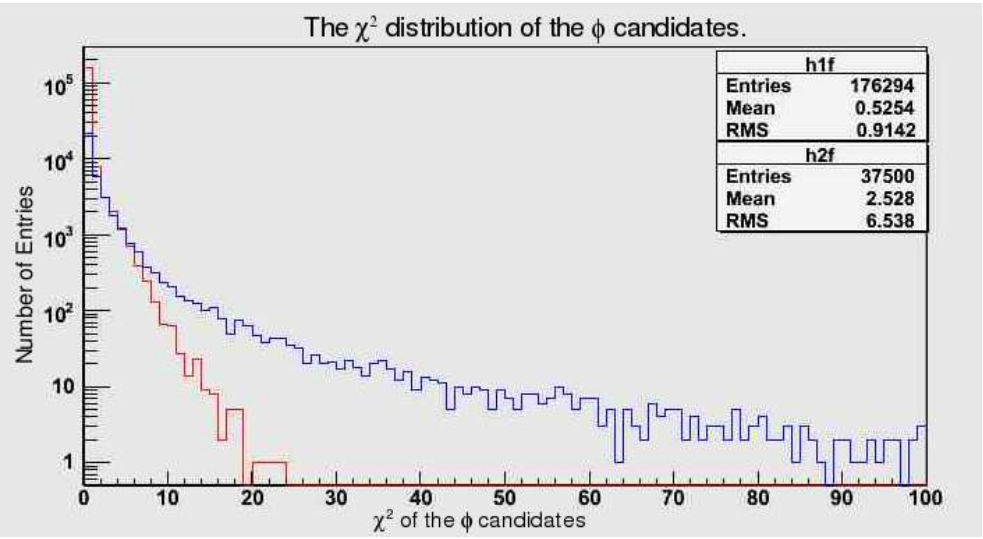

Figure 4.11: The χ^2 of the ϕ candidates. The blue line indicates signal data, while the red line indicates $b\overline{b}-$inclusive events. Data are shown using a log scale on the y axis. The statistics boxes show information for the signal graph (h2f) and $b\overline{b}-$inclusive graph (h1f).

Fig. 4.11 shows the χ^2 of the ϕ candidates. A cut requiring the χ^2 to be less than 100 was applied in the preselection. It can be seen that the signal and background events follow approximately the same distribution. Due to this distribution it was not possible to apply a further cut to reduce the number of background events without seriously affecting the number of signal events.

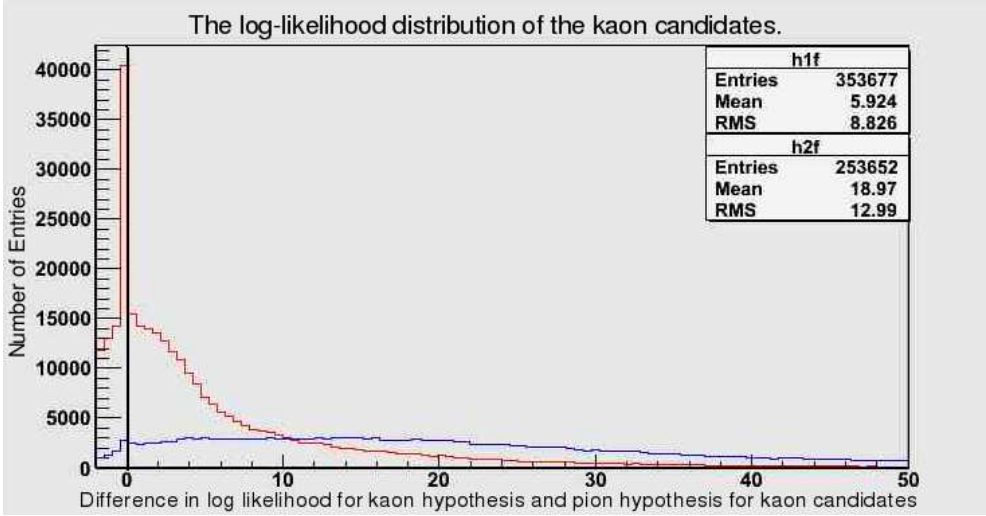

Figure 4.12: The log likelihood distribution for the kaon candidates. This shows the difference in log likelihood for a K hypothesis and π hypothesis for a given candidate. The blue line indicates signal data, while the red line indicates $b\bar{b}-$ inclusive events. The statistics boxes show information for the signal graph (h2f) and $b\bar{b}-$inclusive graph (h1f).

Fig. 4.12 shows the difference in log likelihoods (DLL) for the kaon hypothesis and the pion hypothesis. A cut at -2 was applied during the preselection. It can be seen that the majority of the signal events (shown in blue) have a DLL greater than zero. The background events (shown in red) have a DLL distribution that is approximately symmetric about zero, allowing for the cut applied at -2. Based on this distribution, a cut requiring the DLL to be greater than zero was chosen. This will remove $\sim \frac{1}{5}$ of the background events while leaving the majority of the signal events.

4.4.4 Correlations between Observables

In order to establish whether applying a cut on one observable would affect the distribution of another observable a series of correlation plots was drawn. These plotted one observable

against another so that any relationship between them could be clearly seen. Two examples are given below. Fig. 4.13 shows an example of two observables which are uncorrelated, the transverse momentum of the B_s^o candidates and the χ^2 of the ϕ candidates. This χ^2 measures the goodness of fit for the vertex of the two ϕ candidates forming a B_s^o-meson candidate. Applying cuts to either of these observables will not affect the distribution of the other observable. Fig. 4.14 is and example of two correlated observables, the B_s^o χ^2 and the ϕ χ^2. Applying cuts to a observable which shows correlation to another variable will affect the distribution of second observable as well as the variable to which the cut is applied.

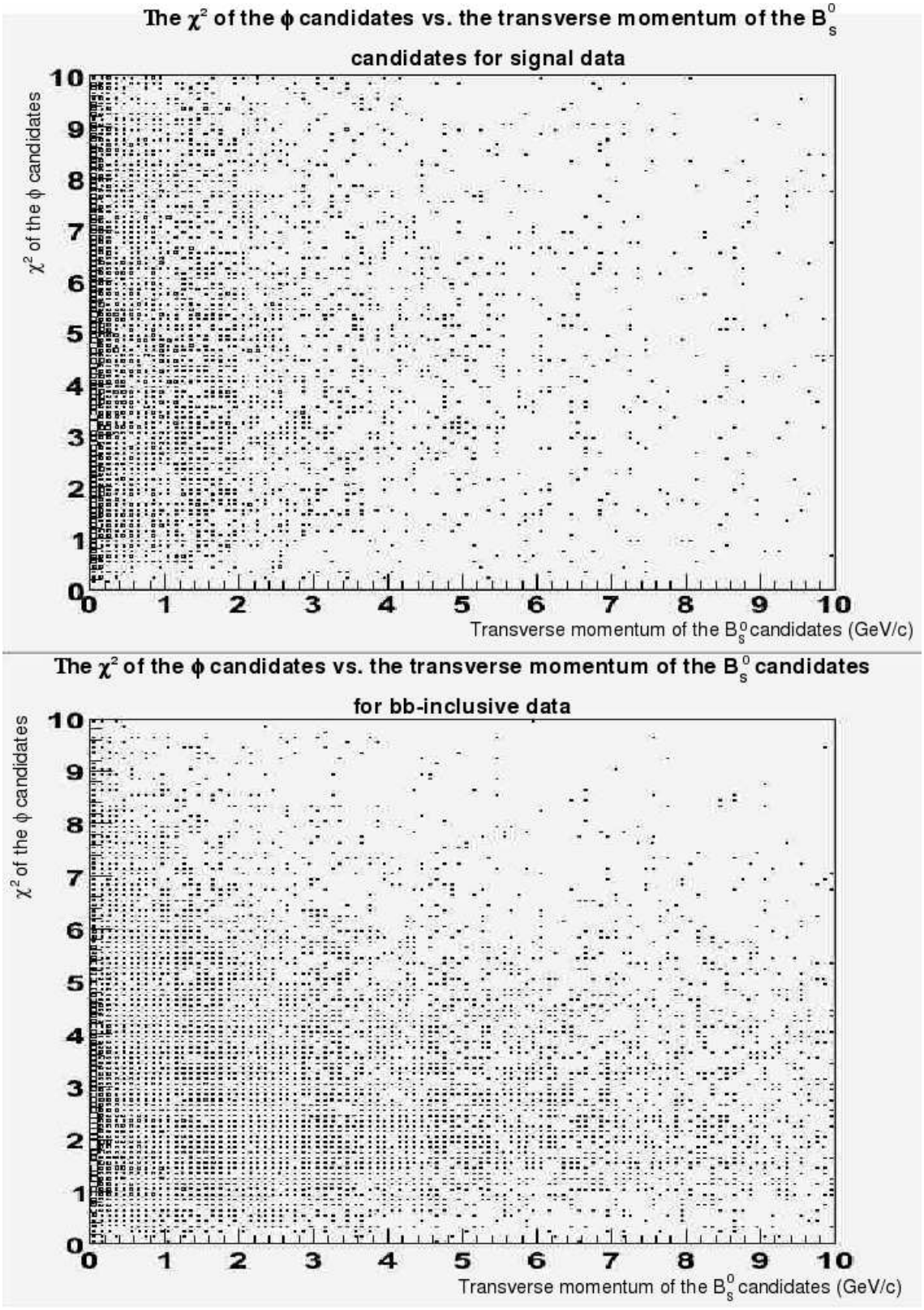

Figure 4.13: An example of two uncorrelated observables. The top graph shows $b\bar{b}-$inclusive data while the bottom graph shows MC-true signal data. It can be seen that there are no significant difference in these distributions. The χ^2 of the ϕ candidates on the y axis is plotted against the transverse momentum of the B_s^o candidates on the x axis. There is no correlation between the two observables.

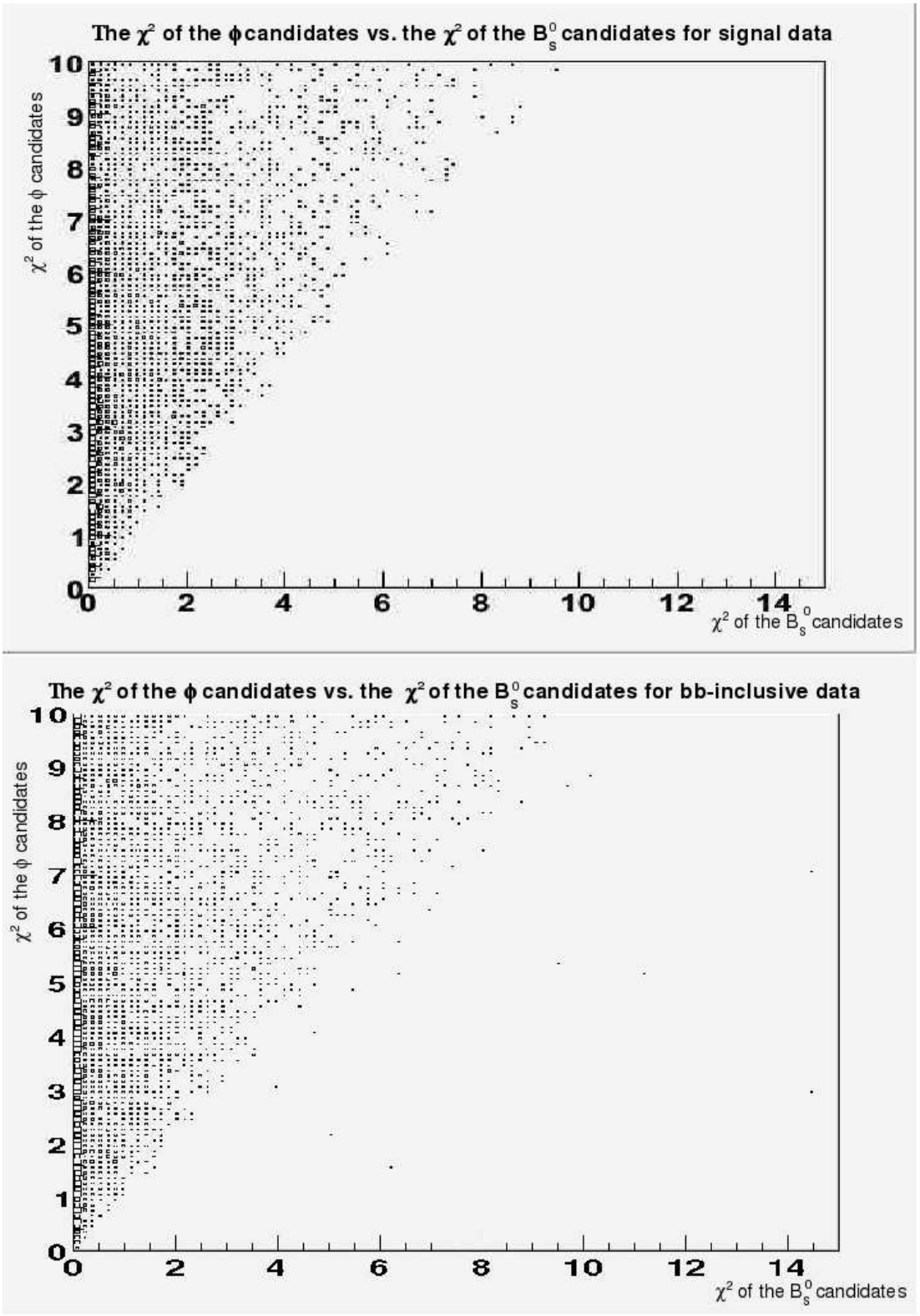

Figure 4.14: An example of two correlated observables. The top graph shows $b\overline{b}-$inclusive data while the bottom graph shows MC-true signal data. The χ^2 of the ϕ candidates is plotted on the y axis against the χ^2 of the B_s^o candidates on the x axis. There is a clear correlation between the two observables.

4.4.5 Selection Efficiencies

Based on the figures 4.4 to 4.12 a series of cuts were defined to reduce background events in the sample while leaving as many signal events as possible. A summary of these cuts is given below:

- The log-likelihood difference between the kaon hypothesis and pion hypothesis was required to be greater than zero.
- ϕ candidates were required to have a transverse momentum greater than 0.5 GeV/c.
- A 20 MeV/c^2 mass window was applied around the ϕ mass (1020 MeV/c^2) for ϕ candidates.
- The B_s^o mesons candidates were required to have a lifetime greater than 0 ps.
- The angle between the momentum vector of the B_s^o mesons candidates and their flight direction was required to be less than 30 mrad.

Applying these cuts left 2,930 MC true signal events in the $\pm$50 MeV/c^2 mass window. This represents $\sim$85% of the 3,429 signal events orignally in this window. These cuts left only 68 of the $b\overline{b}-$inclusive background events in the larger $\pm$1370 MeV/c^2 background mass window. This is less than 1% of the 8,363 events in this mass window before the cuts were applied.

4.5 Background Suppression

The signal to background ratio $\frac{S}{\sqrt{S+B}}$ was plotted as a function of applied cut for each of the observables above. Here, S is the number of MC-true signal events accepted by a given cut, while B is the number of $b\overline{b}-$inclusive events in the same range. In each case the numbers of signal and background events was normalised for time, by dividing the number of events by the respective time in seconds. Only signal events within the ± 50 MeV/c^2 mass range and background events within the ± 1370 MeV/c^2 mass range were considered.

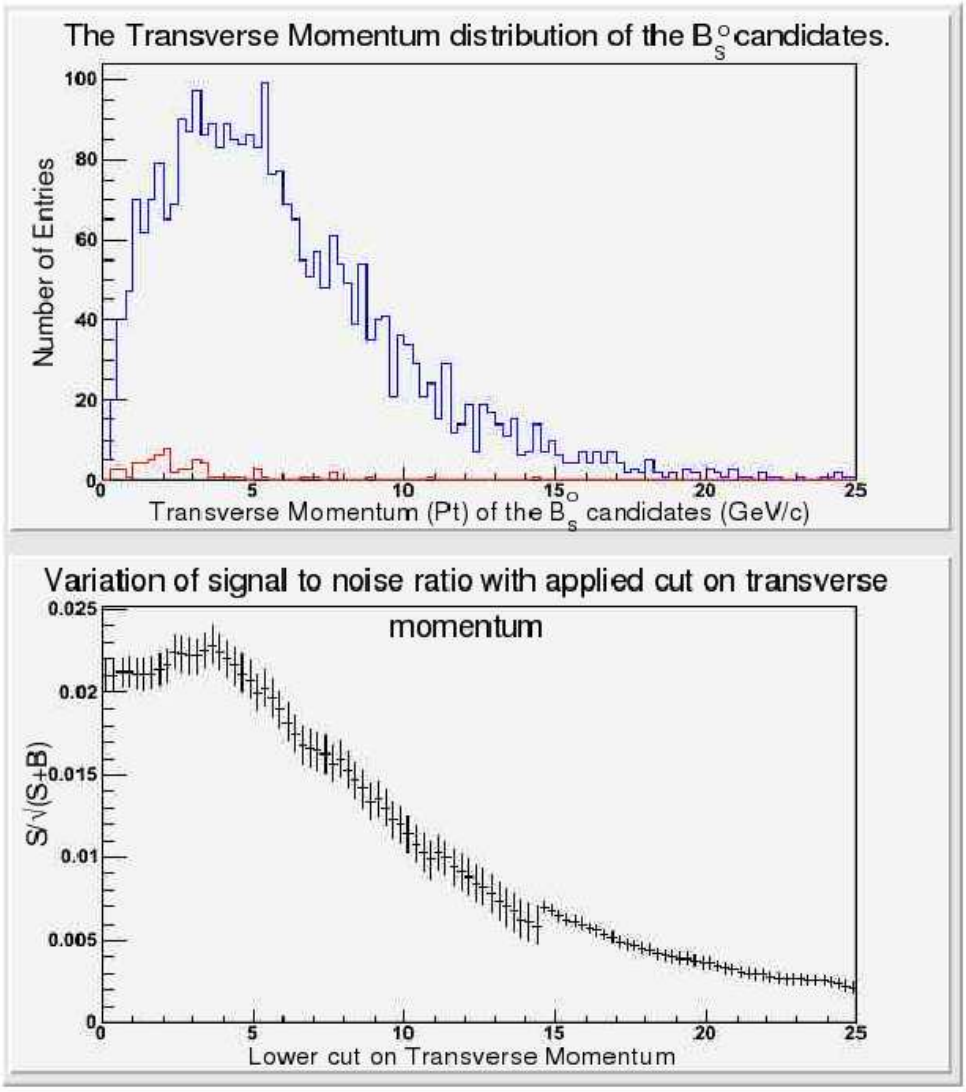

Figure 4.15: The variation of $S/\sqrt{S+B}$ with an upper cut on the transverse momentum of the B_s^o candidates. The blue line indicates signal data, while the red line indicates $b\overline{b}-$ inclusive events. The bottom section shows the variation of the signal to background ratio with the cut.

Fig. 4.15 shows the variation of the signal to noise ratio ($\frac{S}{\sqrt{S+B}}$) with an applied cut on the B_s^o transverse momentum (Pt). This is an upper cut and is varied from Pt greater than zero to Pt greater than 100 GeV/c. Little improvement in $S/\sqrt{S+B}$ is seen. No cut was applied on Pt(B_s^o).

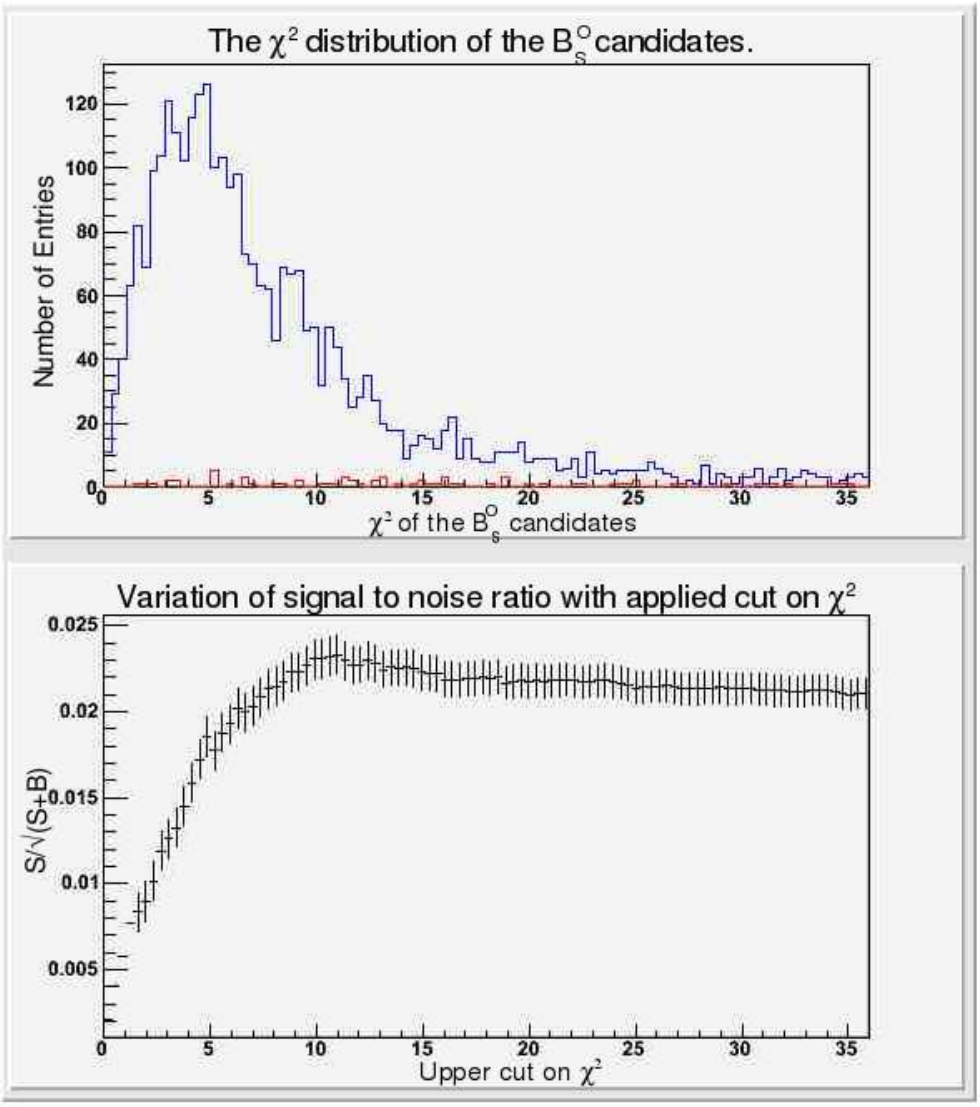

Figure 4.16: The variation of $S/\sqrt{S+B}$ with an upper cut on the χ^2 of the B_s^o candidates. The blue line indicates signal data, while the red line indicates $b\bar{b}-$ inclusive events. The bottom section shows the variation of the signal to background ratio with the upper cut.

Fig. 4.16 shows the variation of the signal to noise ratio with an applied cut on the B_s^o χ^2. This is an upper cut and is varied from χ^2 less than zero to χ^2 less than 36. A cut at χ^2 <36 was applied previously in the preselection. Little improvement in $S/\sqrt{S+B}$ is seen when applying a stricter cut.

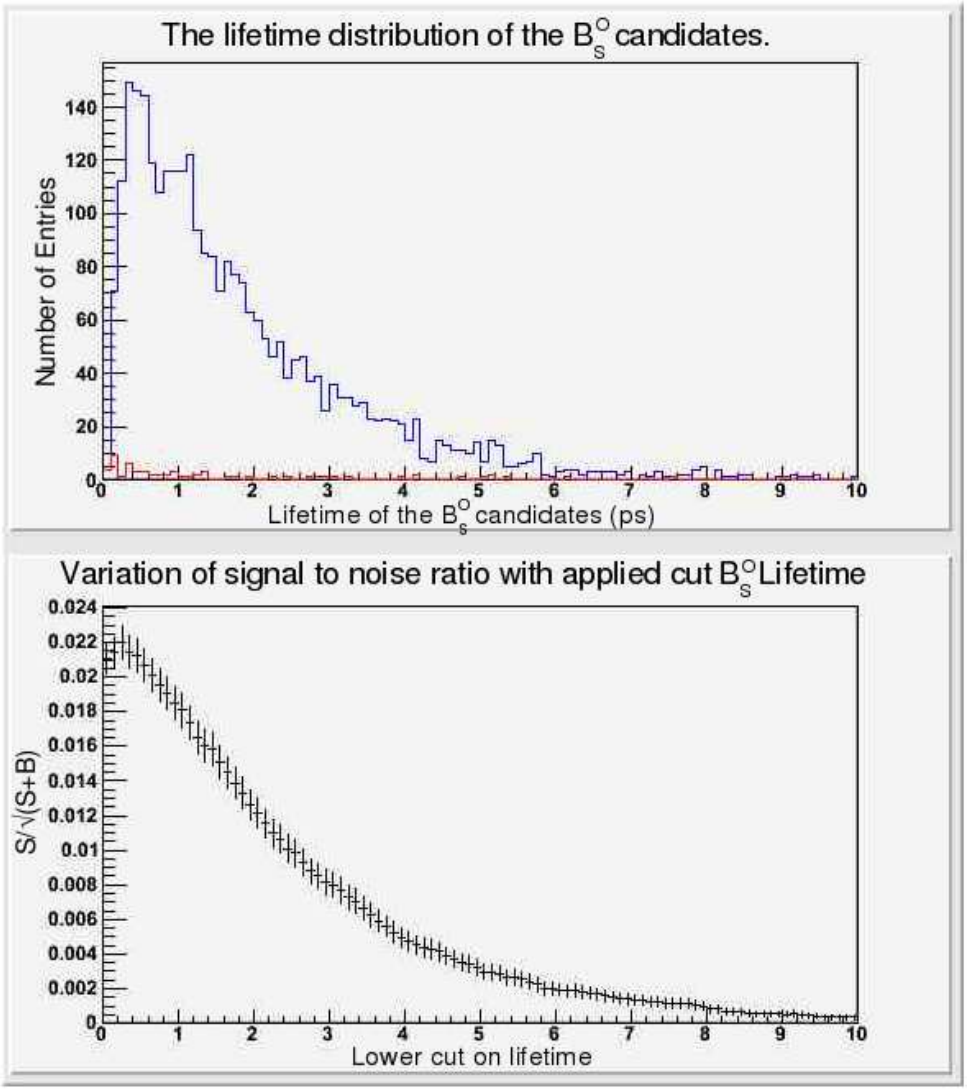

Figure 4.17: The variation of $S/\sqrt{S+B}$ with a lower cut on the lifetime of the B_s^o candidates. The blue line indicates signal data, while the red line indicates $b\bar{b}-$ inclusive events. The bottom section shows the variation of the signal to background ratio with the lower cut.

Fig. 4.17 shows the variation of the signal to noise ratio with an applied cut on the lifetime of the B_s^o candidates. A cut requiring the lifetime to be greater than zero was applied previously during the preselection. This is a lower cut and is varied from greater than zero to greater than 10. No improvement in $S/\sqrt{S+B}$ is seen when applying a tighter cut.

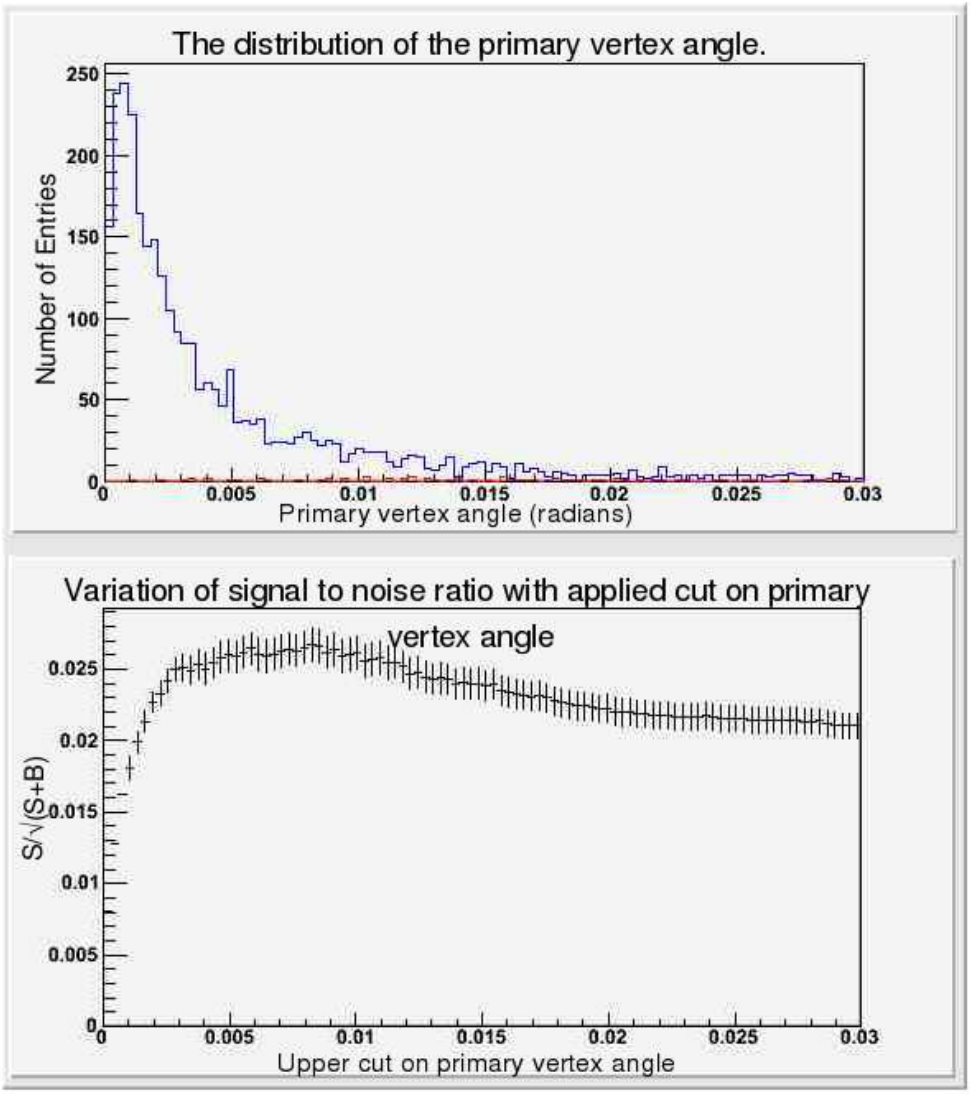

Figure 4.18: The variation of $S/\sqrt{S+B}$ with an upper cut on the primary vertex angle of the B_s^oy candidates. The blue line indicates signal data, while the red line indicates $b\bar{b}-$ inclusive events. The bottom section shows the variation of the signal to background ratio with the upper cut.

Fig. 4.18 shows the variation of the signal to noise ratio with an applied cut on the primary vertex angle of the B_s^o candidates. The primary vertex angle is the angle between the direction of flight of the B_s^o and its momentum vector. A cut requiring this angle to be less than 0.03 mrad was applied previously during the preselection. This is an upper cut and is varied from less than 0.03 mrad to less than 0 mrad. Little improvement in $S/\sqrt{S+B}$ is seen.

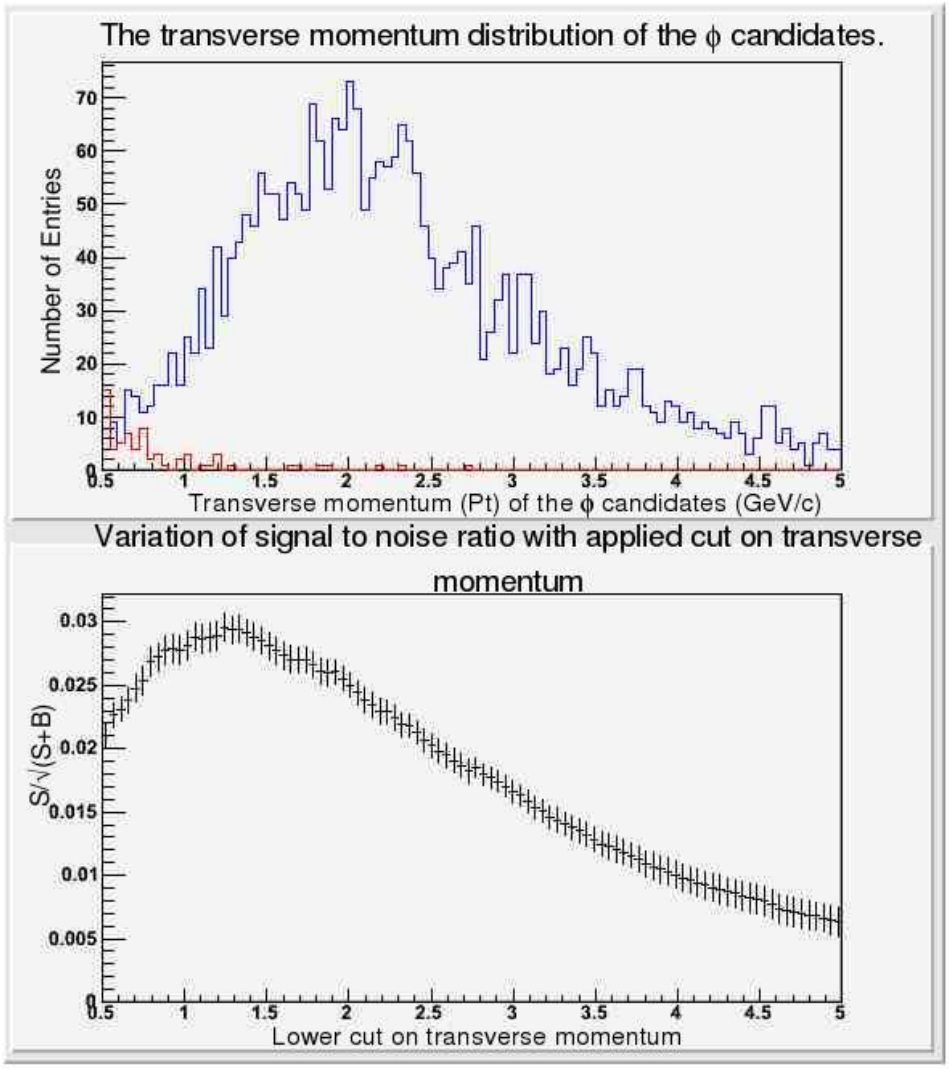

Figure 4.19: The variation of $S/\sqrt{S+B}$ with a lower cut on the transverse momentum of the ϕ candidates. The blue line indicates signal data, while the red line indicates $b\bar{b}-$ inclusive events. Only the lowest transverse momentum ϕ is shown from each pair. The bottom section shows the variation of the signal to background ratio with the lower cut.

Fig. 4.19 shows the variation of the signal to noise ratio with an applied cut on the transverse momentum (Pt) of the ϕ candidates. A cut requiring the Pt to be greater than 0.5 was applied during the preselection. It can be seen that it is possible to increase $S/\sqrt{S+B}$ further by applying a tighter transverse momentum cut.

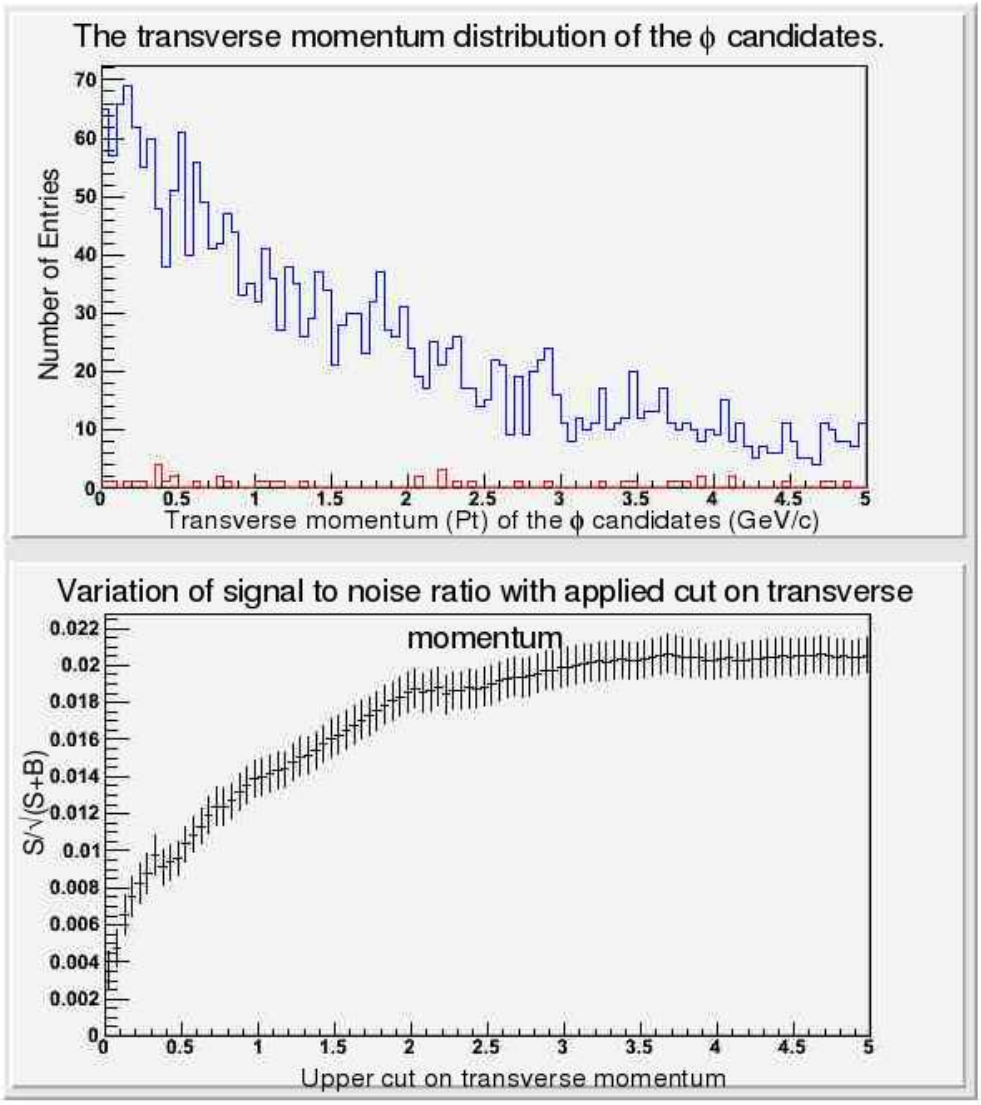

Figure 4.20: The variation of $S/\sqrt{S+B}$ with an upper cut on the χ^2 of the ϕ candidates. Only the highest χ^2 ϕ is shown from each pair. The blue line indicates signal data, while the red line indicates $b\overline{b}-$ inclusive events. The bottom section shows the variation of the signal to background ratio with the upper cut.

Fig. 4.20 shows the variation of the signal to noise ratio with an applied cut on the χ^2 of the ϕ candidates. This is an upper cut and is varied from χ^2 less than zero to χ^2 less than 5. Little improvement in $S/\sqrt{S+B}$ is seen.

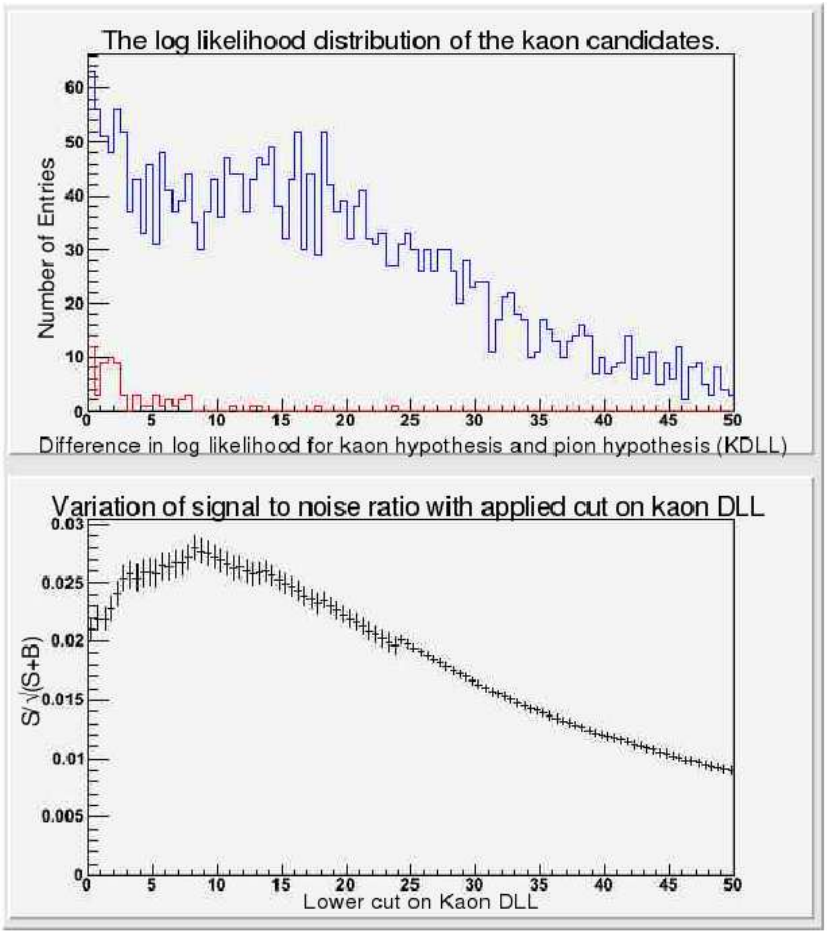

Figure 4.21: The variation of $S/\sqrt{S+B}$ with a lower cut on the difference in log likelihood (DLL) of the kaon candidates. Only the kaon with the lowest DLL is shown from each decay. The blue line indicates signal data, while the red line indicates $b\overline{b}-$ inclusive events. The bottom section shows the variation of the signal to background ratio with the lower cut.

Fig. 4.21 shows the variation of the signal to noise ratio with an applied cut on the difference in log likelihood (DLL) of the Kaon candidates. This is an lower cut and is varied from greater than zero to greater than 50. It can be seen that $S/\sqrt{S+B}$ can be improved with a tightening of this cut.

Based on Figs. 4.15-4.21 the cuts on the majority of observables do not require further optimisation. The gain in $S/\sqrt{S+B}$ is not significant in most cases, and tightening cuts further would result in the loss of MC-true signal events. The exceptions to this are the ϕ Pt and the Kaon DLL which show a clear improvement in $S/\sqrt{S+B}$ with variation in the applied cut. Cuts on these observables can be optimised further and this is discussed in the next section.

4.5.1 Optimisation of cut values

Based on the signal to background distributions shown above, two observables were chosen to optimise further. These were the transverse momentum of the ϕ candidates and the difference in log-likelihood of the kaon candidates. These two observables were optimised at the same time in a two-dimensional plot. This was done in order to maximise the number of MC-true signal events which pass the applied cuts. The mass windows and time normalisations were applied as before. The variation of $S/\sqrt{(S+B)}$ can be seen in

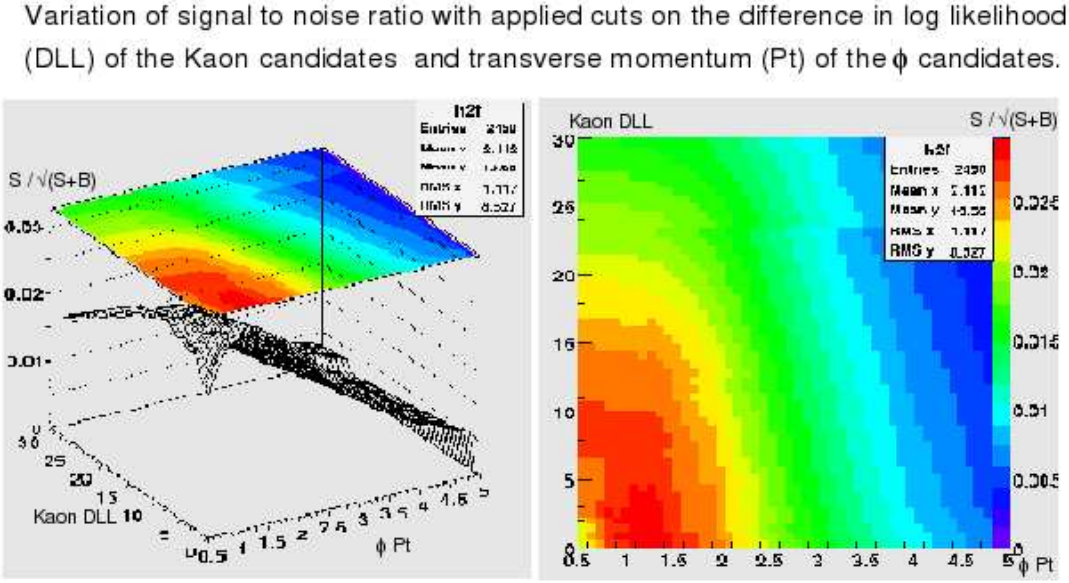

Figure 4.22: The variation of $S/\sqrt{(S+B)}$ with applied cuts on the Kaon DLL and ϕ Pt. The left hand plot shows the variation of $S/\sqrt{(S+B)}$ on the vertical axis. The cut on the Kaon DLL on the horizontal axis on the left, and the applied cut on the ϕ Pt on the horizontal axis on the right. The value of $S/\sqrt{(S+B)}$ is shown as a colour scale superimposed on the top of the left-hand plot and again on the plot on the right hand side.

Fig. 4.22. Based on this, a lower cut of 1.4 GeV/c on the transverse momentum of the ϕ candidates was applied. No further gain is made by increasing the cuts on the Kaon DLL. After this cut was applied, there remained:

- 2492 MC-true signal events
- 8 background events

from the original data. A significant reduction in background has been achieved.

4.6 Application of the Level 0, Level 1 and High Level Triggers

After the cut on ϕ transverse momentum, the Level 0, Level 1 and High Level triggers were applied to the signal data.

The first level trigger (Level 0) uses cuts on the transverse momentum of particles to select particles originating from a B_s^o decay. As B_s^o mesons are relatively heavy they are expected to decay into daughter particles with high Pt. The Level 1 trigger uses an algorithm to reconstruct tracks. Those tracks with a large Pt and large impact parameter to the primary vertex are selected. The High Level trigger considers the Level 1 decision again with better resolution. Cuts are applied selecting specific final states. The cuts applied for the $B_s^o \to \phi\phi$ decay are summarised in Ref. [87]. As discussed in Chapter 2 the Level 1 and High Level Trigger (HLT) have been combined since the original design of the LHCb experiment. However, the data analysis for DC04 data still treats them separately.

The Level 0 trigger left 880 MC-true signal events. After this the Level 1 trigger was applied, which reduced the signal by 266 leaving 614 entries. Finally the High Level Trigger removed a further 173 signal events. After all triggers were applied, 441 signal events remained out of the 2492 previously. The results are summarised in Table 4.1 below.

Trigger	Number of Events Remaining
Selection	2492
Level 0	880
Level 1	614
HLT	441

Table 4.1: The number of MC-true signal events remaining after the selection cuts and after each stage of the trigger has been applied.

After all cuts and triggers have been applied a total of 441 MC-true signal events re-

mained. The distribution of the observables does not differ significantly from the initial distributions, and that the cuts applied did not bias the sample. The number of background events which would pass the trigger was estimated by multiplying the 8 remaining background events by the ratio by which the signal events were reduced (i.e. 441/2492 $\sim$ 1.4). This avoids re-applying the mass window in the High Level Trigger. The fitted B_s^o mass distribution of these 441 events is shown in Fig. 4.23 below.

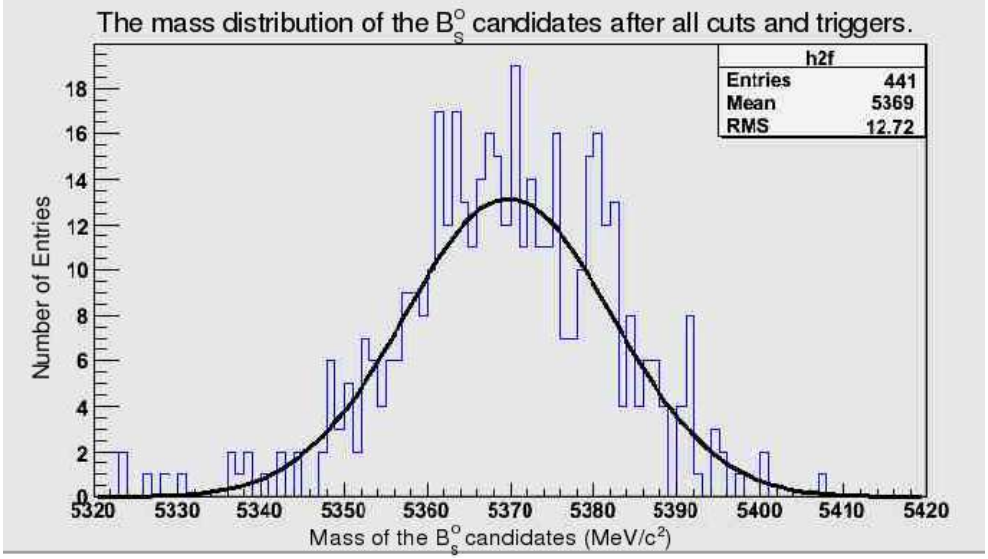

Figure 4.23: The fitted mass of the B_s^o candidates remaining after all cuts and triggers have been applied. The fit has a mean of 5369.75 $\pm$ 0.70 MeV/c^2 and a σ of 12.50 $\pm$ 0.72 MeV/c^2.

From this plot it can be seen that the resolution mass resolution of the B_s^o candidates is $\pm$12.50 MeV/c^2.

4.7 Event Yield

The expected number of signal and background events with one year of data was calculated. A nominal LHCb year is taken to be 10^7 seconds. Once normal running conditions have been reached the LHCb experiment will run at a luminosity (L) of $2{\times}10^{32}$ cm^{-2}s^{-1}. At this luminosity the $b\overline{b}$ production cross section ($\sigma_{b\overline{b}}$) at 14 TeV is 500 μbarn [40]. This corresponds to an integrated luminosity (L_{Int}) of $2{\times}10^{39}$ cm^{-2}, i.e. 2fb^{-1}. The expected signal yield in a nominal year (10^7 s) is given by:

$$N_{Sig} = L_{Int} \times \sigma_{b\overline{b}} \times 2 \times f_s \times BR^{Vis}(B_s^o \to \phi(K^+K^-)\phi(K^+K^-)) \times \epsilon_{Sig}^{Tot} \tag{4.12}$$

Here, f_s is the fraction of b-quarks expected to hadronize to form a B-meson, and is equal to 0.104 [87]. The factor of 2 takes into account the fact that both b and $\overline{b}$ mesons are produced in each event. The visible branching ratio for this channel, BR^{Vis}, is $(3.4 \pm 2.1) \times\ 10^{-6}$. The total signal efficiency, ϵ_{Sig}^{Tot} is given by:

$$\epsilon_{Sig}^{Tot} = \epsilon_{\theta}^{S} \times \epsilon_{Sig}^{Sel} \tag{4.13}$$

The quantity ϵ_{θ}^{S} takes into account the geometrical acceptance for the signal and is equal to 0.347 [87]. A total of 59,000 signal events were processed, and from the reconstructed events 441 passed all cuts and triggers, giving a selection efficiency of:

$$\epsilon_{Sig}^{Sel} = \frac{441}{59000} \sim (7.47 \pm 0.36) \times 10^{-3} \tag{4.14}$$

This gives an expected signal yield of:

$$N_{Sig} = 1,834 \pm 1,136 \text{ events per year} \tag{4.15}$$

where the error includes the error on the visible branching ratio and the Poissonian error on the number of MC-true events passing all cuts, combined in quadrature. Similarly, the number of $b\overline{b}-$inclusive background estimated to pass all cuts and triggers is equivalent to ~ 1.42 events. This is from a total of 32,402240 $b\overline{b}-$inclusive events which have been processed. The number of background events expected in a year is given by:

$$N_{b\overline{b}} = L_{Int} \times \sigma_{b\overline{b}} \times \epsilon_{b\overline{b}}^{Tot} \tag{4.16}$$

where L_{Int} and $\sigma_{b\overline{b}}$ are as before and the background efficiency $\epsilon_{b\overline{b}}^{Tot}$ is given by:

$$\epsilon_{b\overline{b}}^{Tot} = \epsilon_{\theta}^{b\overline{b}} \times \epsilon_{b\overline{b}}^{Mass} \times \epsilon_{b\overline{b}}^{Sel} \tag{4.17}$$

The geometrical acceptance for $b\overline{b}-$inclusive events, $\epsilon_{\theta}^{b\overline{b}}$ is equal to 0.434 [87]. In order to provide suitable statistics different B_S^0 mass windows were chosen for the background and signal data. The mass factor $\epsilon_{b\overline{b}}^{Mass}$ takes this into account. Rather than a simple ratio of mass windows, this was estimated by fitting the distribution of the background events to determine the relative numbers in the large and small mass windows. It was found that:

$$\epsilon_{b\overline{b}}^{Mass} = \frac{195.3}{8111.1} \sim 0.0241 \pm 0.0038 \tag{4.18}$$

where the error is dominated by the error of the fit to the background distribution.

$$\epsilon_{b\overline{b}}^{Sel} = \frac{1.42}{32,402,240} = (2.41 \pm 0.85) \times 10^{-8} \tag{4.19}$$

where errors are Poissonian. Evaluating $\epsilon_{b\overline{b}}^{Tot}$ and combining errors in quadrature gives:

$$\epsilon_{b\overline{b}}^{Tot} = (4.6 \pm 1.7) \times 10^{-10} \tag{4.20}$$

The expected number of $b\overline{b}-$inclusive events in one year was found to be:

$$N_{b\overline{b}} = 457 \pm 169 \text{ events per year} \tag{4.21}$$

(where the fractional error is equal to that of $\epsilon_{b\overline{b}}^{Tot}$). This gave a background to signal ratio of:

$$\frac{B}{S} = \frac{457}{1834} = 0.25 \pm 0.18 \tag{4.22}$$

The expected sensitivity to ϕ_s was simulated using this background to signal ratio. A full description of this simulation is available in Ref. [87]. A fast Monte Carlo simulation was carried out using 1834 signal events and 457 background events. A value of ϕ_s=0.2 was chosen. 500 toy experiments were carried out with an integrated luminosity of 2fb^{-1}, and the resulting fitted distribution for ϕ_s (ϕ_s^{fit}) is shown in Fig. 4.24 [94]. It can be seen that the mean is around at 0.2, as expected, with a sensitivity of σ= 0.14. The sensitivity to ϕ_s will also be dependent on the branching ratio but this dependence is expected to be weak. A significant deviation from $\phi_s = 0$ would imply New Physics effects, and this should be clearly distinguishable from the null hypothesis of $\phi_s = 0$.

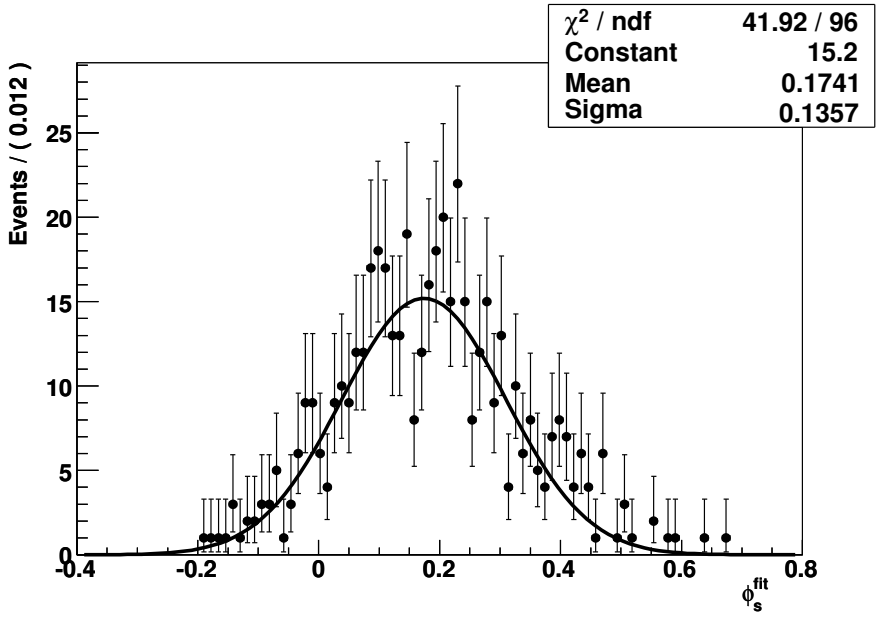

Figure 4.24: The sensitivity of the LHCb experiment to the weak mixing angle ϕ_s. A value of ϕ_s=0.2 was simulated [94].

4.8 Summary

The $B_s^o \to \phi\phi$ decay is an excellent probe for New Physics, and can be reconstructed at LHCb with good efficiency. After optimisation of applied cuts and application of the trigger it is expected that 1834±1136 signal and 457±169 background events will be produced in a nominal LHCb year. This gives a background to signal ratio of 0.25±0.18, allowing a sensitivity to the weak mixing phase ϕ_s of $\sigma(\phi_s)$= 0.14. The upper limit at 95% confidence is 0.23. It is estimated that around $10fb^{-1}$ of data will increase this precision to around $\sigma(\phi_s)$= 0.06. This is precise enough to make measurements of ϕ_s and hence of CP violation.

Chapter 5

Summary and Conclusions

The LHC at CERN is expected to turn on in 2008, and will be the world's highest energy particle accelerator. Four large experiments situated on the ring are currently under commission. One of these is the LHCb experiment which will study the decays of B-mesons. This will usher in an exciting new era of B-physics. In particular, the LHCb experiment aims to study rare decays and to shed new light on the phenomenon of CP-violation and help explain the excess of matter to antimatter in the observed universe.

The LHCb detector relies on two RICH counters to suppress charged particle backgrounds in many decay channels. The RICH counters use arrays of HPDs to image Cherenkov light and allow charged particle identification. Before producing the 550 HPDs needed for the detector, six pre-production HPDs were tested in a pion beam at CERN. These were found to work as expected and integration with the prototype electronics was achieved. Full production began in autumn 2005 and since then a total of 557 HPDs have been shipped to the Universities of Edinburgh and Glasgow for characterisation. It was found that over 97% of these were fully working, and that many exceeded the design specifications.

The RICH detector will play a vital role at the LHCb experiment. The excellent kaon-pion separation it provides will allow rare decays such as the $B_s^o \to \phi\phi$ to be studied. This involves a $b \to s$ Flavour-Changing Neutral Current (FCNC) transition which is forbidden at tree level in the Standard Model. FCNC decays provide an excellent probe for New Physics beyond the Standard Model. An analysis of the $B_s^o \to \phi\phi$ decay was performed on simulated data. A total of 59,000 signal events and $\sim$32.4M $b\overline{b}-$inclusive events were

analysed. A series of loose cuts were defined which reduced the number of background events and observables were chosen for further optimisation. It was found that applying a cut which required the transverse momentum of the ϕ candidates to be less than 1.4 reduced the ratio of $S/\sqrt{(S+B)}$ significantly. After all cuts and triggers were applied a background to signal ratio of 0.25±0.18 was obtained. This will allow the weak mixing angle ϕ_s to be measured with a precision σ of 0.14. It is estimated that around $10fb^{-1}$ of data will increase this precision to around $\sigma(\phi_s)$= 0.06.

Bibliography

[1] "Leptons","Bosons", W.M.Yao et al. (Particle Data Group), J.Phys.G **33**, 1 (2006)

[2] "Measurement of the Rate of $\nu_e + d \rightarrow p + pe^-$ Interactions Produced by 8B Solar Neutrinos at the Sudbury Neutrino Observatory", SNO collaboration, Phys.Rev.Lett. **87**(7) (2001)

[3] "Quarks and Leptons", F.Halzen and A.D.Martin, J.Wiley Sons (1984)

[4] "Quarks", S. Eidelman et al.(Particle Data Group), Phys. Lett. B **592**, 1 (2004 and 2005, partial update for 2006)

[5] "CP violation and the CKM matrix", A. Hocker and Z. Ligeti, hep−ph/0605217 (2006)

[6] "Studies of gluon confinement: How the gluon propagates", N. Brown and M.R. Pennington, Phys. Rev. D, **39**(9) (1989)

[7] "What do we know (and how) about the CKM Matrix", Y.Nir, SLAC−PUB−4987, http://www.slac.stanford.edu/cgi−wrap/getdoc/slac−pub−4987.pdf (1989)

[8] "Evidence for Oscillation of Atmospheric Neutrinos", Y. Fukuda et al, Phys. Rev. Lett. **81** pp.1562−1567 (1998).

[9] "Unitary Symmetry and Leptonic Decays", N.Cabibbo, Phys. Rev. Lett. **10** 531 (1963)

[10] "Quark mixing and CP Violation", A.Ali and B.Kayser, arXiv:hep−ph/9806230v1 (1998)

[11] "Weak Interactions with Lepton−Hadron Symmetry", S.L.Glashow, J.Iliopoulos and L.Maiani Phys. Rev. D**2** 1285 (1970)

[12] "Experimental Observation of a Heavy Particle J", J.J Aubert et al., Phys. Rev. Lett. **33**(1974) 1404

[13] "Discovery of a Narrow Resonance in e^+e^- Annihilation", J.E.Augustin et al., Phys. Rev. Lett. **33**(1974) 1406

[14] "Quark Mixing and CP Violation: The CKM Matrix", U.Nierste, Int. Journal of Modern Physics A, **21** 1724−1737 (2006)

[15] "Observation of a Dimuon Resonance at 9.5 GeV in 400−GeV Proton−Nucleus Collisions", W. Herb, et al., Phys. Rev. Lett. **39** 252 (1983)

[16] "Observation of Top Quark Production in $\overline{p}$−p Collisions with the Collider Detector at Fermilab" , F.Abe et al, Phys. Rev. Lett. **74** , 2626−2631 (1995)

[17] "Observation of the Top Quark", S.Abachi et al., Phys. Rev. Lett. **74** , 2632−2637 (1995)

[18] "CP−Violation in the Renormalizable Theory of Weak Interaction", M.Kobayashi and C.Maskawa, Prog.Theor.Phys. **49**(652) (1973)

[19] "Parametrization of the Kobayashi−Maskawa Matrix ", L.Wolfenstein, Phys. Rev. Lett. **21**(1945-1947) (1983)

[20] "The CKM Matrix and the Unitarity Triangle", M.Battaglia et al., arXiv:hep−ph/0304132v1 (2003)

[21] "Overview: Sides of the Unitarity Triangle", B. Grinstein, arXiv:0706.4179v1 (2007)

[22] http: //www.slac.stanford.edu/xorg/ckmfitter/ckm_results_summerEPS2005.htm

[23] "Behaviour of Neutral Particles Under Charge Conjugation", M.Gell−Mann and A.Pais, Phys. Rev. **97** 1387 (1955)

[24] "Decay of τ mesons of known charge", R.H. Dalitz, Phys. Rev. **94**, 1046−1051 (1954)

[25] "Question of Parity Conservation in Weak Interactions", T.D. Lee and C.N. Yang, Phys. Rev. **104**, 254−258 (1956)

[26] "Evidence for the 2π decay of the K_2^0 meson", J.H. Cristenson et al., Phys.Rev.Lett., **13**(138) (1964)

[27] "CP Violation in B meson decays", A.B. Carter and A.I. Sanda, Phys. Rev. D **23**(7) (1981)

[28] "Time Dependent CP−violation effects in $B^o\overline{B^o}$ systems", I. Dunietz and J.L. Rosner, Phys.Rev.D, **34**(5) (1986)

[29] "Observation of CP violation in the B^o meson system", The BaBar Collaboration Phys. Rev. Lett., **87**(9) (2001)

[30] "Observation of large CP violation in the neutral B−meson system", The Belle Collaboration, Phys. Rev. Lett., **87**(9) (2001)

[31] "CPT violation and the Standard Model", D. Colladay and V.A. Kostelecky, Phys. Rev. D **55**(11) (1997)

[32] ALEPH, DELPHI, L3 and OPAL Collaborations, Phys. Lett. B **565**(61) (2003)

[33] "Collider signatures of new large space dimensions", E.A. Mirabelli et al., Phys. Rev. Lett., **82**(11) (1999)

[34] "CP violation in Meson Decays", S. Eidelman et al., Phys. Lett. B 592, 1 (2004) (updated 2005)

[35] "Models for Geometric CP violation with extra dimensions", D.Chang et al., Phys. Lett. B, **515**(434-441) (2001)

[36] "Approximate CP in supersymmetric models", G.Eyal and Y.Nir, Nuclear Phys. B **528**(21-34) (1998)

[37] "Magnitude of the cosmological baryon asymmetry", S.Barr and H.A.Weldon, Phys. Rev. D **20**, 2494−2498 (1979)

[38] "A supersymmetric primer (version 4)", S.P. Martin hep−ph/9709356 (2006)

[39] "Supersymmetry", P. Fayet and S. Ferrara, Physics Reports **32**(249-334) (1977)

[40] "LHCb collaboration: Reoptimized Detector Design and Performance", CERN LHCC 2000-037 (2000)

[41] "The LCHb detector and triggers", F.C.D. Metlica et al., Nuclear Physics B **167**($pp173-176$) (2007)

[42] "The LHCb experiment", V. Gibson, LHCb-2007-100 (2007)

[43] "Developing Radiation Hard silicon for the LHCB Vertex Locator", C. Parkes et. al, Nuclear Inst.& Methods A, **552** pp.216-218 (2005)

[44] "Semiconductor Detectors" R.K. Bock, http: //rkb.home.cern.ch/rkb/PH14pp/node167.html (1998)

[45] "LHCb VELO Technical Design Report", The LHCb collaboration, CERN/LHCC 2001-0011 (2001)

[46] "LHCb Magnet Technical Design Report" The LHCb collaboration, CERN/LHCC 2001-010 (2001)

[47] 'LHCb Inner Tracker Technical Design Report", The LHCb collaboration, CERN/LHCC 2002-029 (2002)

[48] "LHCb tracking system and it's performance", J. Nardulli.
http: //lhcb−doc.web.cern.ch/lhcb−doc/presentations/conferencetalks/postscript/2006presentations/−LakeLouise2006Nardulli.pdf (2006)

[49] "The LHCb Outer Detector Design and Production", L.B.A. Hommels et al., Nuclear Science Symposium Conference Record 2004 (IEEE 1) **1** pp.672-676 (2004)

[50] "LHCb collaboration: LHCb Outer Tracker Technical Design Report",
The LHCb collaboration, CERN LHCC 2001-024 (2001)

[51] "Mass and Width Measurements of Sigma-c Baryons.",
Eric Vaandering, PhD Thesis, University of Colorado,
http: //www−e831afs.fnal.gov/people/ewv/thesis/html/node1.html (2000)

[52] "The straw tube technology for the LHCb outer tracking system", S. Bachmann et al., Nuclear Inst.& Methods A, **535**$(1-2)$ pp.171-174 (2004)

[53] "LHCb trigger system", F. Teuberta et al., Nuclear Physics B **156** pp.135-136 (2006)

[54] "Cherenkov Radiation and its applications", J.V. Jelley, Pergamon Press (1958)

[55] "RICH Technical Design Report", The LHCb collaboration, CERN LHCC 2003−030

[56] "The RICHes of LHCb",
C. D'Abmbrosio, http: //www.gsi.de/documents/DOC-2006-Mar-61-1.pdf (2006)

[57] "Multianode Photomultiplier Tubes for the LHCb RICH photodetectors", R.J.U. Chamonal,
PhD Thesis, University of Edinburgh (2005)

[58] "Carbon Fibre Spherical Mirrors for the LHCb RICH1 Detector", K. Lessnoff,
http: //lhcb−doc.web.cern.ch/lhcb-doc/presentations/ConferencePosters/Postcript/2007/MirrorsPoster.ppt (2007)

[59] "LHCb RICH1 Engineering Design Review Report" The LHCb RICH group,
http: //lhcb-rich.web.cern.ch/lhcb-rich/rich1edr/rich1edr.pdf (2004)

[60] "Status and prospects of the LHCb experiment" N.Harnew, Nuclear Physics B **120** pp.305-310 (2003)

[61] "LHCb Calorimeter from Trigger to Physics", O. Deschames et al,
http: //lhcb-doc.web.cern.ch/lhcb-doc/presentations/conferencetalks/postscript/2004presentations/-

LHCB_Calor04_Deschamps.ps (2004)

[62] "Design and Construction of the LHCb Scintillator Pad/Preshower Detector",
S.Fillipov et al., LHCb note LHCb 200−42 (2000)

[63] "SPD very front end electronics" S. Luengoa et al., Nuclear Inst.& Methods A, **567**(1) (2006)

[64] "The Shaslik Electromagnetic Calorimeter for the LHCb experiment" S. Barsuk, on behalf of the LHCb Calorimeter group,
http: //lhcb-doc.web.cern.ch/lhcb-doc/presentations/conferencetalks/postscript/2004presentations/-Barsuk_Callor04_proc.pdf (2004)

[65] "LHCb Calorimeters Technical Design Report", The LHCb collaboration, CERN/LHCC 2000-036 (2000)

[66] "LHCb Muon System Technical Design Report", The LHCb collaboration, CERN LHCC 2001-010 (2001)

[67] "The LHCb Trigger", A. Hernando, Acta Physica Polonica B **38**(3) (2007)

[68] "Trigger System Design Report", The LHCb collaboration, CERN LHCC 2003-031

[69] "LHCBPIX1 (Pixel Chip Manual)", kwyllie.home.cern.ch/kwyllie/LHCBPIX1.htm K. Wyllie

[70] Photonis (formerly Delflt Electronics Products) http: //www.photonis.com/

[71] "Production of 500 Pixel Hybrid Photon Detectors for the RICH counters of LHCb", T. Gys, http: //lhcb-doc.web.cern.ch/lhcb-doc/presentations/conferencetalks/postscript/2005presentations/-presentation_Gys.pdf (2005)

[72] "Production of 500 Pixel Hybrid Photon Detectors for the RICH counters of LHCb (Conference Talk)", T. Gys, Nuclear Inst. Meth. A **567** 176-179 (2006)

[73] "Pixel HPD Test System Hardware Description",
K. Wyllie, kwyllie.home.cern.ch/kwyllie/LHCBPIX1doc/Test_hardware_doc_1.0.pdf

[74] "A Brief Introduction to the JTAG Boundary Scan Interface",
N. Patavalis, http: //www.inaccessnetworks.com/projects/ianjtag/jtag-intro/jtag-intro.html (2001)

[75] CERN S-link homepage,
E. van der Bij, S. Haas, http: //hsi.web.cern.ch/HSI/s-link/

[76] "Readout of high speed S-Link data via a buffered PCI card", A.Guirao et al.,
http: //lhcb-doc.web.cern.ch/lhcb-doc/presentations/conferencetalks/postscript/2002presentations/WE-08_pcapac2002_paper.pdf

[77] "Photodetector Test Facilities Production Readiness Report", R.Chamonal et al.
http: //www.ph.ed.ac.uk/particle/Exp/PDTF/prr/pdtf-prr.pdf (2005)

[78] "PDTF Status and Status of Backpulse Measurements",
L. Carson, RICH meeting presentation,
http: //indico.cern.ch/getFile.py/access?contribId=4amp;resId=1amp;materialId=slidesamp;confId=10426
(2007)

[79] "Studies of MaPMTs with beetle-chip read-out", F.Muheim, Nuclear. Inst. Meth. A **553** 351-355 (2005)

[80] G.Aglieri Rinella, private communication (2006)

[81] "ROOT: An Object-Orientated Data Analysis Framework", http://root.cern.ch/

[82] "Performance of the LHCb RICH photodetectors in a charged particle beam", M. Adinolfi et al., Nuclear Inst.& Methods A, **574** pp. 39-49 (2007)

[83] "GEANT - Detector Description and Simulation Tool", http: //wwwasd.web.cern.ch/wwwasd/geant/

[84] J.Dickens, private communication (2005)

[85] "CP Violation in the B System: Status and Perspectives", R. Fleischer, hep−ph/0512271 (2005)

[86] "First evidence for $B_s\phi\phi$ and penguin B decays at CDF", M. Rescigno (for the CDF collaboration), arXiv:hep−ex/0410063v2 (2004)

[87] "LHCb's sensitivity to new CP-violating phases in the decay $B_s^0 \to \phi\phi$", S.Amato et al., LHCb 2007-047 (2007)

[88] "The BaBar Physics Book: Physics at an asymmetric B factory", The BaBar Collaboration, SLAC−R−0504 (1999)

[89] "$\phi\phi$ decay as a parity and signature test", T.L.Trueman, Phys. Rev. D, **18**(8) (1978)

[90] "Polarization in B Decays", W.−M. Yao et al. (Particle Data Group), J. Phys. G **33**(1) (2006) (URL: http: //pdg.lbl.gov)

[91] "Gauss:The LHCb simulation program: User's guide and Reference Manual",
http: //lhcb-comp.web.cern.ch/lhcb-comp/Simulation/Gauss.pdf

[92] "Boole:LHCb digitization program: User's guide and Reference Manual",
http: //lhcb−release−area.web.cern.ch/LHCb-release-area/BOOLE/BOOLE_v6r5/doc/Boole.pdf

[93] "Brunel: LHCb reconstruction program: User's Guide",
http: //lhcb-comp.web.cern.ch/lhcb−comp/Reconstruction/BUG.pdf

[94] Y.Xie, private commumication (2007)

[95] "The Heavy Flavour Averaging Group" http: //www.slac.stanford.edu/xorg/hfag/ (2007)